論文 / 著書情報
Article / Book Information

題目(和文)	直接数値計算による乱流予混合燃焼の大域及び局所火炎構造に関する研究
Title(English)	Investigation on global and local flame structures of turbulent premixed combustion by direct numerical simulation
著者(和文)	BASMILYENERDAG
Author(English)	Basmil Yenerdag
出典(和文)	学位:博士（工学）, 学位授与機関:東京工業大学, 報告番号:甲第9774号, 授与年月日:2015年3月26日, 学位の種別:課程博士, 審査員:店橋　護,花村　克悟,小酒　英範,齊藤　卓志,志村　祐康
Citation(English)	Degree:, Conferring organization: Tokyo Institute of Technology, Report number:甲第9774号, Conferred date:2015/3/26, Degree Type:Course doctor, Examiner:,,,,
学位種別(和文)	博士論文
Type(English)	Doctoral Thesis

Doctoral Dissertation

Investigation on Global and Local Flame Structures of Turbulent Premixed Combustion by Direct Numerical Simulation

Supervisor

Professor : Mamoru Tanahashi

Department of Mechanical and Aerospace Engineering
Graduate School of Science and Engineering
Tokyo Institute of Technology

Basmil Yenerdag

Contents

1 Introduction **1**

1.1 Combustion technology 1

1.2 Background 5

1.3 Simulation techniques 6

1.3.1 Reynolds averaged Navier–Stokes simulation 6

1.3.2 Large eddy simulation 6

1.3.3 Direct numerical simulation 7

1.4 Review of previous studies 7

1.5 Objectives of this study 9

1.6 Outline of this thesis 10

2 Direct numerical simulation of hydrogen–air premixed flames in a constant volume vessel **12**

2.1 Preface 12

2.2 Direct numerical simulation 13

2.2.1 Governing equations 13

2.2.2 Chemical reaction 16

2.2.3 Thermodynamic properties 19

2.2.4 Transport coefficients 20

2.2.5 Numerical methods 21

2.3 Flame and flow behavior in a constant volume vessel 28

2.4 Heat flux and total heat loss in a constant volume vessel 40

2.4.1 Effects of pressure on wall heat flux 40
2.4.2 Total heat loss in a constant volume vessel 45
2.5 Statistical characteristics of local flame structure 49
2.6 Conclusions of this chapter 57

3 Direct numerical simulation of methane–air premixed flames in thin reaction zones 58
3.1 Preface 58
3.2 Direct numerical simulation 60
3.2.1 Numerical methods and initial conditions 60
3.3 Local flame structures 68
3.4 Statistical characteristics of local flame structures 93
3.4.1 Effects of turbulence on local flame thickness and local mean curvature 93
3.4.2 Effects of turbulence to the reaction and preheat zones . . 103
3.4.3 Correlations of heat release rate with flame curvature and tangential strain rate in methane–air premixed flames . . . 113
3.5 Conclusions of this chapter 117

4 Fractal characteristics of turbulent premixed flames 120
4.1 Preface 120
4.2 Fractal characteristics of hydrogen–air premixed flames in a constant volume vessel 121
4.3 Fractal characteristics of methane–air premixed flames in thin reaction zones 130
4.4 Conclusions of this chapter 136

5 Conclusions 137

A The detailed kinetic mechanism for hydrogen–air premixed flame 157

B The detailed kinetic mechanism for methane–air premixed flame 159

Acknowledgments **171**

The result of chapter 2 is partially published in the following journal and conference papers:

(1) Basmil Yenerdag, Naoya Fukushima, Masayasu Shimura, Mamoru Tanahashi, Toshio Miyauchi, Turbulence–flame interaction and fractal characteristics of H_2-air premixed flame under pressure rising condition, Proceedings of the Combustion Institute 35 (2) (2015) 1277-1285. doi:http://dx.doi.org/10.1016/j.proci.2014.05.153

(2) Basmil Yenerdag, Naoya Fukushima, Masayasu Shimura, Mamoru Tanahashi and Toshio Miyauchi, Dynamics of Turbulent Flame in a Constant Volume Vessel, 22nd International Symposium on Transport Phenomena, Delft, Netherlands, 8-11 November (2011)

The result of chapter 3 is partially submitted and will be published in the following conference paper:

(1) Basmil Yenerdag, Yoshitsugu Naka, Masayasu Shimura and Mamoru Tanahashi, 3D DNS of Methane-Air Turbulent Premixed Flame in Thin Reaction Zones with a Detailed Kinetic Mechanism, 9th International Symposium on Turbulence and Shear Flow Phenomena, Melbourne, Australia, 30 June-3 July, (2015) (Accepted)

The result of chapter 4 is partially published in the following journal paper:

(1) Basmil Yenerdag, Naoya Fukushima, Masayasu Shimura, Mamoru Tanahashi, Toshio Miyauchi, Turbulence–flame interaction and fractal characteristics of H_2-air premixed flame under pressure rising condition, Proceedings of the Combustion Institute 35 (2) (2015) 1277-1285. doi:http://dx.doi.org/10.1016/j.proci.2014.05.153

Chapter 1

Introduction

1.1 Combustion technology

Combustion of fossil fuels such as oil, natural gas and coal, is a main energy source and accounts for around 80% of world primary energy supply. As civilizations advance, dependency on fossil fuels to produce energy will increase. However, the negative effects of fossil fuels on environment is a major concern and the global warming issue is one of the top priorities of many governments' agendas. Our planet is warming because of the greenhouse effect which is a result of increasing greenhouse gases such as carbon dioxide in the atmosphere. A recent research shows that more than 85% of carbon dioxide emissions of human source is the result of combustion of fossil fuels [1]. Due to the increasing pollution, governments and non-governmental organizations started searching alternative energy resources. The alternative energy resources are mainly solar energy, wind energy, hydro energy, nuclear energy and bio-fuels. Although many advancement have been made, aforementioned alternative energy sources such as solar and wind energy are not able to provide even a fraction of energy as that of fossil fuels which are widely used by the majority of the population on earth for many purposes such as transportation, electricity production and so on. Nuclear energy is also a promising energy source, although its security and negative environment impact in the long run is still under serious debate, particularly after

the Chernobyl disaster in 1986 and a recent accident known as Fukushima Daiichi incident, which is the result of a huge tsunami, triggered by Tohoku earthquake on 11 March 2011. As a result of inconsistency in renewable energy and security issues in nuclear energy, demand for fossil fuels will continue to rise. By 2040, 78% of the total energy consumption will be supplied by fossil fuels [2]. A recent report by U.S. Energy Information Administration [3] shows that the total petroleum production in the world in 2011 is 75 millions barrels per day, and is projected to increase to 99.1 millions barrels per day by 2040. Figure 1.1 shows the electricity production in percentage by burning fossil fuels for G8 (The group of 8 leading advanced economies) countries [4]. As can be seen, most of the G8 countries except France and Canada produce the majority of their electricity from burning of fossil fuels. Due to the increasing demand of fossil fuels, prices are also expected to increase. U.S. Energy Information Administration reported the North Sea Brent crude oil prices in three different cases: The reference case, high oil price and low oil price cases (in 2012 dollars) as shown in Fig. 1.2 [3]. The increasing prices of fossil fuels is a huge burden to economy, especially for fossil fuel dependent countries such as Japan. After the nuclear accident in March 2011, Japan became the second largest net fossil fuel importer in the world [5], and estimated cost of import of fossil fuels reached 5.3% of her nominal GDP [6]. As fossil fuels usage continue to be dominant in the future, it is crucial to improve the efficiency of combustion systems to make energy more affordable and achieve a cleaner combustion.

Figure 1.1: Electricity production percentage by burning fossil fuels for G8 countries [4].

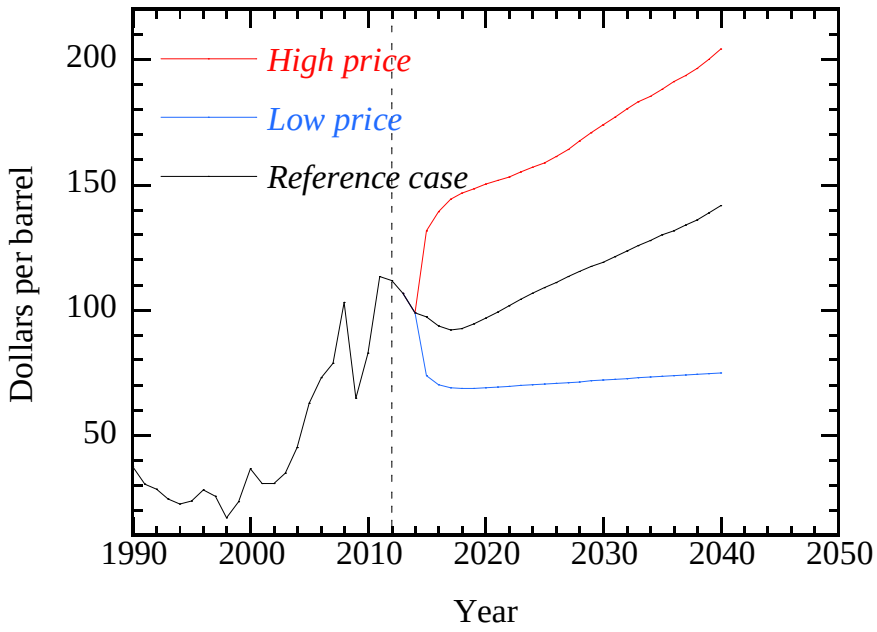

Figure 1.2: North Sea Brent crude oil prices in three different scenarios (in 2012 dollars) [3].

1.2 Background

Turbulent combustion can be classified as premixed and non-premixed combustion. In Diesel engines, gas turbines or industrial furnaces, combustion takes place under non-premixed condition. In this condition, local equilibrium chemistry assumption is used as chemical time scales are much smaller than the convective and diffusion time scales [7, 8]. In spark ignition (SI) engines, fuel and oxidizer is mixed before combustion is started by a spark, this phenomena is referred as premixed combustion. Modeling this type of combustion is more difficult than non-premixed flames, as premixed flames' location does not depend on the mixing field but on the flow field itself [7–9]. The length and the time scales of the flow therefore would have significant effects on the characteristics of the flame, such as flame displacement speed, flame thickness and chemical kinetics [7–9]. The relationship between the characteristics of premixed flame such as flame speed and flame thickness and length scale of flow field can be used to define different flame regimes of turbulent premixed combustion. These regimes are the wrinkled flamelets, the corrugated flamelets, the thin reaction zones and the broken reaction zones [10].

In practical applications, premixed combustion occurs in turbulent flow conditions. Understanding the turbulence–flame interaction of premixed flames is of great importance for designing low emission and high efficiency combustors. The conservation equations of mass, momentum, energy and chemical species mass concentrations can be used to describe the interactions of turbulence and flame. Analytical solutions of these nonlinear differential equations are almost impossible, consequently, investigation on characteristics of turbulent premixed flames had been conducted by experiments only before the introduction of high speed parallel computing. With the improvement in technology, measurements of flame front, flame speed, local flame thickness and time-resolved flow field can be done by laser based diagnostics [11–17]. Although these studies have provided insightful information on the premixed flames, flame characteristics have not been well

understood due to the difficulties in measurements of local flame structures.

As computational technology develops, numerical simulation has become a promising tool for investigations on turbulent combustion. In the next section, numerical simulation techniques for turbulent combustion will be discussed briefly as the present thesis utilizes numerical simulation for investigations on premixed combustion.

1.3 Simulation techniques

1.3.1 Reynolds averaged Navier–Stokes simulation

Reynolds averaged Navier–Stokes simulation (RANS) is a simulation technique that is widely used in practice. In this numerical approach, the Reynolds averaged or Favre averaged equations are obtained by decomposing the conservation equations into mean and fluctuating quantities. With this averaging operation, more unknowns will be obtained than the equations, therefore, additional models are needed to close the averaged equations. In computational fluids dynamics (CFD) applications, the $k - \epsilon$ model [18, 19] is used to close Reynolds stress by solving the turbulent kinetic energy k and the dissipation rate ϵ. In reacting flow, turbulent combustion model is also required for chemical reaction and several models have been proposed for RANS [7, 20, 21]. This numerical approach is widely used in industrial applications such as boilers, gas turbines and furnaces. Thanks to short computational time and low memory requirement in RANS, research and development cost have been reduced. However, the turbulence and its effects on flame elements are not solved explicitly, as the accuracy of this approach depends on the models.

1.3.2 Large eddy simulation

Large eddy simulation (LES) is a simulation technique that solves the large scale motion of turbulence explicitly, while a subgrid scale (SGS) model is employed

to deal with small scale of turbulence. With this operation, the computational resources can be reduced because LES does not solve the smallest scale of turbulence explicitly. This technique is considered to be more accurate than RANS. Since the small scales of turbulence have great impact on flame wrinkling and heat release, the accuracy of SGS models is very important to account the flame characteristics. LES is not used for practical purposes since it requires more computational resources compared to RANS. In the near future, with the improvement in computational technology, LES is considered to be an important simulation technique for industrial CFD [22].

1.3.3 Direct numerical simulation

Direct numerical simulation (DNS) solves the Navier–Stokes equations without using any model and DNS is considered to be the highest level of numerical simulation technique for turbulent and turbulent reacting flows. In DNS, all turbulence scales are solved explicitly, therefore the effects of the smallest scale of turbulence on the flame elements can be captured. To capture the chemical reactions correctly, about 10 grid points should be contained to resolve flame thickness, and temporal resolutions should be of the order of nanosecond. With DNS, detailed information on the characteristics of flame elements can be provided [23–26], and the results can be used to validate and develop turbulent combustion models for RANS and LES [27, 28]. To resolve all length and time scales in a flow field, huge computational resources are necessary, therefore, DNS is only limited to small domain sizes and simple flow and flame configurations.

1.4 Review of previous studies

DNS is a valuable tool for enhancing our understanding of fundamentals of turbulent premixed combustion. Due to the limited computational resources in the past, DNS of turbulent premixed flame was conducted only in one-dimensional configuration with a complex chemical mechanism [29]. With the developments in com-

putational technology, two-dimensional DNS of premixed flames with a simplified chemistry model [30] and a complex kinetics mechanism [31] were conducted. Although these studies provided valuable information on premixed flames such as flame–vortex interaction and flame characteristics over a range of equivalence ratios, the true nature of turbulence could not be captured in two-dimensional flow configuration. Three-dimensional DNS of turbulent premixed flame in isotropic turbulent flow was conducted with a single-step chemistry [32] to investigate the flame–flow coupling. Tanahashi et al. [23] conducted three-dimensional turbulent premixed planar flame with a detailed kinetic mechanism. It was shown that fine scale eddies in turbulence have a great contribution to flame wrinkling and increase in heat release rate. Nada et al. [33] investigated the effects of turbulence on the local flame structures of hydrogen–air premixed planar flames with three-dimensional DNS, they showed that three-dimensional local flame structures such as handgrip and spire structures are formed by the invasion of coherent fine scale eddies, which is a universal fine scale structures of turbulence [34–36]. Shim et al. [37] investigated local flame structures of high Reynold number flame by three-dimensional DNS, they showed that complicated structures such as multiply folded structures, flame peninsulas and multi-layer structures are formed due to strong turbulence of unburned gas. Shim et al. [37] and Chatakonda et al. [38] conducted three-dimensional DNS to investigate global flame structures of premixed flame such as flame wrinkling and inner cutoff. Clarifying these flame structures is crucial for determining turbulent burning speed, as increased wrinkled flame surface area accounts for most of the enhanced burning [39]. Recently, DNS in different flow configurations such as V-flames [40–42], swirl flames [43, 44] and jet flames [45–47] have become possible for investigations on turbulence–flame interactions.

These studies enabled researchers to have a better and deeper understanding on the local and global flame structures of premixed combustion. Clarifying these flame structures of turbulent premixed flame is essential for developments of turbulent combustion model for industrial applications.

1.5 Objectives of this study

To achieve cleaner and more affordable combustion, it is necessary to develop high accuracy of turbulent combustion models. As was discussed in the previous section, detailed investigations on the turbulence–flame interactions of hydrogen–air premixed flames with different flow configurations have been made by three-dimensional DNS [23, 39, 41, 46], promising results have been obtained for hydrogen premixed flames. Hydrogen is an important fuel which has unique characteristics and can be produced from fossil fuels such as coal and natural gas. Although there are some limitations on hydrogen technology in terms of production, transportation and storage, its faster burning rate, lower lean operational limit in SI engines compared to gasoline, and more importantly no carbon monoxide and carbon dioxide emissions show that hydrogen can play a prominent role in clean combustion technology [48]. Further understanding of the characteristics of hydrogen–air premixed flames in a SI engine condition, where temperature and pressure increase with flame propagation is required. Due to the requirement of enormous computational resources, three-dimensional DNS of premixed combustion was limited to atmospheric-constant pressure conditions. Because the spatial resolution should be about of the order of one tenth of laminar flame thickness to capture the chemical reactions correctly. If the pressure is doubled, the flame thickness will be reduced, therefore the spatial resolution should be at least of the order of one twentieth of laminar flame thickness, which leads to even higher computing time and memory. The first objective of this study is to investigate the local flame characteristics of turbulent hydrogen–air premixed flames under pressure rising conditions with detailed kinetic mechanism by employing DNS approach.

The computational cost of three-dimensional DNS of hydrocarbon flames is much higher compared to hydrogen flames. 12 chemical reactive species and 27 elementary reactions are sufficient to represent hydrogen–air premixed flames. On the other hand, in methane flames, at least 50 reactive species and more than

300 elementary reaction are required. Several three-dimensional DNS studies of methane–air premixed flames have been conducted with a kinetic mechanism including not more than 20 reactive species due to enormous computational cost [40, 47, 49–51]. However, to have a better understanding on the local flame structures such as local heat release rate, local flame thickness, flame front curvature and tangential strain rate, the detailed description of the kinetic mechanism is required. Therefore, three-dimensional DNS of methane–air premixed flame with at least 50 chemical species and 300 elementary reactions are necessary for detailed investigation on the local flame structures. To design high thermal efficiency and low emission combustors such as gas turbines, high inlet temperature and lean premixed combustion is of great interest. Turbulent premixed flames under such conditions are considered to be formed in the thin or broken reaction zones. However, due to difficulties in measurement of turbulent flames in experiments, flame structures even in the thin reaction zones have not been clarified yet. Therefore, the second objective of this study is to conduct three-dimensional DNS of turbulent premixed planar flames propagating in homogeneous isotropic turbulence with GRI-Mech 3.0 chemical mechanism [52] which includes 53 reactive species and 325 elementary reactions to investigate local flame characteristics of methane–air premixed flames classified into the thin reaction zones.

The third objective of this study is to clarify the effects of pressure increase on the global characteristics of flame structures of hydrogen–air premixed flame, and the global flame structures of methane–air premixed flames in the thin reaction zones.

1.6 Outline of this thesis

In chapter 2, three-dimensional DNS of hydrogen–air turbulent premixed flames at relatively high Reynolds number in a constant volume vessel configuration are conducted considering the detailed kinetic mechanism to investigate the turbulence–flame interaction under pressure rising conditions.

In chapter 3, three-dimensional DNS of methane–air turbulent premixed planar flames propagating in homogeneous isotropic turbulence are conducted using GRI-Mech 3.0 kinetic mechanism to investigate the local flame structures in the thin reaction zones regime.

In chapter 4, fractal characteristics of hydrogen–air premixed flames in a constant volume vessel and methane–air turbulent premixed planar flames in the thin reaction zones are investigated using the DNS database from chapter 2 and 3.

In chapter 5, the main conclusions from each chapter are summarized.

Chapter 2

Direct numerical simulation of hydrogen–air premixed flames in a constant volume vessel

2.1 Preface

To develop proper combustion models for engineering applications such as a combustion chamber where temperature and pressure increase with flame propagation, characteristics of turbulent premixed flame under pressure rising conditions need to be clarified. However, due to the difficulties in measurement of flame structure in experiments, flame characteristics have not been well understood yet. DNS is a technique that provides an access to the details of turbulent combustion thanks to impressive developments in computational technology in recent years. Owston et al. [53] have conducted one-dimensional DNS to investigate interactions of premixed hydrogen laminar flames with walls. They have measured heat flux at constant pressure condition and have shown that the maximum heat flux increases substantially when the pressure is doubled.

Three-dimensional DNSs have been conducted to investigate local flame characteristics in the thin reaction zones, the corrugated flamelets and the wrinkled flamelets for hydrogen–air premixed flames in our previous studies [23, 24, 33, 37, 54]. Shim et al. [54] have shown that fluctuations of the heat release rate at

the flame front in the thin reaction zones is relatively larger than that in the corrugated flamelets and the heat release rate of most of the flame elements are in the range of $0.9 - 1.1$ times that of the laminar flame, while those in the corrugated flamelets and the wrinkled flamelets [23, 24, 33] have a value around that of the corresponding laminar flame. It should be noted that these previous studies have been carried out under a constant pressure condition. In a combustion chamber, however, temperature and pressure increase. Such changes have a crucial impact on fluid dynamics and characteristics of flame elements due to changes in transport and thermo-chemical properties. Therefore, a deeper understanding of turbulence–flame interactions under pressure rising conditions is necessary.

In this chapter, three-dimensional DNS of hydrogen–air turbulent premixed flames at relatively high Reynolds number in a constant volume vessel configuration has been conducted considering the detailed kinetic mechanism to investigate the turbulence–flame interaction under pressure rising conditions.

2.2 Direct numerical simulation

2.2.1 Governing equations

The governing equations for fully-compressible reacting flows are the conservation equations of mass, momentum, energy and chemical species mass concentrations and can be written, respectively as

$$\frac{\partial \rho}{\partial t} + \nabla \cdot (\rho \boldsymbol{u}) = 0, \tag{2.1}$$

$$\rho \frac{\partial \boldsymbol{u}}{\partial t} + \rho \boldsymbol{u} \cdot (\nabla \boldsymbol{u}) = -\nabla \cdot \boldsymbol{P} + \rho \sum_{i=1}^{N} Y_i \boldsymbol{f}_i, \tag{2.2}$$

$$\rho \frac{\partial e_t}{\partial t} + \rho \boldsymbol{u} \cdot (\nabla e_t) = -\nabla \cdot \boldsymbol{q} - \boldsymbol{P} : (\nabla \boldsymbol{u}) + \rho \sum_{i=1}^{N} Y_i \boldsymbol{f}_i \cdot \boldsymbol{V}_i, \tag{2.3}$$

$$\frac{\partial Y_i}{\partial t} + \boldsymbol{u} \cdot \nabla Y_i = -\frac{1}{\rho} \nabla \cdot (\rho Y_i \boldsymbol{V}_i) + \frac{w_i}{\rho}, \tag{2.4}$$

where ρ, $\boldsymbol{u}$, e_t and N denote the density, the fluid velocity vector, the internal energy and the number of chemical species, respectively. Y_i, $\boldsymbol{f}_i$, $\boldsymbol{V}_i$ and w_i are mass fraction, external force, diffusion velocity and reaction rate of the ith species. The heat flux $\boldsymbol{q}$ can be written as follows:

$$\boldsymbol{q} = -\lambda \nabla T + \rho \sum_{i=1}^{N} h_i Y_i \boldsymbol{V}_i + R^0 T \sum_{i=1}^{N} \sum_{j=1}^{N} \left(\frac{X_j D_{T,i}}{W_i D_{ij}} \right) \left(\boldsymbol{V}_i - \boldsymbol{V}_j \right) + \boldsymbol{q}_R, \quad (2.5)$$

In the above equation λ, R^0, T denote the thermal conductivity, the universal gas constant and the temperature, respectively. $D_{T,i}$ is the thermal diffusion coefficient, D_{ij} is the binary diffusion coefficient. h_i, X_i and W_i denote the enthalpy, the mole fraction and the molecular weight of the ith species, respectively.

The mass diffusion velocity $\boldsymbol{V_i}$ of the chemical species i is defined in the following equation:

$$\begin{aligned} \nabla X_i &= \sum_{j=1}^{N} \left(\frac{X_i X_j}{D_{ij}} \right) \left(\boldsymbol{V}_j - \boldsymbol{V}_i \right) \\ &+ \left(Y_i - X_i \right) \frac{\nabla p}{p} + \frac{\rho}{p} \sum_{j=1}^{N} Y_i Y_j \left(\boldsymbol{f}_i - \boldsymbol{f}_j \right) \\ &+ \sum_{j=1}^{N} \left[\left(\frac{X_i X_j}{\rho D_{ij}} \right) \left(\frac{D_{T,j}}{Y_j} - \frac{D_{T,i}}{Y_i} \right) \right] \frac{\nabla T}{T}. \end{aligned} \quad (2.6)$$

In the present DNS, following assumptions are made:

No external forces

$$\boldsymbol{f}_i = 0, \quad (2.7)$$

Negligible Soret effect

$$\sum_{j=1}^{N} \left[\left(\frac{X_i X_j}{\rho D_{ij}} \right) \left(\frac{D_{T,j}}{Y_j} - \frac{D_{T,i}}{Y_i} \right) \right] \frac{\nabla T}{T} = 0, \quad (2.8)$$

Negligible Dufour effect

$$R^0 T \sum_{i=1}^{N} \sum_{j=1}^{N} \left(\frac{X_j D_{T,i}}{W_i D_{ij}} \right) \left(\boldsymbol{V}_i - \boldsymbol{V}_j \right) = 0, \quad (2.9)$$

Negligible pressure gradient diffusion

$$(Y_i - X_i)\frac{\nabla p}{p} = 0, \tag{2.10}$$

Negligible bulk viscosity

$$\kappa = 0, \tag{2.11}$$

Negligible radiative heat transfer

$$\boldsymbol{q}_R = 0, \tag{2.12}$$

With the above assumptions, the governing equations can be written as follows.

$$\frac{\partial \rho}{\partial t} + \nabla \cdot (\rho \boldsymbol{u}) = 0, \tag{2.13}$$

$$\frac{\partial \rho \boldsymbol{u}}{\partial t} + (\nabla \rho \boldsymbol{u}\boldsymbol{u}) = -\nabla \cdot \boldsymbol{P}, \tag{2.14}$$

$$\begin{aligned}\frac{\partial \rho T}{\partial t} + \nabla \cdot (\rho \boldsymbol{u} T) &= \frac{1}{\bar{c}_v}\nabla \cdot (\lambda \nabla T) - \frac{1}{\bar{c}_v}\sum_{i=1}^{N}\left(\rho Y_i \boldsymbol{V}_i c_{p,i} \nabla T\right) \\ &\quad -\frac{T}{\bar{c}_v}\sum_{i=1}^{N}\left[R_i \nabla \cdot (\rho Y_i \boldsymbol{V}_i)\right] - \frac{1}{\bar{c}_v}\boldsymbol{P} : (\nabla \boldsymbol{u}) \\ &\quad -\frac{1}{\bar{c}_v}\sum_{i=1}^{N}(h_i w_i) + \frac{T}{\bar{c}_v}\sum_{i=1}^{N}(R_i w_i),\end{aligned} \tag{2.15}$$

$$\frac{\partial Y_i}{\partial t} + \boldsymbol{u} \cdot \nabla Y_i = -\frac{1}{\rho}\nabla \cdot (\rho Y_i \boldsymbol{V}_i) + \frac{w_i}{\rho}. \tag{2.16}$$

R_i, $c_{v,i}$ and $c_{p,i}$ denote, respectively, characteristic gas constant, specific heat capacities at constant volume and pressure for chemical species i. The mixture averaged specific heat capacity at constant volume, $\bar{c_v}$, is given by

$$\bar{c_v} = \sum_{i=1}^{N} c_{v,i} Y_i \tag{2.17}$$

the stress tensor, $\boldsymbol{P}$ is given by

$$\boldsymbol{P} = \left[p + \frac{2}{3}\mu (\nabla \cdot \boldsymbol{u})\right]\boldsymbol{I} - \mu\left[(\nabla \boldsymbol{u}) + (\nabla \boldsymbol{u})^T\right], \tag{2.18}$$

where p, μ and $\boldsymbol{I}$ denote pressure, dynamic viscosity and the identity matrix, respectively. The pressure is obtained by the equation of state for ideal gas of multicomponent and can be written as

$$p = \rho R^0 T \sum_{i=1}^{N} \left(\frac{Y_i}{W_i} \right), \tag{2.19}$$

the diffusion velocity is given by

$$V_i = -\frac{1}{X_i} D_{im} \nabla X_i, \tag{2.20}$$

where D_{im} denote mixture diffusion coefficient for species i. The mixture diffusion coefficient is obtained by using binary diffusion coefficients, D_{ij}, as follows,

$$D_{im} = \frac{1 - Y_i}{\sum_{i \neq j}^{N} X_i / D_{ij}}. \tag{2.21}$$

2.2.2 Chemical reaction

The forward and backward reactions of a general k set of reactions can be written as follows:

$$\sum_{i=1}^{I} \nu'_{i,k} X_i \Longleftrightarrow \sum_{i=1}^{I} \nu''_{i,k} X_i \tag{2.22}$$

Here, $\nu'_{i,k}$ and $\nu''_{i,k}$ are the reactant and product of the stoichiometric coefficient for the species i in the kth elementary reactions, respectively. I is the number of the elementary reactions. The reaction rate w_i is determined by the total of the rate of progress variable q_k.

$$w_i = \sum_{k=1}^{K} (\nu''_{i,k} - \nu'_{i,k}) q_k \tag{2.23}$$

q_k can be written as:

$$q_k = k_{f_k} \prod_{i=1}^{I} [X_i]^{\nu'_{i,k}} - k_{r_k} \prod_{i=1}^{I} [X_i]^{\nu''_{i,k}} \tag{2.24}$$

In the above equation, k_{f_k} and k_{r_k} denote the forward and reverse rate constants. k_{f_k} is generally assumed to have Arrhenius temperature dependence.

$$k_{f_k} = A_k T^{\beta_k} \exp\left(\frac{-E_k}{R^0 T} \right) \tag{2.25}$$

Here, A_k, β_k and E_k denote the pre-exponential factor, the temperature exponent and the activation energy for each elementary reactions, respectively. k_{r_k} can be obtained by

$$k_{r_k} = \frac{k_{f_k}}{K_{c_k}} \tag{2.26}$$

and K_{c_k} the equilibrium constant is given by

$$K_{c_k} = K_{p_k} \left(\frac{P_{atm}}{RT} \right)^{\sum_{i=1}^{I} (\nu''_{i,k} - \nu'_{i,k})} \tag{2.27}$$

where K_{p_k} is obtained by using the entropy and the enthalpy of elementary reaction.

$$K_{p_k} = \exp\left(\frac{\Delta S_k}{R^0} - \frac{\Delta H_k}{R^0 T} \right) \tag{2.28}$$

In the above equation, ΔS_k and ΔH_k can be calculated as follows.

$$\frac{\Delta S_k}{R^0} = \sum_{i=1}^{I} (\nu''_{i,k} - \nu'_{i,k}) \frac{S_i}{R^0} \tag{2.29}$$

$$\frac{\Delta H_k}{R^0 T} = \sum_{i=1}^{I} (\nu''_{i,k} - \nu'_{i,k}) \frac{H_i}{R^0 T} \tag{2.30}$$

Three body reactions

In some chemical reactions, a third body element may be required to advance the reaction as the following equation,

$$\mathrm{H} + \mathrm{O_2} + \mathrm{M} \Longleftrightarrow \mathrm{HO_2} + \mathrm{M}$$

when a third body element is needed, Eq. (2.25) becomes

$$q_k = \left(\sum_{i=1}^{I} \alpha_{i,k} [X_i] \right) \left(k_{f_k} \prod_{i=1}^{I} [X_i]^{\nu'_{i,k}} - k_{r_k} \prod_{i=1} I [X_i]^{\nu''_{i,k}} \right) \tag{2.31}$$

In the above equation, $\alpha_{i,k}$ is the contribution of a third body element of the ith species in the kth reaction. $\alpha_{i,k}$ becomes 1 in the case of all species contribute the reaction equally as a third body, and the first term becomes

$$[M] = \sum_{i=1}^{I} [X_i] \tag{2.32}$$

Fall-off reaction

On certain conditions, some reaction rate expressions can depend on both pressure and temperature. The fall-off reaction can be given as an example for this condition. One may consider methyl recombination. The description of this reaction is CH_3 + CH_3 $\Longleftrightarrow$ C_2H_6 for the high-pressure limit. In the low-pressure limit, however, a third-body element is needed for the reaction to proceed. Therefore, the appropriate description for low-pressure limit is CH_3 + CH_3 + (M) $\Longleftrightarrow$ C_2H_6 + (M).

In this fall-of region, the parameters are given in Arrhenius form, for the high-pressure limit (k_∞) and the low-pressure limit (k_0), which can be written as:

$$k_0 = A_0 T^{\beta_0} \exp\left(\frac{-E_0}{R_c T}\right) \tag{2.33}$$

$$k_\infty = A_\infty T^{\beta_\infty} \exp\left(\frac{-E_\infty}{R_c T}\right). \tag{2.34}$$

The rate constant at any pressure is given by

$$k = k_\infty \left(\frac{P_r}{1+P_r}\right) F, \tag{2.35}$$

where the reduced pressure P_r can be given as,

$$P_r = \frac{k_0[M]}{k_\infty} \tag{2.36}$$

where $[M]$ is the mixture's concentration, when F=1, it becomes Lindemann form. In this DNS study, F is given by

$$\log F = \left\{1 + \left[\frac{\log P_r + c}{n - d(\log P_r + c)}\right]^2\right\}^{-1} \log F_{\text{cent}} \tag{2.37}$$

The constants in the above equation are

$$c = -0.4 - 0.67 \log F_{\text{cent}} \tag{2.38}$$

$$n = 0.75 - 1.27 \log F_{\text{cent}} \tag{2.39}$$

$$d = 0.14 \tag{2.40}$$

F_{cent} can be expressed as a function of temperature:

$$F_{\mathrm{cent}} = (1-\alpha)\exp\left(\frac{-T}{T^{***}}\right) + \alpha\exp\left(\frac{-T}{T^{*}}\right) + \exp\left(\frac{-T^{**}}{T}\right). \tag{2.41}$$

2.2.3 Thermodynamic properties

In the present DNS, temperature dependence of the viscosity, the thermal conductivity and the diffusion coefficients are taken into account by linking the CHEMKIN-II packages [55, 56] with modifications for vector/parallel computations. This package assumes that the thermodynamic properties are only functions of temperature and given in terms of polynomial fits to the molar heat capacities at a constant pressure condition:

$$\frac{C_{p,i}}{R^0} = \sum_{n=1}^{N} a_{n,i} T^{(n-1)} \tag{2.42}$$

The standard-state molar enthalpy is given by

$$H_i = \int_0^T C_{p,i} dT \tag{2.43}$$

by substituting the Eq. (2.42) into Eq. (2.43), the following equation can be obtained:

$$\frac{H_i}{R^0 T} = \sum_{i=1}^{N} \frac{a_{n,i} T^{(n-1)}}{n} + \frac{a_{N+1,i}}{T} \tag{2.44}$$

In the above equation, the integrated constant $a_{N+1,i}$ is the standard enthalpy of formation at 0 K. However, since this polynomial representation near 0 K is not valid, this integrated constant is evaluated from the standard heat of formation at 298 K. Therefore, the enthalpy of each species can be written as:

$$H_i = \int_{298}^{T} C_{p,i} dT + H_i(298). \tag{2.45}$$

The entropy of each species can be obtained by integrating the specific heat and can be written as

$$S_i = \int_0^T \frac{C_{p,i}}{T} dT \tag{2.46}$$

and

$$\frac{S_i}{R^0} = a_{1,i} \ln T + \sum_{n=2}^{N} \frac{a_{n,i} T^{(n-1)}}{n-1} + a_{N+2,i} \tag{2.47}$$

where the constant of integration $a_{N+2,i}$ is at 298 K. $c_{p,i}$ and $\bar{c_v}$ are correlated to $C_{p,i}$ and are given as follows.

$$c_{p,i} = C_{p,i}/W_i \tag{2.48}$$

$$C_{v,i} = C_{p,i} - R^0 \tag{2.49}$$

$$c_{v,i} = C_{v,i}/W_i \tag{2.50}$$

$$\bar{c_v} = \sum_{i=1}^{I} c_v Y_i \tag{2.51}$$

2.2.4 Transport coefficients

The viscosity η_i, thermal conductivity λ_i and the binary diffusion coefficient D_{ij} for ith species are calculated by applying fitting procedure.

$$\ln \eta_i = \sum_{n=1}^{N} a_{n,i} (\ln T)^{n-1} \tag{2.52}$$

$$\ln \lambda_i = \sum_{n=1}^{N} b_{n,i} (\ln T)^{n-1} \tag{2.53}$$

$$\ln D_{ij} = \sum_{n=1}^{N} c_{n,i} (\ln T)^{n-1} \tag{2.54}$$

Here, the constant $a_{n,i}$, $b_{n,i}$ and $c_{n,i}$ are calculated by using TRANSPORT of CHEMKIN PACKAGE [56] for until $N = 4$. By using the calculated values of η_i, λ_i, the following equations can be given as:

$$\nu = \sum_{i=1}^{I} \frac{X_i \eta_i}{\sum_{j \neq i}^{I} X_j \Phi_{ij}} \tag{2.55}$$

$$\lambda = \frac{1}{2} \left(\sum_{i=1}^{I} X_i \lambda_i + \frac{1}{\sum_{i=1}^{I} X_i / \lambda_i} \right). \tag{2.56}$$

where,

$$\Phi_{ij} = \frac{1}{\sqrt{8}} \left(1 + \frac{W_i}{W_j}\right)^{-\frac{1}{2}} \left\{1 + \left(\frac{\eta_i}{\eta_j}\right)^{\frac{1}{2}} \left(\frac{W_j}{W_i}\right)^{\frac{1}{4}}\right\}^2 \tag{2.57}$$

2.2.5 Numerical methods

Figure 2.1 shows the schematic of numerical configuration with a high temperature ignition kernel. In order to form ignition kernel in the center of the domain, initial temperature distribution T_{ini} is given as Gaussian distribution. T_{ini} can be written as:

$$T_{\mathrm{ini}} = T_{\mathrm{pre}} + \left(T_{\mathrm{max}} - T_{\mathrm{pre}}\right) \exp\left(-\frac{r^2}{2\sigma_T^2}\right) \tag{2.58}$$

$$\frac{r_c^2}{2\sigma_T^2} = \ln\left(\frac{T_{\mathrm{max}} - T_{\mathrm{pre}}}{T_{\mathrm{ig}} - T_{\mathrm{pre}}}\right) \tag{2.59}$$

Here, T_{max}, T_{pre}, T_{ig}, r and σ_T denote the maximum temperature of the ignition kernel, preheat temperature, ignition temperature, radius of the ignition kernel and the standard deviation of the temperature distribution, respectively. DNS of hydrogen–air turbulent premixed flames have been conducted in two constant volume vessel configurations. Fully-developed homogeneous isotropic turbulence is used for initial velocity field. The initial flow field is obtained through preliminary DNS of decaying homogeneous isotropic turbulence by the spectral method with periodic boundary conditions. The initial Reynolds number is defined as

$$Re_\lambda = \frac{u'_{\mathrm{rms}}\lambda}{\nu} \tag{2.60}$$

$$Re_l = \frac{u'_{\mathrm{rms}}l}{\nu} \tag{2.61}$$

where u'_{rms}, l, λ and ν denote the root-mean-square of turbulent velocity, the integral length scale, the Taylor micro scale and the kinematic viscosity, respectively. The closed vessel is assumed to have a rectangular configuration, which is a simple idealized model for a real combustion chamber in engineering applications such as an automobile engine. The size of the vessels are $L_x \times L_y \times L_z = 20.0$

mm $\times$ 5.0 mm $\times$ 20.0 mm and 40.0 mm $\times$ 5.0 mm $\times$ 40.0 mm; they will be referred to as the small vessel and the large vessel, respectively hereafter. $N_x \times N_y \times N_z = 1025 \times 257 \times 1025$ and $2049 \times 257 \times 2049$ grid points are used in the small and large vessels, respectively. Each wall is named as follows: left wall ($x = 0$), right wall ($x = L_x$), lower wall ($y = 0$), upper wall ($y = L_y$), front wall ($z = 0$) and back wall ($z = L_z$), respectively. In reactive flow, spatial resolution is determined from laminar flame thickness which is the smallest scale. About 10 grid points should be contained to resolve the laminar flame thickness to calculate chemical reactions correctly. To determine spatial resolutions for the present three-dimensional DNS, preliminary two-dimensional DNSs have been conducted. Spatial resolutions of both cases are determined based on the laminar flame thickness and characteristics of turbulence in addition to the care of near wall phenomena. 24 grid points are within the laminar flame thickness and decreasing flame thickness due to pressure increase was taken into account. The detailed kinetic mechanism [57] including 12 reactive species (H_2, O_2, H_2O, O, H, OH, HO_2, H_2O_2, N_2, N, NO_2 and NO) and 27 elementary reactions is used for the hydrogen-air reaction. The DNS code developed in our previous studies [23, 24] is modified for wall-bounded flows. The governing equations are discretized using fourth-order central finite difference scheme in all directions, and can be written as follows:

$$\left(\frac{\partial f}{\partial x}\right)_i = \frac{-f_{i+2} + 8f_{i+1} - 8f_{i-1} + f_{i-2}}{12\Delta x} \tag{2.62}$$

$$\left(\frac{\partial f}{\partial y}\right)_j = \frac{-f_{j+2} + 8f_{j+1} - 8f_{j-1} + f_{j-2}}{12\Delta y} \tag{2.63}$$

$$\left(\frac{\partial f}{\partial z}\right)_k = \frac{-f_{k+2} + 8f_{k+1} - 8f_{k-1} + f_{k-2}}{12\Delta z} \tag{2.64}$$

The following equations are given for the domain boundaries.

$$\left(\frac{\partial f}{\partial x}\right)_1 = \frac{-25f_1 + 48f_2 - 36f_3 + 16f_4 - 3f_5}{12\Delta x} \tag{2.65}$$

$$\left(\frac{\partial f}{\partial x}\right)_2 = \frac{-3f_1 - 10f_2 + 18f_3 - 6f_4 + f_5}{12\Delta x} \tag{2.66}$$

$$\left(\frac{\partial f}{\partial x}\right)_{N_x-1} = \frac{3f_{N_x} + 10f_{N_x-1} - 18f_{N_x-2} + 6f_{N_x-3} - f_{N_x-4}}{12\Delta x} \tag{2.67}$$

$$\left(\frac{\partial f}{\partial x}\right)_{N_x} = \frac{25f_{N_x} - 48f_{N_x-1} + 36f_{N_x-2} - 16f_{N_x-3} + 3f_{N_x-4}}{12\Delta x} \tag{2.68}$$

$$\left(\frac{\partial f}{\partial y}\right)_1 = \frac{-25f_1 + 48f_2 - 36f_3 + 16f_4 - 3f_5}{12\Delta y} \tag{2.69}$$

$$\left(\frac{\partial f}{\partial y}\right)_2 = \frac{-3f_1 - 10f_2 + 18f_3 - 6f_4 + f_5}{12\Delta y} \tag{2.70}$$

$$\left(\frac{\partial f}{\partial y}\right)_{N_y-1} = \frac{3f_{N_y} + 10f_{N_y-1} - 18f_{N_y-2} + 6f_{N_y-3} - f_{N_y-4}}{12\Delta y} \tag{2.71}$$

$$\left(\frac{\partial f}{\partial y}\right)_{N_y} = \frac{25f_{N_y} - 48f_{N_y-1} + 36f_{N_y-2} - 16f_{N_y-3} + 3f_{N_y-4}}{12\Delta y} \tag{2.72}$$

$$\left(\frac{\partial f}{\partial z}\right)_1 = \frac{-25f_1 + 48f_2 - 36f_3 + 16f_4 - 3f_5}{12\Delta z} \tag{2.73}$$

$$\left(\frac{\partial f}{\partial z}\right)_2 = \frac{-3f_1 - 10f_2 + 18f_3 - 6f_4 + f_5}{12\Delta z} \tag{2.74}$$

$$\left(\frac{\partial f}{\partial z}\right)_{N_z-1} = \frac{3f_{N_z} + 10f_{N_z-1} - 18f_{N_z-2} + 6f_{N_z-3} - f_{N_z-4}}{12\Delta z} \tag{2.75}$$

$$\left(\frac{\partial f}{\partial z}\right)_{N_z} = \frac{25f_{N_z} - 48f_{N_z-1} + 36f_{N_z-2} - 16f_{N_z-3} + 3f_{N_z-4}}{12\Delta z} \tag{2.76}$$

The fourth order compact finite difference filter [58] is applied to eliminate unphysical oscillations with higher spatial frequencies than the spatial resolution.

$$\begin{aligned}\beta\hat{f}_{i-2} + \alpha\hat{f}_{i-1} + \hat{f}_i + \alpha\hat{f}_{i+1} + \beta\hat{f}_{i+2} \\ = af_i + \frac{d}{2}(f_{i+3} + f_{i-3}) + \frac{c}{2}(f_{i+2} + f_{i-2}) + \frac{b}{2}(f_{i+1} + f_{i-1})\end{aligned} \tag{2.77}$$

In the above equation, $\hat{f}_i$ denote the spatial derivative of filter f_i, in which transfer function $T(w)$ should satisfy where $T(\pi) = 0$. The transfer function is given in the following:

$$T(w) = \frac{a + b\cos(w) + c\cos(2w) + d\cos(3w)}{1 + 2\alpha\cos(w) + 2\beta\cos(2w)} \tag{2.78}$$

Where w represents the frequency. the coefficients α, β, a, b, c, d are obtained matching the Taylor series expansion coefficients. the coefficients a, b, c can be obtained by

$$a = \frac{1}{8}(5 + 6\alpha - 6\beta + 16d) \tag{2.79}$$

$$b = \frac{1}{2}(1 + 2\alpha + 2\beta - 2d) \tag{2.80}$$

$$c = -\frac{1}{8}(1 - 2\alpha - 14\beta + 16d) \tag{2.81}$$

where α, β and d are

$$\alpha = 0.475, \;\; \beta = 0, \;\; d = 0 \tag{2.82}$$

and the following is given for the domain boundaries.

$$\hat{f}_1 = \frac{15}{16}f_1 + \frac{1}{16}(4f_2 - 6f_3 + 4f_4 - f_5) \tag{2.83}$$

$$\hat{f}_2 = \frac{3}{4}f_2 + \frac{1}{16}(f_1 + 6f_3 - 4f_4 + f_5) \tag{2.84}$$

$$\hat{f}_{N-1} = \frac{3}{4}f_{N-1} + \frac{1}{16}(f_N + 6f_{N-2} - 4f_{N-3} + f_{N-4}) \tag{2.85}$$

$$\hat{f}_N = \frac{15}{16}f_N + \frac{1}{16}(4f_{N-1} - 6f_{N-2} + 4f_{N-3} - f_{N-4}) \tag{2.86}$$

The time integration is implemented by the third order Runge-Kutta scheme and can be written as follows:

$$\Delta u_k = \left(\frac{\partial u_k}{\partial t}\right) \times \frac{1}{3}\Delta t \tag{2.87}$$

$$u_{k'} = u_k + \Delta u_k \tag{2.88}$$

$$\Delta u_{k'} = \left\{-\frac{5}{9}\Delta u_k + \left(\frac{\partial u'_k}{\partial t}\right)\right\} \times \frac{15}{16}\Delta t \tag{2.89}$$

$$u_{k''} = u_{k'} + \Delta u_{k'} \tag{2.90}$$

$$\Delta u_{k''} = \left\{-\frac{153}{128}\Delta u_{k'} + \left(\frac{\partial u''_k}{\partial t}\right)\right\} \times \frac{8}{15}\Delta t \tag{2.91}$$

$$u_{k+1} = u_{k''} + \Delta u_{k''} \tag{2.92}$$

The reaction source terms in species conservation equations are advanced by the implicit method [59]. Both DNS are advanced at a constant 12 ns time step. For the boundary condition, isothermal and no-slip conditions given by the Navier-Stokes characteristic boundary condition (NSCBC) [60, 61] are imposed on the walls and the wall surfaces are supposed to be chemically inert (Boundary conditions for all species mass fractions are Neumann, i.e. zero gradients). As shown in Table 2.1, the preheating temperature, the wall temperature, the equivalence ratio and the initial pressure are set to 700 K, 450 K, 1.0 and 0.1 MPa, respectively. The initial distribution of species is assumed to be uniform. Other important numerical parameters are $u'_{rms}/S_L = 1.80$ and $l/\delta_F = 281$, where S_L and δ_F denote the laminar burning velocity and the laminar flame thickness. Both cases are classified inside the corrugated flamelets in the turbulent combustion diagram as shown in Fig. 2.2

Table 2.1: Numerical parameters for initial turbulence and combustion field

	Small Vessel	Large Vessel
Re_λ	97.1	
Re_l	516.2	
u'_{rms}	18.98 m/s	
l	2.465 mm	
λ	0.464 mm	
η	0.0243 mm	
$u'_{\mathrm{rms}}/S_{\mathrm{L}}$	1.84	
l/δ_{F}	281.2	
l/δ_{L}	5.42	
P_{ini}	0.1 MPa	
T_{ini}	700 K	
T_{wall}	450 K	
ϕ	1.0	
S_{L}	10.34 m/s	
δ_{F}	8.77 μm	
δ_{L}	0.470 mm	
$L_x \times L_y \times L_z$	20mm $\times$ 5mm $\times$ 20mm	40mm $\times$ 5mm $\times$ 40mm
$N_x \times N_y \times N_z$	1025$\times$257$\times$1025	2049$\times$257$\times$2049

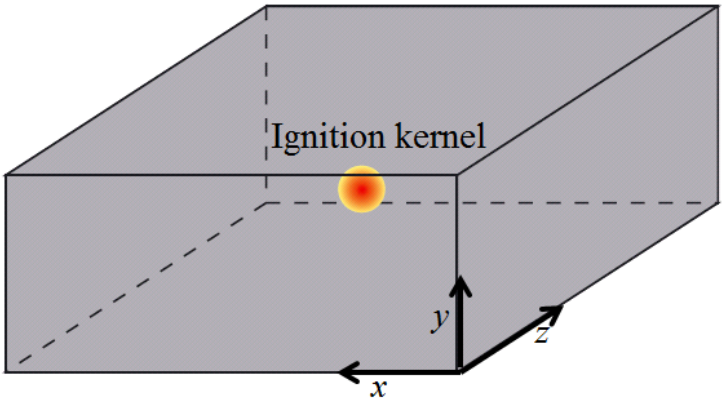

Figure 2.1: Schematic of computational domain.

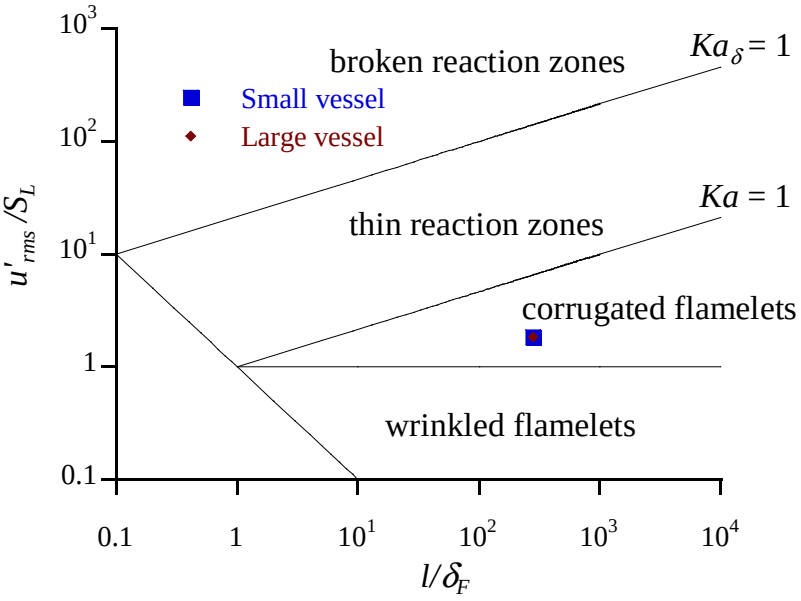

Figure 2.2: Turbulent combustion diagram.

2.3 Flame and flow behavior in a constant volume vessel

Figure 2.3 and Figure 2.4 show temporal developments of the heat release rate for the small vessel and the large vessel case by the volume rendering method. In the small vessel, at first, the flame ignites and propagates from the ignition kernel in a spherical shape on average. At $t = 96\mu s$, the flame front is already beginning to be stretched and distorted by turbulence and this almost spherical flame is going to impinge on the upper and the lower walls. In the following moments at $t = 150\mu s$ and $t = 240\mu s$, the flame propagates in an almost circular-disc shape on average. However, asymmetrical propagation can be observed because of inhomogeneous distribution of turbulent vortices in the initial field. In this phase, flame displacement speed parallel to the wall becomes higher than that of freely propagating flames due to expansion effect induced by the wall bounded field. At $t = 300\mu s$, the flame can only be found near the four corners of the vessel.

Figure 2.6 and Figure 2.7 show temporal developments of heat release rate in the center plane (a red-line plane in Fig. 2.5) with the second invariant of the velocity gradient tensor (A_{ij}) near the center plane (a blue-line box in Fig. 2.5) for the small and large vessel case, respectively. The velocity gradient tensor is given by

$$A_{ij} = \frac{\partial u_i}{\partial x_j} \tag{2.93}$$

the characteristic equation for the eigenvalues λ are

$$\lambda^3 + P\lambda^2 + Q\lambda + R = 0 \tag{2.94}$$

where P, Q and R denote the first, second and third invariant of the velocity

gradient tensor, respectively. They can be written as follows.

$$P = -(A_{11} + A_{22} + A_{33}) \tag{2.95}$$

$$\begin{aligned} Q &= \begin{vmatrix} A_{11} & A_{12} \\ A_{21} & A_{22} \end{vmatrix} + \begin{vmatrix} A_{11} & A_{13} \\ A_{31} & A_{33} \end{vmatrix} + \begin{vmatrix} A_{22} & A_{23} \\ A_{32} & A_{33} \end{vmatrix} \\ &= \frac{1}{2}(P^2 - trace[A^2]) = \frac{1}{2}(W_{ij}W_{ij} - S_{ij}S_{ij}) \end{aligned} \tag{2.96}$$

$$\begin{aligned} R &= \begin{vmatrix} A_{11} & A_{12} & A_{13} \\ A_{21} & A_{22} & A_{23} \\ A_{31} & A_{32} & A_{33} \end{vmatrix} \\ &= \frac{1}{3}(-P^3 + 3PQ - trace[A^3]) = \frac{1}{3}(-3W_{ij}W_{jk}S_{ki} - S_{ij}S_{jk}S_{ki}) \end{aligned} \tag{2.97}$$

S_{ij} and W_{ij} represent the symmetric and antisymmetric parts of A_{ij}, which can be written as

$$S_{ij} = \frac{1}{2}\left(\frac{\partial u_i}{\partial x_j} + \frac{\partial u_j}{\partial x_i}\right) \tag{2.98}$$

$$W_{ij} = \frac{1}{2}\left(\frac{\partial u_i}{\partial x_j} - \frac{\partial u_j}{\partial x_i}\right) \tag{2.99}$$

The asterisk denotes normalization by u'_{rms} and the Kolmogorov length scale (η) in the unburned side at each instant. The contour level is $Q^* = 0.01$. Due to dilatation and local pressure increase, fine scale vortices are found just outside the flame front. Tanahashi et al. [23] showed that fine scale eddies in turbulence have a great contribution to flame wrinkling and increase in heat release rate. As shown in Fig. 2.6-2.7, fine vortices make the flame front more complicated and increase the flame surface area. It should be noted that Re_λ does not decrease so far because of the high temperature and pressure induced by the flame propagation in a constant volume.

Temporal developments of mean pressure in the small and large vessels are shown in Fig. 2.8. The mean temperature is determined by the balance of a total heat quantity generated by the chemical reactions and a total heat loss from the wall. Here, mean pressure is defined as pressure averaged in the whole vessel whereas the mean temperature is defined as temperature averaged in the unburned

side of the vessel. For both cases, the temporal development of the mean pressure has a similar tendency. In the early stage, the total heat loss from the wall due to the difference between the preheating and wall temperature is slightly larger than the total heat quantity generated by chemical reactions. Therefore, the mean pressure values in both cases slightly decrease with decrease in the mean temperature. Then, the mean pressure starts to increase and rise quickly with rapid increase in total heat quantity generated by chemical reactions during the rapid combustion. In the large vessel case, the increasing rate of the mean pressure is slower than that in the small vessel case because the volume of the vessel is 4 times larger. For both cases, since the preheating temperature is set to 700 K, the pressure increase is expected to be a factor of 3.

In Fig. 2.9, temporal developments of the Reynolds number based on Taylor micro scale Re_λ = u'_{rms} λ / ν is shown. Here, u'_{rms}, λ and ν are averaged in the unburned side. At first, Re_λ drastically decreases from the initial condition for both vessels. This is because the homogeneous isotropic turbulence is filled in the vessel at the initial condition, and the turbulence decays especially near the wall. After that, Re_λ fluctuates with time but shows almost a constant value until the mean pressure begins to increase at $t = 120\mu s$ and $t = 200\mu s$ for the small and large vessels, respectively. In the small vessel, after the flame ignition, the turbulent intensity in the unburned side is determined by the balance between enhancement of turbulence due to local pressure increase by the dilatation and decay of turbulence especially near the walls. The turbulent intensity in the unburned side decreases almost linearly with fluctuation as shown in Fig. 2.10 while the Taylor micro scale in the unburned side increases, which can be seen in Fig. 2.11 with almost a constant averaged kinematic viscosity which can be seen in Fig. 2.12. The product of u'_{rms} and λ is almost constant until $t = 120\mu s$. After $t = 120\mu s$, the turbulent intensity in unburned side continues to decrease, but the rate of decrease becomes slower with the mean pressure increase. The Taylor micro scale averaged in the unburned side starts to decrease, while the kinematic viscosity drastically decreases with a rapid increase in the mean pressure in the unburned side. In the

large vessel case, Re_λ shows similar tendency to the small vessel case. Re_λ starts to increase as the mean pressure increases, and then shows a quick decrease as the flame reaches the side walls. In Fig. 2.10, in the large vessel, the turbulent intensity in the unburned side is almost constant during $t = 200 - 360\mu s$ and the Taylor micro scale averaged in the unburned side increases almost linearly after the mean pressure increases. Consequently, the maximum value of Re_λ for the large vessel case is much higher than that in the small vessel case.

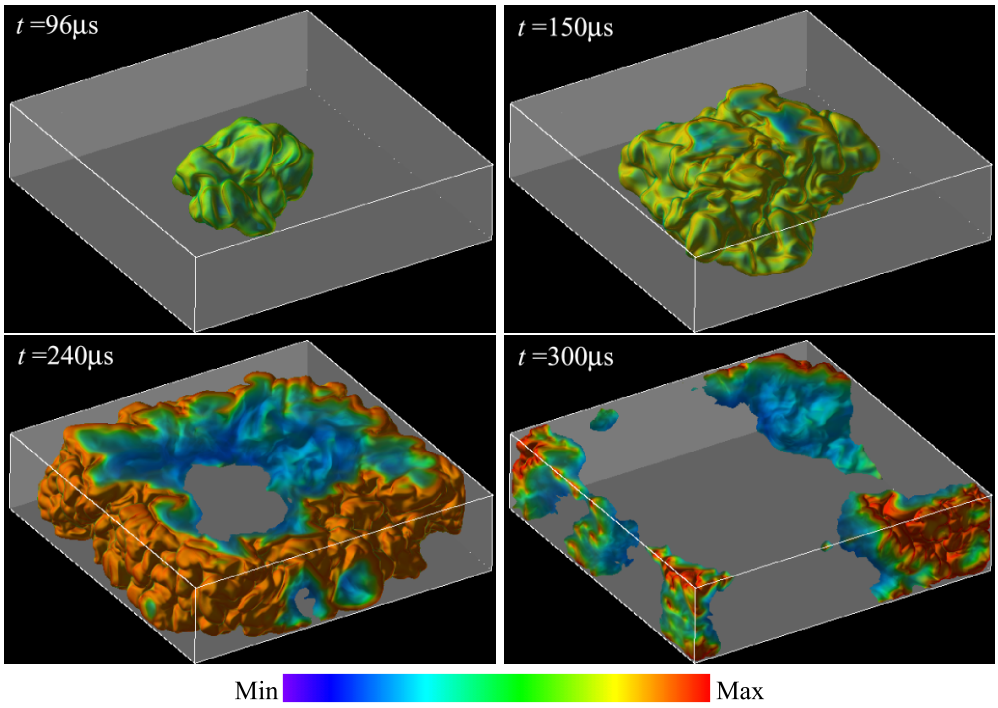

Figure 2.3: Temporal development of the heat release rate for the small vessel. Volume rendering method is used for visualization.

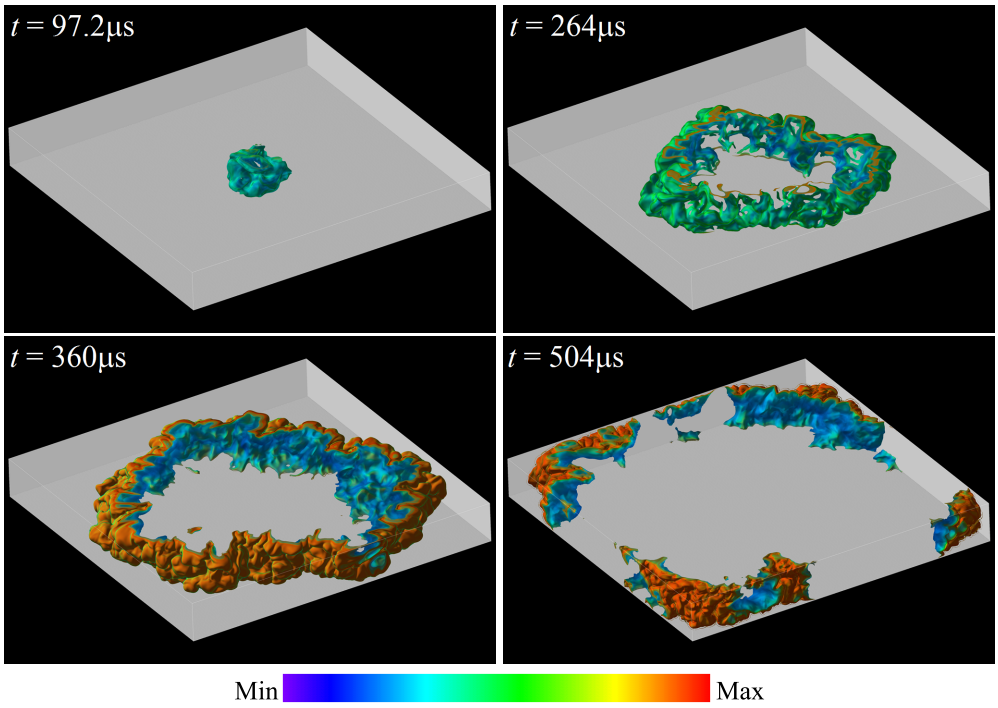

Figure 2.4: Temporal development of the heat release rate for the large vessel. Volume rendering method is used for visualization.

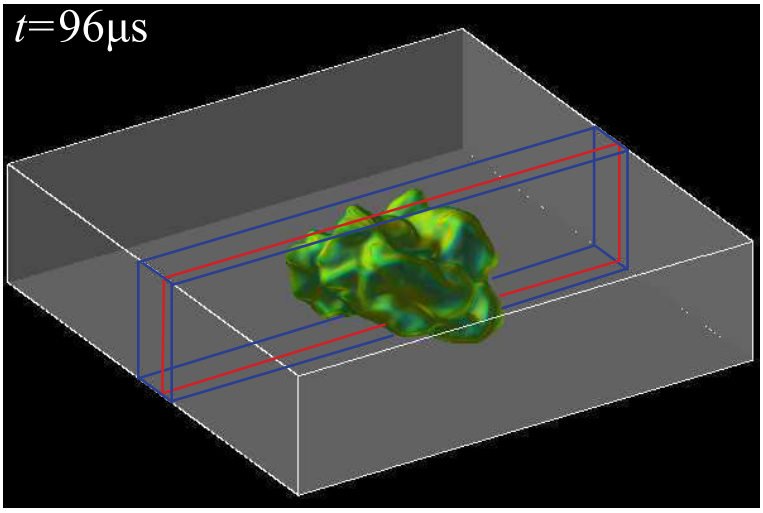

Figure 2.5: A red-line center plane and a blue-line box near the center plane.

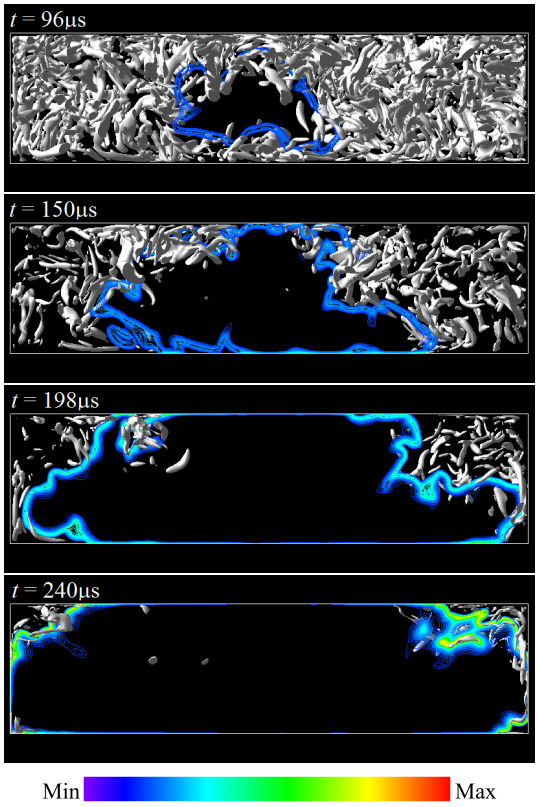

Figure 2.6: Temporal development of the heat release rate in the center plane and turbulent vortices near the center plane in the small vessel ($Q^* = 0.01$).

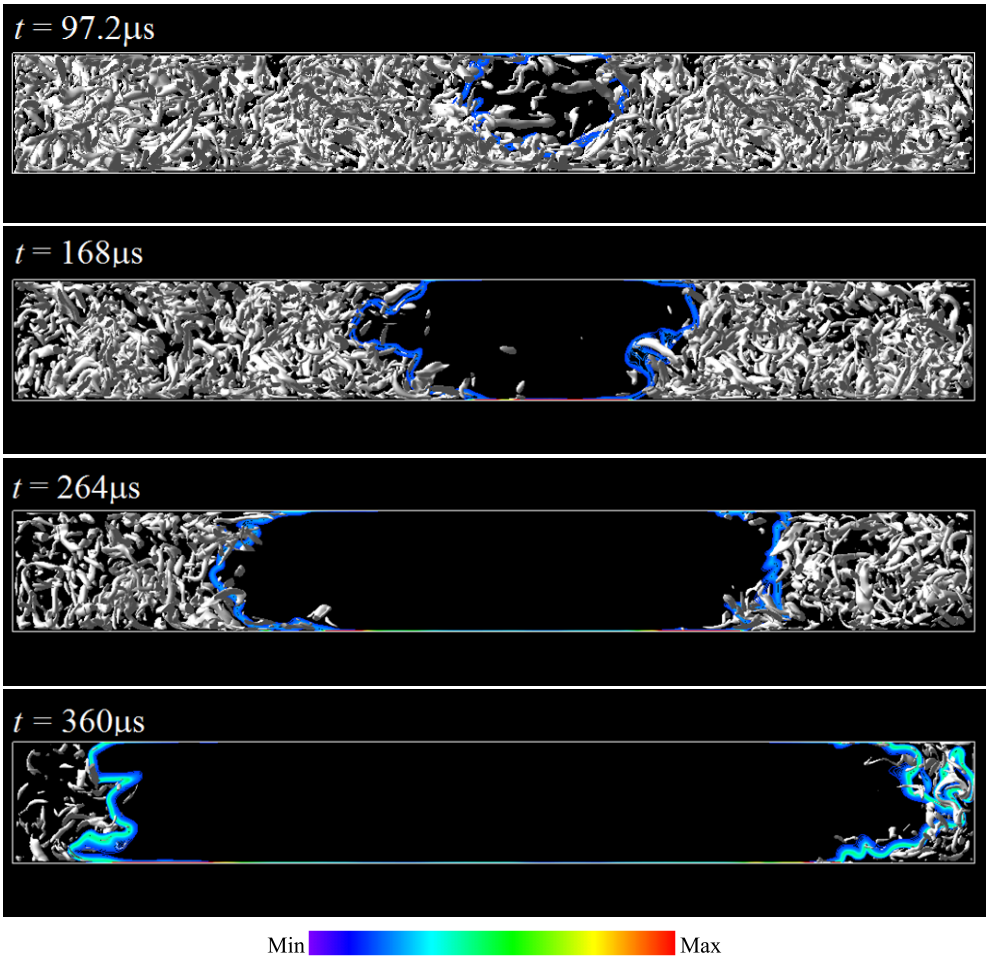

Figure 2.7: Temporal development of the heat release rate in the center plane and turbulent vortices near the center plane in the large vessel ($Q^* = 0.01$).

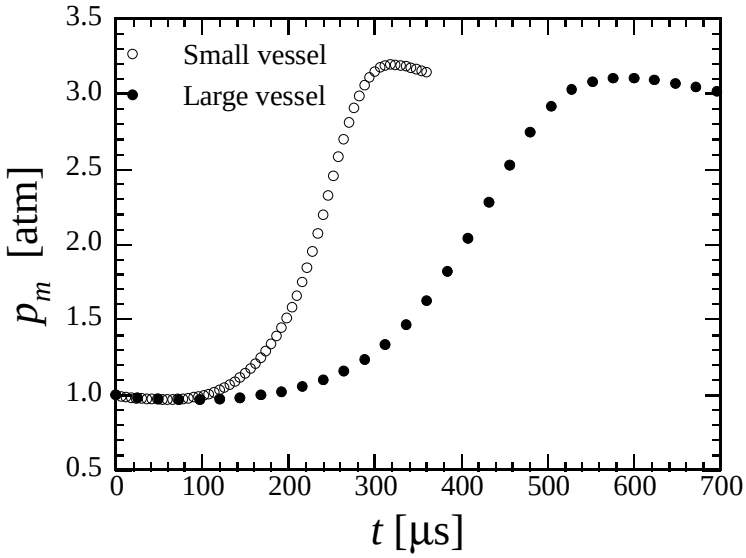

Figure 2.8: Temporal developments of mean pressure in the small and large vessels.

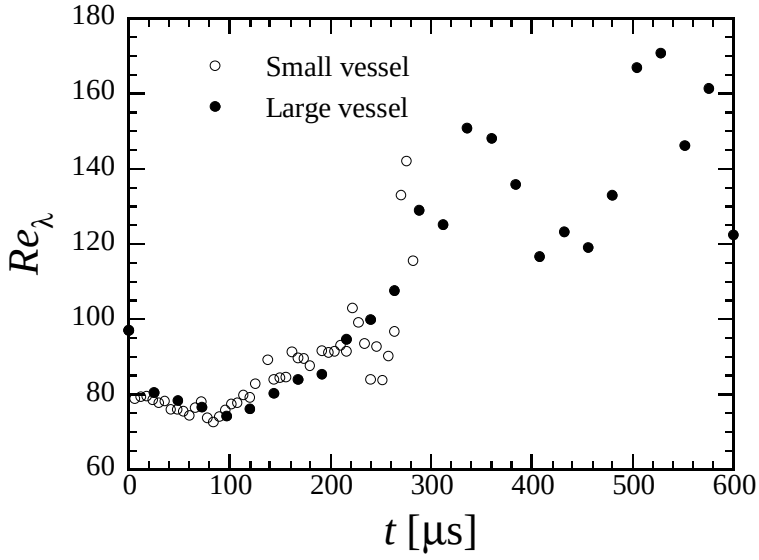

Figure 2.9: Temporal developments of Reynolds number based on Taylor micro scale in the small and large vessels.

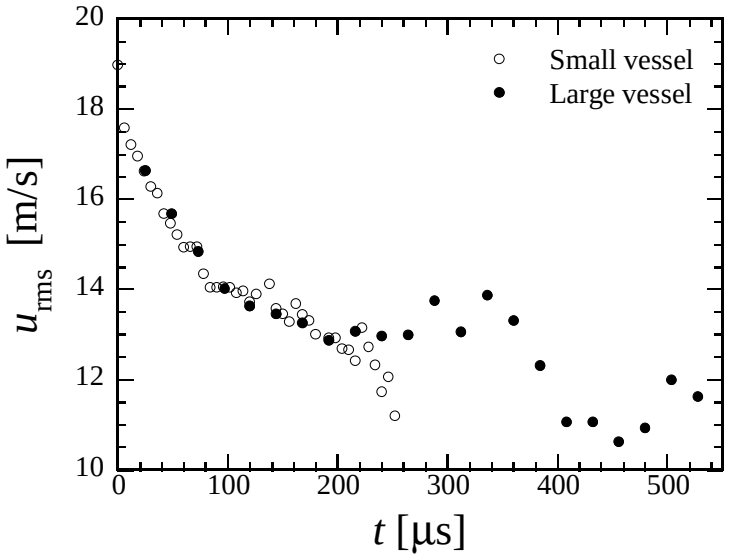

Figure 2.10: Temporal developments of mean turbulent intensity in the small and large vessels.

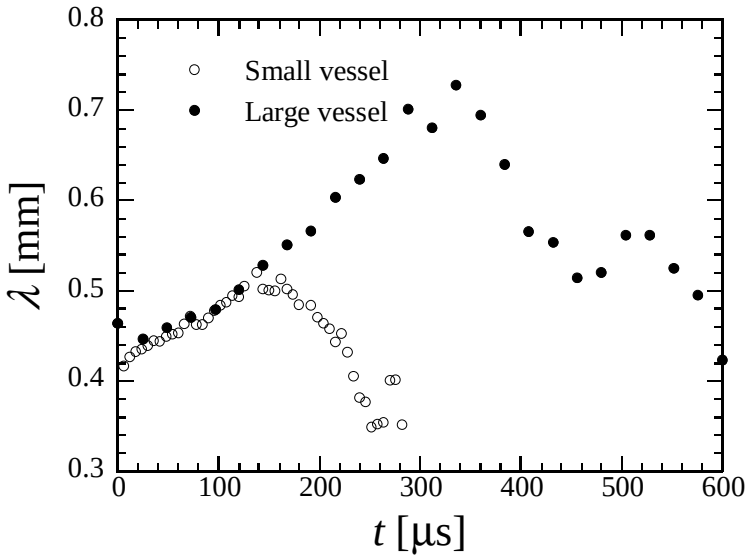

Figure 2.11: Temporal developments of Taylor micro scale in the small and large vessels.

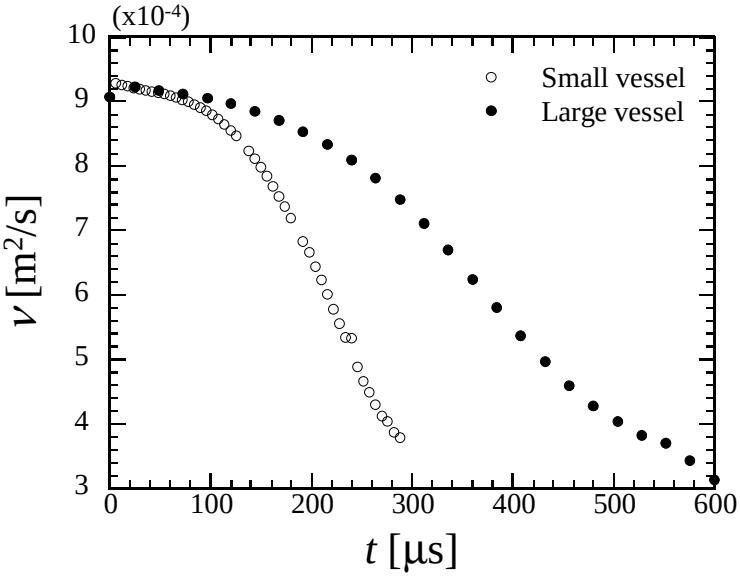

Figure 2.12: Temporal developments of mean kinematic viscosity in the small and large vessels.

2.4 Heat flux and total heat loss in a constant volume vessel

2.4.1 Effects of pressure on wall heat flux

Figure 2.13 shows temporal developments of heat flux distribution on the lower wall for the large vessel case. Heat flux is defined as the product of thermal conductivity and temperature gradient on the wall. The wall heat flux can be written as follows:

$$\phi = -\lambda \nabla T \tag{2.100}$$

As the wall temperature is much lower than the preheating temperature of the mixture, a thermal boundary layer develops at first. During this period of time, low temperature regions near the wall are stretched and disturbed by turbulent eddies. While the thermal boundary layer develops, heat flux on the wall facing unburned mixture increases gradually, which is reflected by heat flux fluctuations in no flame region. When the flame impinges on a wall, wall heat flux induced by the flame front increases much more drastically than that induced by a thermal boundary layer. As the flame propagates, it can be understood from the maximum values of the heat flux that the shape of the flame front becomes complicated and the maximum value becomes higher due to increase in mean pressure in the vessel. Figure 2.14 and Figure 2.15 show temporal developments of the maximum heat flux on each wall for the both cases. It can be found that heat flux on the upper and lower walls increases earlier than on the other walls because of the rectangular vessel configuration. For the large vessel case, the rapid rises can be observed at around $t = 73.2$ μs and 120 μs on the upper and the lower wall, at around $t = 336$ μs, 384 μs, 408 μs and 432 μs on the right, front, back and left wall, when the flame impingement occurs, respectively. By comparison with the small vessel case, it is found that the sequence of flame impingement differs greatly from that in the large vessel. This results from the distinct inhomogeneous distribution of turbulent vortices in the initial field. The maximum heat flux on each wall

demonstrates similar tendency after the flame impingement occurs. Owston et al. [53] showed that the maximum wall heat flux increases significantly (168% for H_2-O_2 flames in laminar cases.) when pressure increases by a factor of 2. Figure 2.16 shows temporal developments of the maximum wall heat flux on the lower wall in the both vessels. After the flame impingement, the maximum heat flux on the lower wall increases almost linearly with the mean pressure and has nearly same values for the same mean pressure for both cases. This is due to the decrease in flame thickness, which results in higher heat release rather than change in thermal boundary layer. These suggest a possibility that wall heat flux may be described as a function of mean pressure. However, it was shown that heat flux increases with pressure in nonlinear fashion in methane flame case [62].

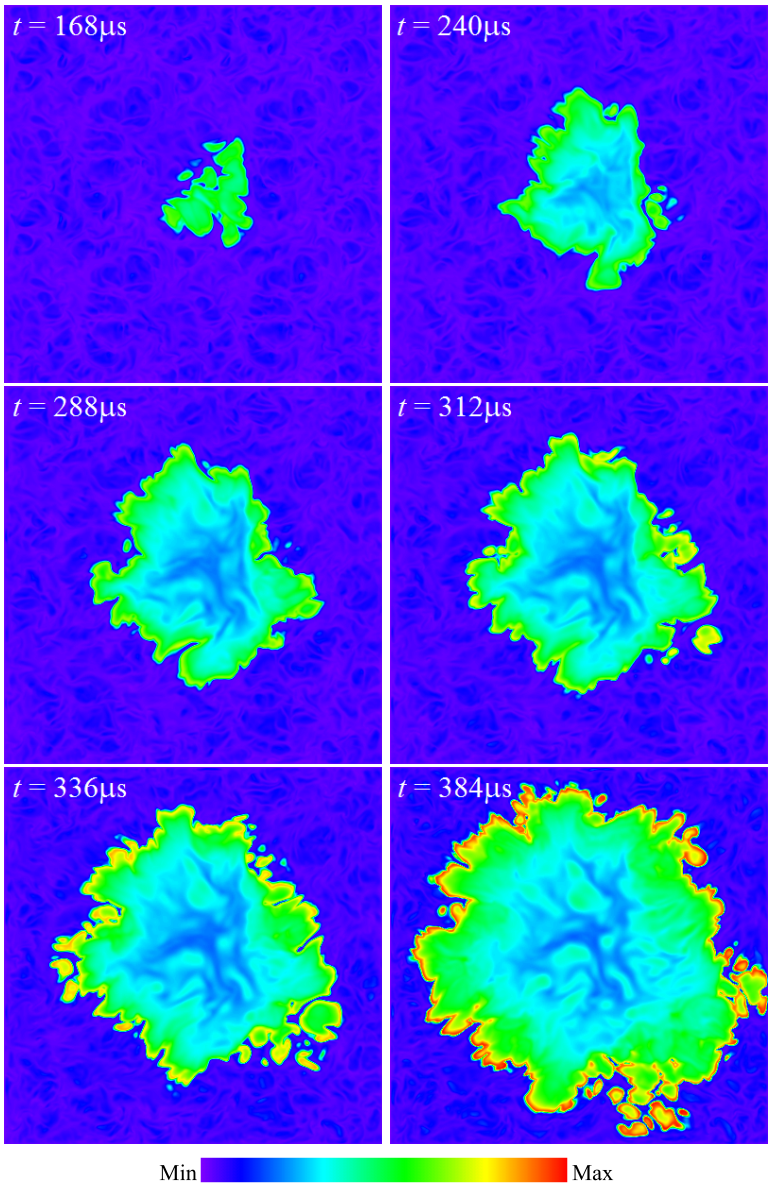

Figure 2.13: Temporal developments of heat flux distribution on the lower wall for the large vessel case.

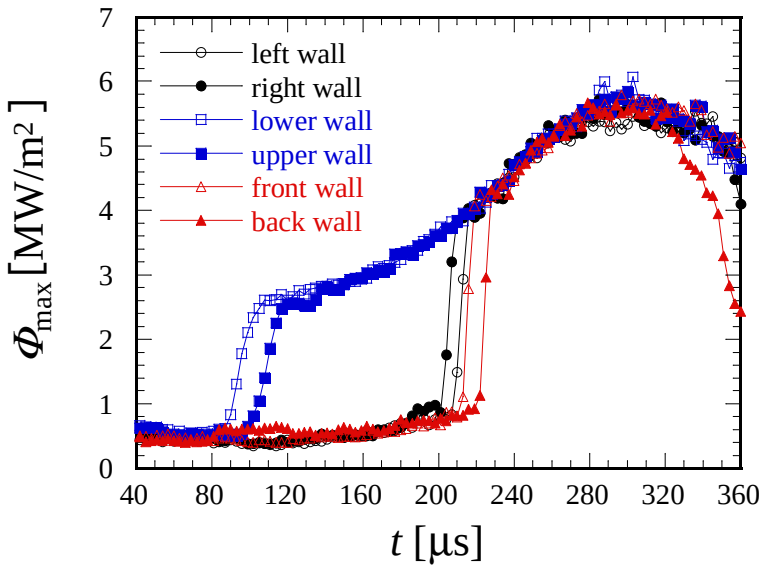

Figure 2.14: Temporal developments of the maximum heat flux on each wall for the small vessel case.

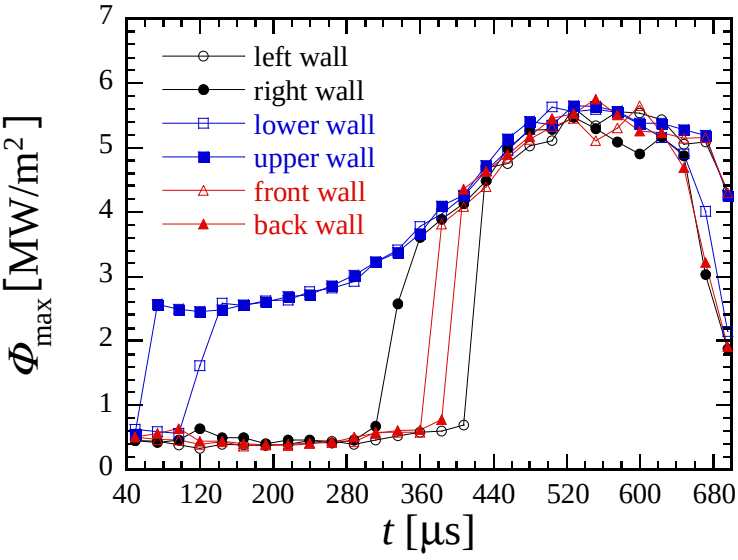

Figure 2.15: Temporal developments of the maximum heat flux on each wall for the large vessel case.

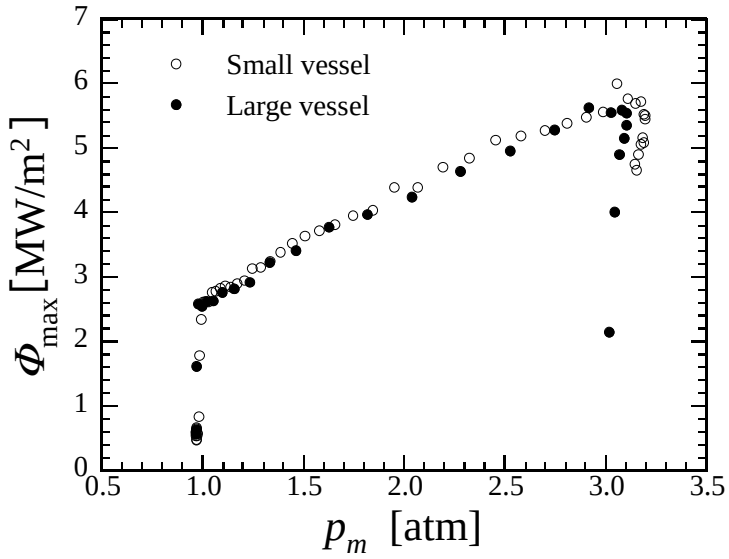

Figure 2.16: The maximum wall heat flux on the lower wall as a function of mean pressure for the small and large vessels.

2.4.2 Total heat loss in a constant volume vessel

In order to investigate the effects of the vessel size on the total heat loss and total fuel consumption, the results of large and small vessel cases are compared. A normalized total heat quantity generated by chemical reactions R_{reac} and a normalized total heat loss R_{loss} can be given by

$$R_{\mathrm{reac}} = \frac{Q_{\mathrm{reac}}}{Q_{298}} \tag{2.101}$$

$$R_{\mathrm{loss}} = \frac{Q_{\mathrm{loss}}}{Q_{298}} \tag{2.102}$$

where Q_{reac} and Q_{loss} denote the total amount of heat emitted by fuel which has already been consumed and transfered to all the wall surfaces, respectively. Q_{298} denotes the total internal energy of the initial input fuel at 298 K. Figure 2.17 denote the temporal developments of normalized total heat quantity generated by chemical reaction (R_{reac}). The rapid increase in R_{reac} is due to quick rise in the mean pressure and the flame surface area. About 90$\%$ of the initial fuel has been consumed for both cases although the vessel sizes are different. It takes almost two times longer to consume the same rate of fuel in the case the flame propagates in the larger vessel. The remainder of the fuel will be consumed slowly by the burned gas after the combustion is finished. Figure 2.18 shows temporal developments of R_{loss} for the two vessels. Since the combustion in the large vessel takes almost 2 times longer than that in the small vessel, the total heat loss is higher for large vessel and reaches about 17$\%$ of the total heat quantity generated by chemical reactions when the combustion is almost finished (R_{reac} = 0.9). Figure 2.19 demonstrates R_{reac} versus R_{loss}. In the early period, before the flame impinging the wall surfaces, heat loss is the result of difference between the wall temperature and the preheating temperature of the fuel. As the flame impinges to the upper and lower walls, heat loss increases quickly therefore the ratio of R_{loss} to R_{reac} increases for the both vessels. By the end of the rapid combustion, R_{reac} versus R_{loss} is higher for the large vessel case and R_{loss} reaches about 17$\%$. In Fig. 2.20, the normalized total heat loss as a function of mean pressure for the

both cases is shown. The total heat loss is higher for the large vessel case at the same pressure, this is due to the 4 times larger volume in the large vessel in which combustion takes longer time to reach the same pressure values.

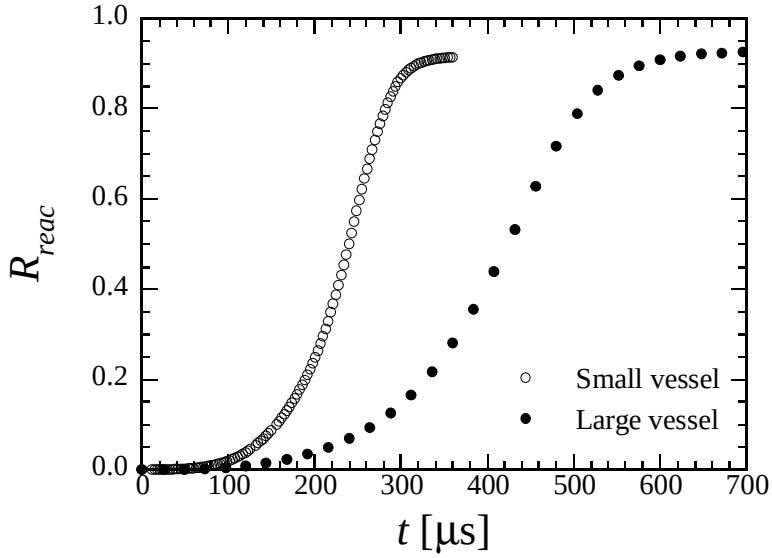

Figure 2.17: Temporal developments of R_{reac} for the small and large vessels.

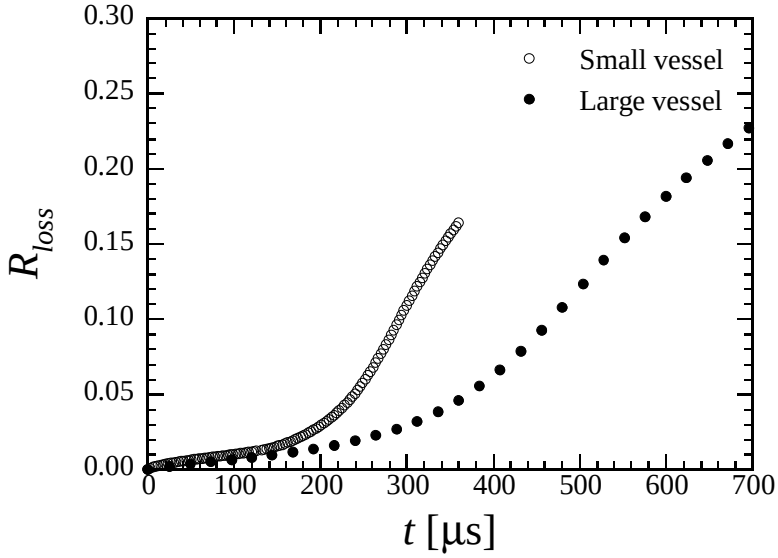

Figure 2.18: Temporal developments of R_{loss} for the small and large vessels.

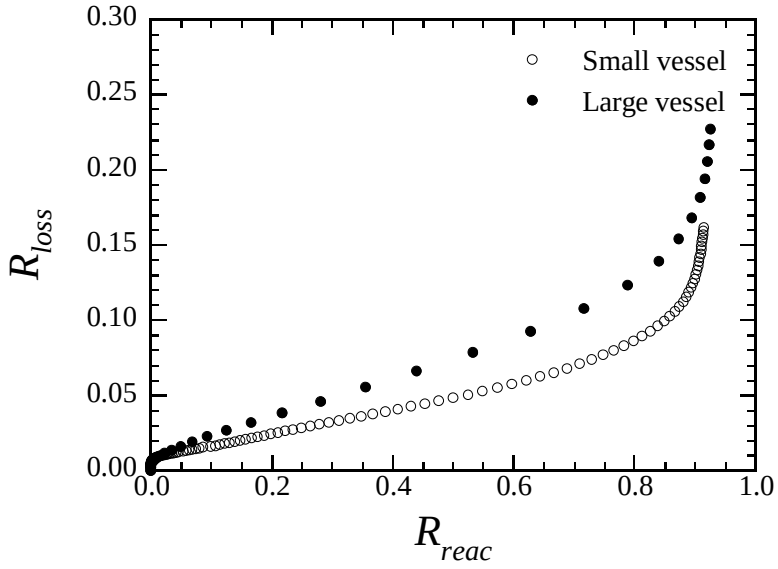

Figure 2.19: Temporal developments of R_{reac} versus R_{loss} for the small and large vessels.

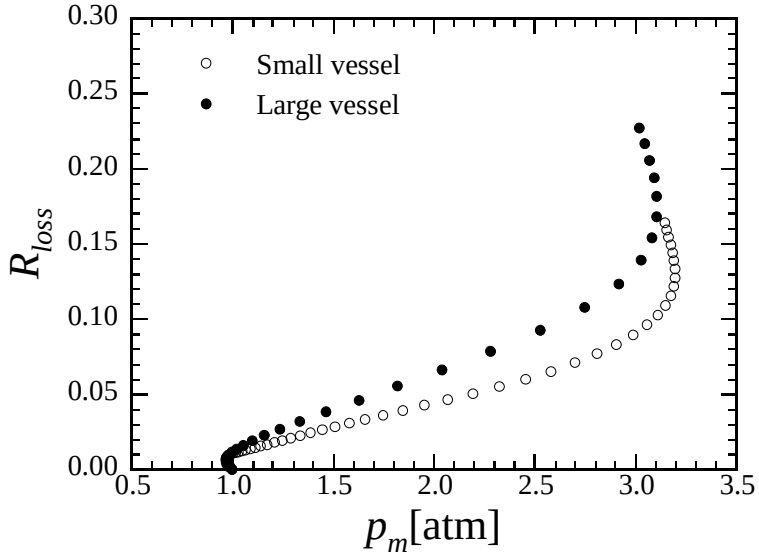

Figure 2.20: R_{loss} versus mean pressure for the both cases.

2.5 Statistical characteristics of local flame structure

To clarify effects of pressure increase on the local flame structure in a closed vessel, the statistical characteristics of flame elements are investigated. The flame front is defined as surfaces with local maximum temperature gradient, as in our previous studies [23, 24]. The local heat release rate (ΔH) increases and the local flame thickness (δ) decreases with time due to the mean pressure (p_m) and temperature increase in the vessel. It should be noted that, for corresponding laminar flame, maximum heat release rate (ΔH_L) increases and the flame thickness (δ_L) decreases with the pressure increase. Therefore, one-dimensional DNS of laminar flame propagation is conducted by adopting pressure and temperature averaged in the unburned side of the vessel as the inlet condition, to obtain the corresponding ΔH_L and δ_L at each time.

In order to show the pressure rising effect on the local flame elements more clearly, analyses are conducted at p_m = 1, 2 and 3 atm. Figure 2.21-2.22 show probability density functions (pdfs) of the local heat release rate normalized by corresponding ΔH_L for the small and large vessels, respectively. For the both cases, the pdfs of the heat release rate show peaks values around $1.0\Delta H_L$. These results are consistent with our previous researches on freely-propagating flame in homogeneous turbulence [23, 24] in which the pdfs of the heat release rate in the wrinkled flamelets and the corrugated flamelets show sharp peaks near $1.0\Delta H_L$. The maximum heat release reaches about $1.3\Delta H_L$ for the both cases.

Figure 2.23-2.24 show the pdfs of local flame thickness for the small and large vessels, respectively. Local flame thickness is defined by

$$\delta = \frac{T_b - T_u}{(\partial T/\partial \boldsymbol{n})_{max}} \tag{2.103}$$

where $\boldsymbol{n}$ denotes a unit vector normal to the flame front, and the subscripts u and b denote the unburned and burned sides, respectively. The flame thickness is normalized by the corresponding δ_L. With the flame propagation, since u'_{rms} decreases with increase of pressure, which was shown in Fig. 2.10, u'_{rms}/S_L de-

creases. In the turbulent combustion diagram [10], the flame conditions shift to the wrinkled flamelets region from the corrugated flamelets with the pressure increase as shown in Fig. 2.25. These results explain why the peak values of the pdfs of the local flame thickness approach δ_L at higher pressures for the both cases. Similarly, the probability of thicker flame elements decreases for high pressure.

It was observed by Kobayashi [63] that the Kolmogorov length scale (η) decreases with increasing pressure. In the present DNS, since the pressure changes as the flame propagates in the vessel, η values averaged in the unburned side are obtained as a function of mean pressure and are shown in Fig. 2.26. It can be seen that for the both cases, η decreases in a similar manner with increasing pressure.

Soika et al. [64] and Majid et al. [65] have conducted experiments and they have shown that the flame front curvature distribution broadens at elevated pressure conditions. In Fig. 2.27-2.28, the pdfs of the local mean curvature (k) on the flame front which is normalized by η for the both cases are shown at each pressure condition. The mean curvature is defined by

$$k = \frac{1}{R_1} + \frac{1}{R_2} \tag{2.104}$$

where R_1 and R_2 denote two curvature radiuses on the flame surface. The flame elements convex toward the unburned side have negative values. For the both cases, the most expected curvature for all pressure conditions show negative values. This indicates that flame elements tend to be convex toward the unburned side. This results from the almost spherical or circular-disc flame on average after the flame ignition at the center of the vessel. As shown in our previous DNS and experimental results [14, 23, 24, 33], the minimum curvature radius of the flame front is about of the order of the Kolmogorov scale, which also agrees with the present DNS.

Figure 2.29-2.30 show the pdfs of the tangential strain rate (a_t) to the flame front. a_t is defined by

$$a_t = \boldsymbol{t}_1\boldsymbol{t}_1 : \nabla \boldsymbol{u} + \boldsymbol{t}_2\boldsymbol{t}_2 : \nabla \boldsymbol{u} \tag{2.105}$$

where $\boldsymbol{t}_1$ and $\boldsymbol{t}_2$ denote unit vectors tangential to the flame front and satisfy a relation $\boldsymbol{t}_1 \cdot \boldsymbol{t}_2 = 0$. The tangential strain rate is normalized by Taylor time scale (u'_{rms}/λ) in the unburned side at each pressure condition. The positive and the negative strains represent stretch and compression, respectively. For the both cases, It can be observed that all pdfs skew to the positive side and the most expected tangential strain for all pressure conditions are about of the order of u'_{rms}/λ which was also the case in our previous study [23]. This means most of the flame elements tend to be stretched in the tangential direction and tangential strain can be scaled by u'_{rms}/λ.

These statistics of local flame elements suggest that the pressure change in the vessel is quickly reflected in characteristics of the local flame structure. This fact will be important for turbulent combustion models especially for large eddy simulation (LES).

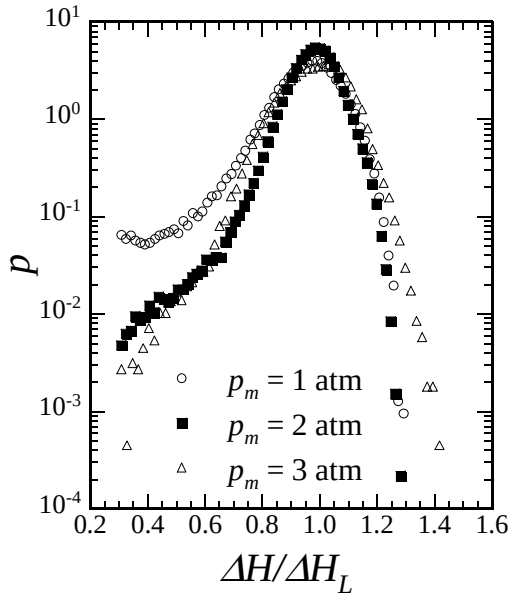

Figure 2.21: Probability density functions of the local heat release rate for the small vessel.

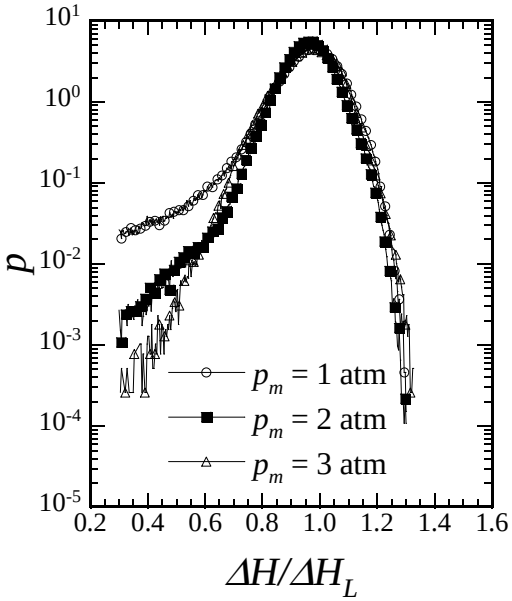

Figure 2.22: Probability density functions of the local heat release rate for the large vessel.

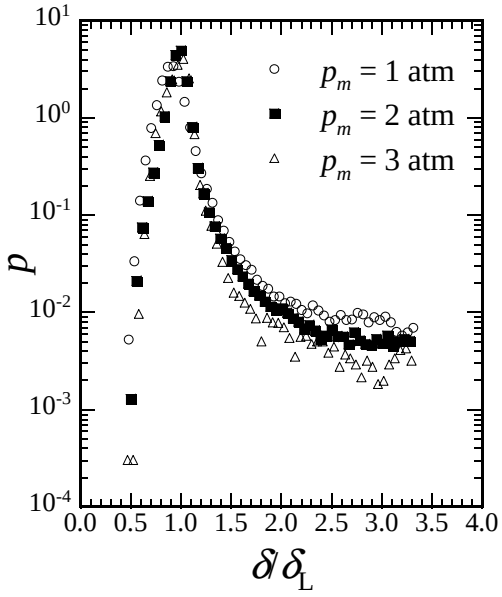

Figure 2.23: Probability density functions of the local flame thickness for the small vessel.

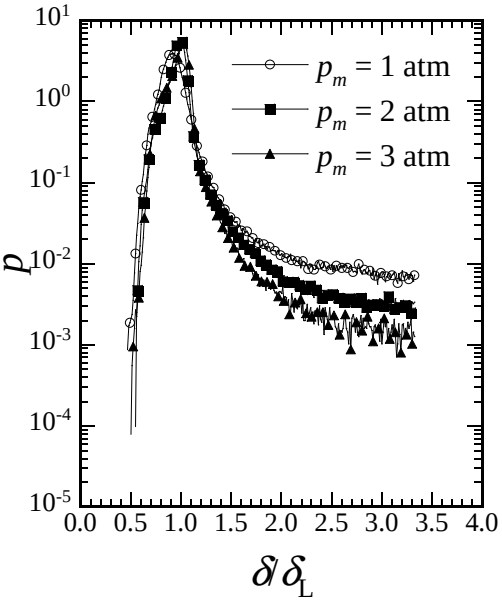

Figure 2.24: Probability density functions of the local flame thickness for the large vessel.

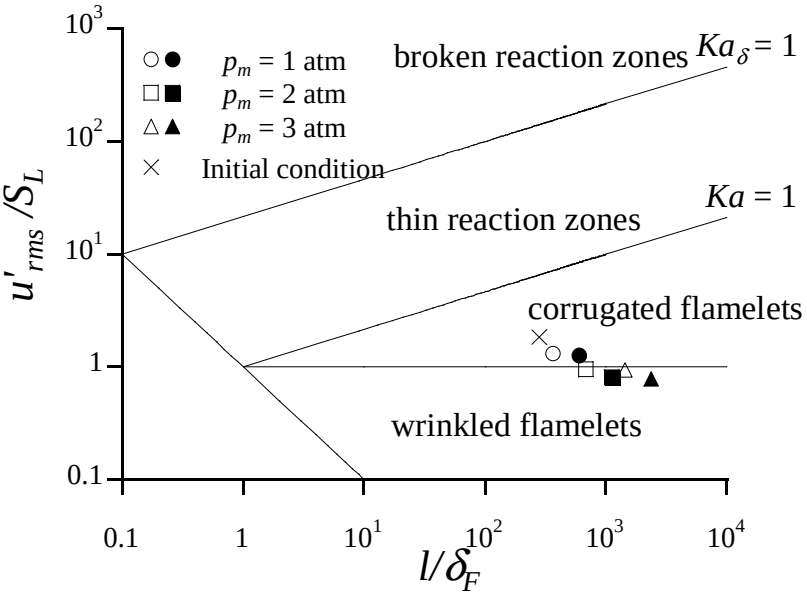

Figure 2.25: Flame conditions at different pressure in the turbulent combustion diagram for the small (open symbols) and large (closed symbols) vessels. Initial condition of both cases are also plotted.

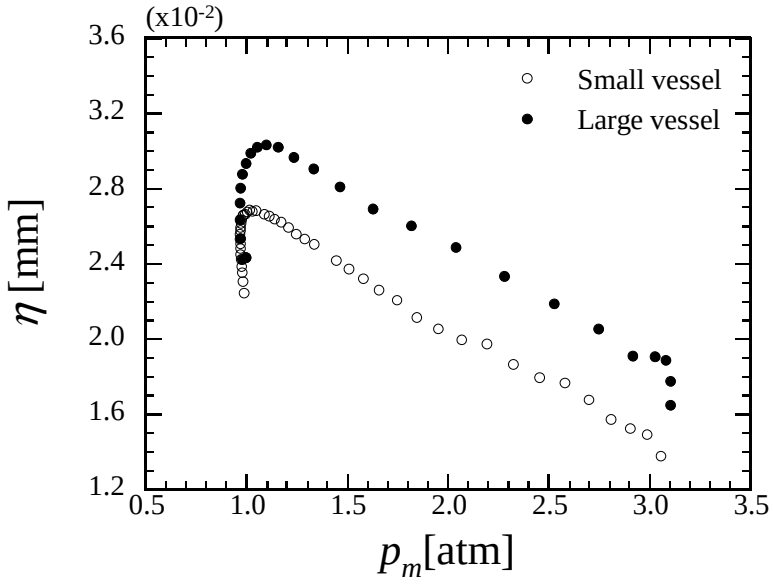

Figure 2.26: Kolmogorov length scale versus mean pressure for the both cases.

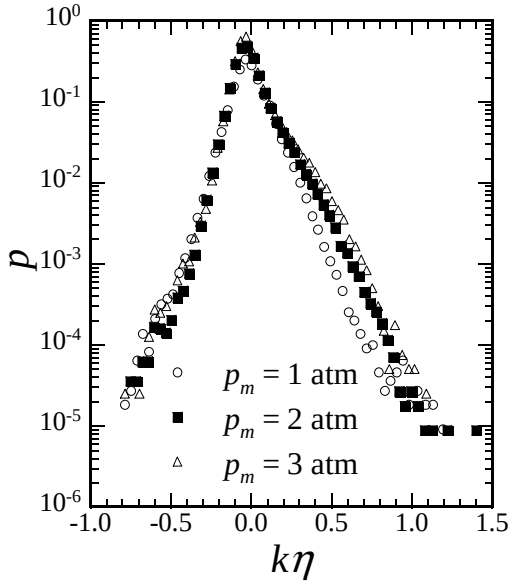

Figure 2.27: Probability density functions of the mean curvature for the small vessel.

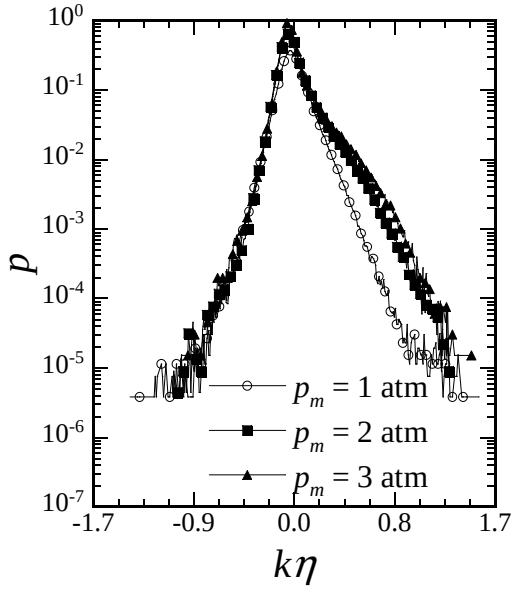

Figure 2.28: Probability density functions of the mean curvature for the large vessel.

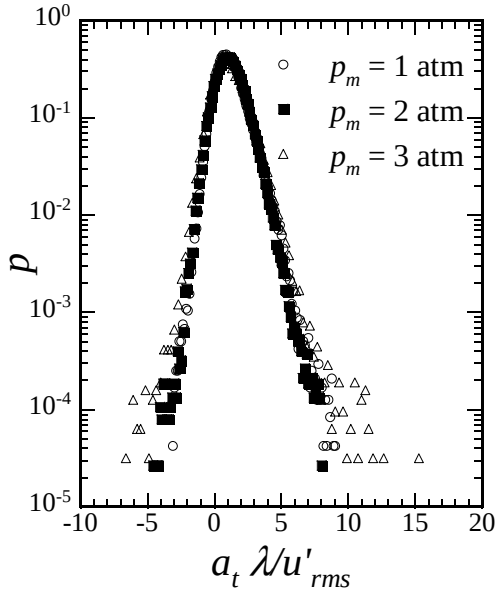

Figure 2.29: Probability density functions of the tangential strain rate for the small vessel.

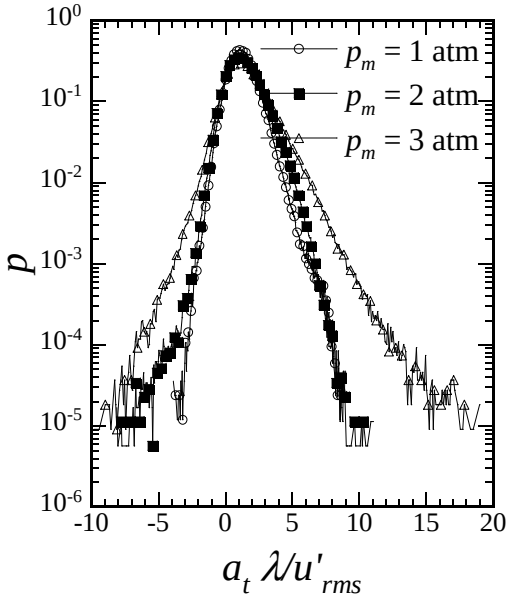

Figure 2.30: Probability density functions of the tangential strain rate for the large vessel.

2.6 Conclusions of this chapter

In this chapter, three-dimensional DNS of hydrogen–air turbulent premixed flames at relatively high Reynolds number in a constant volume vessel configuration has been conducted considering the detailed kinetic mechanism to investigate the turbulence–flame interaction under pressure rising conditions. The following conclusions are obtained:

(1) The pressure increase in the vessel reduces the flame thickness and enhances the heat release rate at the flame front. The local pressure increase due to dilatation also enhances turbulence and finer scale vortices which results in a more complicated flame surface and an increase in the flame surface area.

(2) The Reynolds number based on Taylor micro scale increases with the mean pressure in the vessel, as turbulent intensity decreases.

(3) The increase in the mean pressure enhances the wall heat flux. The maximum wall heat flux is approximately proportional to the mean pressure after the flame impinges on the wall, which suggests a possibility that the wall heat flux may be described as a function of pressure.

(4) Although the vessel sizes are different, 90$\%$ of the initial fuel has been consumed. However, when the combustion is almost over (R_{reac} = 0.9), heat loss is a little higher for the large vessel and reaches about 17$\%$, this could be attributed to the different aspect ratio of 2 vessels and 2 times longer combustion in the large vessel.

(5) Local heat release rate, flame curvature and tangential strain rate could be scaled by ΔH_L of the corresponding pressure, η and u'_{rms}/λ in the unburned side, respectively, even for the pressure rising condition.

Chapter 3

Direct numerical simulation of methane–air premixed flames in thin reaction zones

3.1 Preface

The characteristics of premixed flames are affected significantly by the length and the time scales of the flow field [7–9]. Therefore, to characterize premixed flames, the ratio of turbulent intensity (u'_{rms}) to laminar burning velocity (S_L) and the ratio of length scale of turbulence (l) to nominal laminar flame thickness (δ_F) are often used. With these two parameters, classification of particular flame regimes such as the wrinkled flamelets, the corrugated flamelets, the thin reaction zones and the broken reaction zones [10] can be made. In practical combustors, such as gas turbine and spark ignition engines, it is considered that turbulent flame is formed in the thin or broken reaction zones. Researchers are trying to attain a deeper understanding on local flame structure of turbulent premixed flames in these particular regimes in order to develop and validate proper combustion models for engineering applications. However, due to difficulties in measurement of turbulent flames in experiments, flame structures even in the thin reaction zones have not been clarified yet.

Remarkable progress in computational technologies in recent years enabled

researchers to conduct three-dimensional DNS of turbulent combustion with detailed chemistry. Three-dimensional DNS of hydrogen–air turbulent premixed flames with detailed chemistry have been conducted first in the world by Tanahashi et al. [23, 24] to investigate the local flame structure and the turbulence–flame interaction. Three-dimensional DNS of hydrocarbon flames with a detailed chemistry remains a challenge despite improvement in computational technology. Due to the high computational cost, several DNS have been done with a reduced kinetic mechanism adopting a low-Mach number approach. A complex chemistry which includes 20 species derived from GRI-Mech 1.2 mechanism and an adaptive time-dependent low-Mach number model was adopted and used by Bell et al. [40, 47, 49]. They have conducted three-dimensional DNS of lean methane–air premixed planar flames [49], a laboratory scale stoichiometric Bunsen flame [47] and a laboratory scale lean V-flame [40]. Carlsson et al. [66] recently conducted three-dimensional DNS of methane–air planar flames, a low-Mach number approximation with a reduced kinetic mechanism that includes 16 species and 25 reactions. Another low-Mach number approach, three-dimensional DNS of methane–air expanding turbulent flame with a reduced kinetic mechanism was conducted by Thevenin [50]. In order to develop higher accuracy of combustion models for industrial applications, it is necessary to have a better understanding of characteristics of flame elements with a more complex and detailed chemical mechanism. With this in mind, three-dimensional DNSs of turbulent premixed planar flames propagating in homogeneous isotropic turbulence is conducted with GRI-Mech 3.0 chemical mechanism [52] which includes 53 reactive species and 325 elementary reactions to investigate local flame characteristics of methane–air premixed flames classified into the thin reaction zones.

3.2 Direct numerical simulation

3.2.1 Numerical methods and initial conditions

In this chapter, three-dimensional DNSs of methane–air turbulent premixed flame have been conducted using GRI-Mech 3.0 kinetic mechanism [52], which includes 53 reactive species and 325 elementary reactions. The DNS code developed in our previous studies [23, 24] is used. The Soret effect, the Dufour effect, pressure gradient diffusion, bulk viscosity and radiative heat transfer are assumed to be negligible. Temperature dependence of the viscosity, the thermal conductivity and the diffusion coefficients is taken into account by linking the CHEMKIN packages [55, 56] with modifications for vector/parallel computations. Figure 3.1 shows a schematic of the computational domain. Navier–Stokes characteristic boundary condition (NSCBC) [60, 61] is used in the x direction and the periodic boundary conditions are applied in the $y-z$ directions. For the present compressible reacting flow cases, the governing equations, which have been discussed in section 2.2.1, are discretized by a fourth-order finite difference scheme in the x direction and a Fourier spectral method in the $y-z$ directions. Time integration is implemented by the third-order Runge–Kutta scheme. The reaction source terms in species conservation equations are advanced by the point implicit method [59]. The inflow boundary condition for the velocity field is given as $\boldsymbol{u}_{in}(y,z,t) = (\alpha S_L, 0, 0) + \boldsymbol{u}'(y,z,t)$, where, S_L is determined by preliminary one-dimensional calculations and can be written as follows.

$$S_L = \frac{1}{\rho_u Y_{CH_{4,u}}} \int \omega_{CH_4} dx \tag{3.1}$$

Here, ρ_u, $Y_{CH_4,u}$, ω_{CH_4} denote the density in the unburned side, the mass fraction of CH_4 in the unburned side and the reaction rate of CH_4, respectively. The turbulence $\boldsymbol{u}'(y,z,t)$ at the inflow boundary is given through a preliminary three-dimensional DNS of homogeneous isotropic turbulence with the spectral method and the periodic boundary conditions. α is a parameter which is determined from the ratio of the turbulent burning velocity (S_T) to S_L and is set to a constant value

which is determined to ensure the flame stays in the computation domain for a long time. In this regard, αS_L is nearly equal to S_T. S_T can be written as:

$$S_T = \frac{1}{\rho_u Y_{CH_{4,u}} L_y L_z} \iiint \omega_{CH_4} dxdydz \tag{3.2}$$

Numerical parameters for DNSs of methane–air turbulent premixed flames are presented in Table 3.1. Two flames are considered; a stoichiometric flame (Case 1) and a lean flame (Case 2). About 10 grid points should be contained to resolve the laminar flame thickness to calculate chemical reactions correctly, in this study, 22 grid points are within the laminar thermal flame thickness (δ_L) for both cases. δ_L is calculated by the maximum temperature gradient and can be written as follows:

$$\delta_L = \frac{T_b - T_u}{(\partial T/\partial x)_{max}} \tag{3.3}$$

Here, the subscripts u and b denote the unburned and burned sides of the domain, respectively. The initial Reynolds number is $Re_l = 144$ and $Re_\lambda = 37.4$. With the given initial parameters, the present methane–air premixed flames are classified into the thin reaction zones in the turbulent combustion diagram [10], as can be seen in Fig. 3.2.

For the present two cases, initial one-dimensional flames are calculated by Premix code package from Chemkin [67]. Since the grid sizes are non-uniform in Premix calculations, these results are used in one-dimensional DNS to obtain uniform grid size for the present three-dimensional DNSs. Distributions of mass fractions of major species CH_4, O_2, CO_2 and H_2O are shown in Fig. 3.3 (a-b) for the case 1 and the case 2, respectively. It can be seen that the results from one-dimensional DNS and Chemkin show good agreement along the flow direction.

Both DNSs are advanced at a constant 1.9 ns time step and conducted for long enough to construct statistically meaningful data. Temporal developments of S_T normalized by S_L for the both cases are shown in Fig. 3.4. τ_l is the turbulent mixing time or eddy turnover time, and τ_F is the flame time , time required for flame to pass its own thickness, can be written, respectively as:

$$\tau_l = l/u'_{rms} \tag{3.4}$$

$$\tau_F = \delta_L/S_L \tag{3.5}$$

In Fig. 3.4 (a), the time is normalized by τ_F, in Fig. 3.4 (b), the time is normalized by τ_l. As can be seen, the turbulent burning velocity increases with time for the both cases, and it has a higher value in the case 2 as the normalized turbulent intensity is relatively higher (u'_{rms}/S_L = 9.78). At the end of the computation, The S_T reaches about 2.55S_L and 2.59S_L for the case 1 and the case 2, respectively.

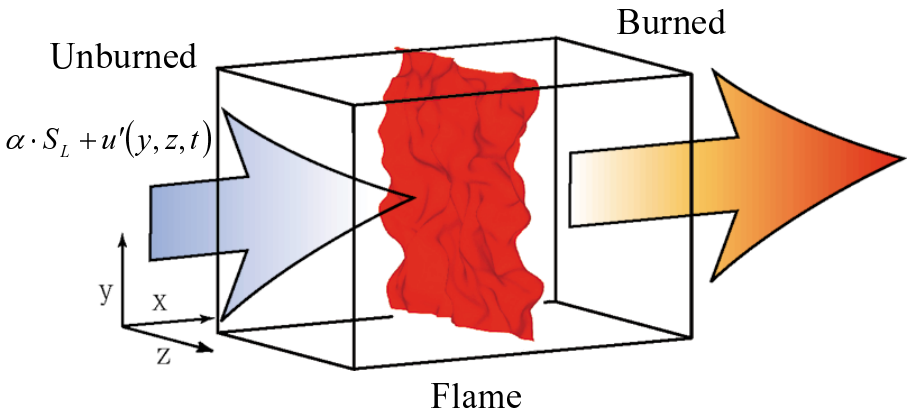

Figure 3.1: Schematic of computational domain.

Table 3.1: Numerical parameters for initial turbulence and combustion field

	Case 1	Case 2
Re_λ	37.4	
Re_l	144	
P_{ini}	0.1 MPa	
T_{ini}	950 K	
l	0.6559 mm	
λ	0.2299 mm	
η	0.0189 mm	
ϕ	1.0	0.6
u'_{rms}	25.28 m/s	25.04 m/s
$u'_{\mathrm{rms}}/S_{\mathrm{L}}$	7.14	9.78
l/δ_{F}	20.13	14.70
l/δ_{L}	2.62	2.14
S_{L}	3.54 m/s	2.56 m/s
δ_{F}	32.59 μm	44.63 μm
δ_{L}	0.25 mm	0.31 mm
$L_x \times L_y \times L_z$	11 mm $\times$ 4.4 mm $\times$ 4.4 mm	8.8 mm $\times$ 4.4 mm $\times$ 4.4 mm
$N_x \times N_y \times N_z$	961$\times$192$\times$192	641$\times$160$\times$160

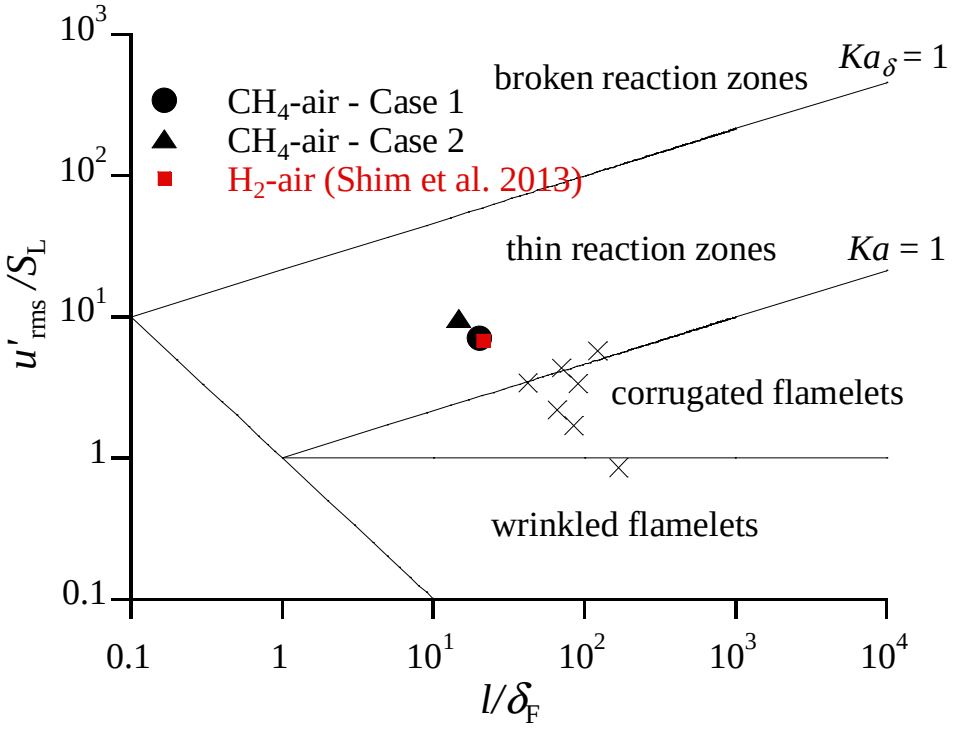

Figure 3.2: Turbulent combustion diagram. The cross symbols represent the previous DNS studies of H_2–air planar premixed flames [23, 24, 33, 37]

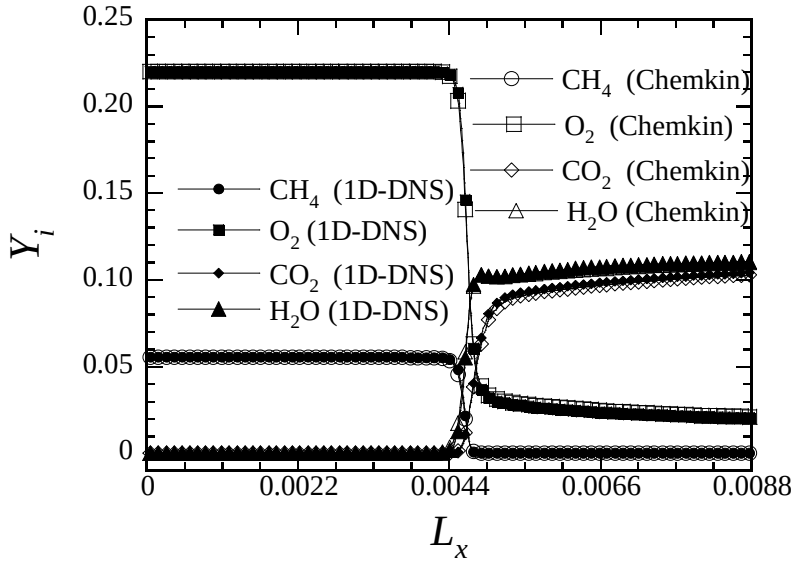

(a) Case 1

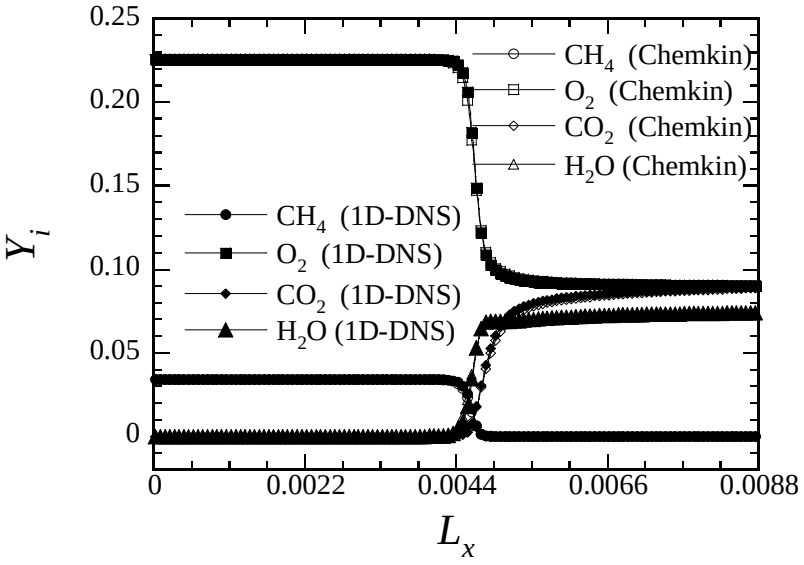

(b) Case 2

Figure 3.3: Distribution of mass fractions of major species for case 1 (a) and case 2 (b).

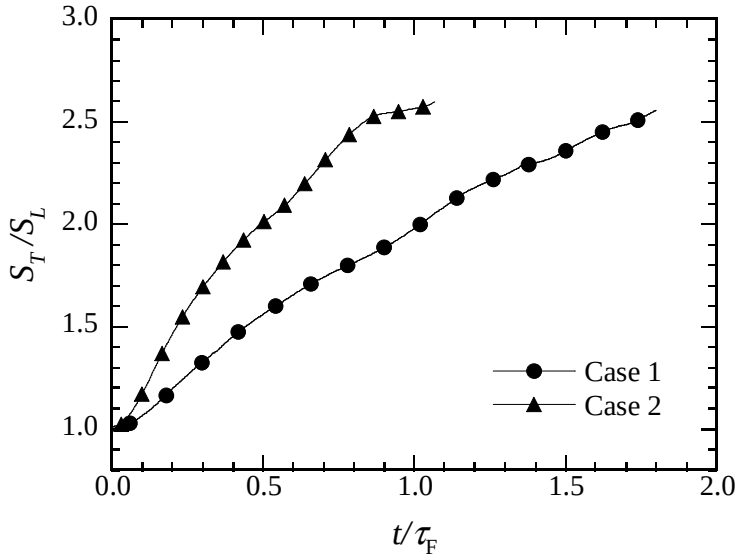

(a)

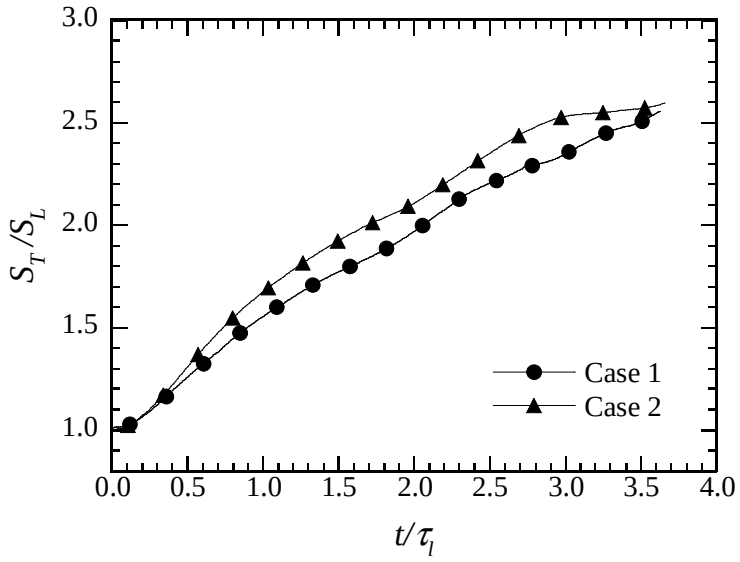

(b)

Figure 3.4: Turbulent burning velocity developments as a function of flame time (a) and eddy turnover time (b).

3.3 Local flame structures

Contour surface of temperature (T) with the second invariant (Q^*) of the velocity gradient tensor (A_{ij}) are shown in Fig. 3.5 for the case 1 and the case 2. Asterisk means normalization by u'_{rms} and the Kolmogorov length scale (η) in the unburned side. The contour levels are $Q^* = 0.01$ and T is set to 1944 K for the case 1 and 1675 K for the case 2, where the heat release rate shows the maximum value in the corresponding laminar flame. As shown here, fine vortices make the flame front more complicated and increase the flame surface area. The fine vortices cannot survive behind the flame front for the both cases due to the increase of viscosity and temperature rise in the burned region.

Figure 3.6-3.7 show the contour surface of the heat release rate ($\Delta H/\Delta H_L$) with the second invariant of the velocity gradient tensor for the case 1 and the case 2, respectively. ΔH is normalized by the maximum heat release rate of the corresponding laminar premixed flame (ΔH_L). Different contour levels are drawn for the both cases. As shown in Fig. 3.6-3.7 (a), in the both cases, large region of heat release rate lower than the corresponding laminar flame can be seen. These regions of low heat release rate do not indicate global extinction, as can be seen in Fig. 3.6-3.7 (b)-(c), their distributions show three-dimensionally connected structures, for the both cases.

For understanding the local flame characteristics of premixed methane–air flame in the thin reaction zones regime, the distribution of temperature (T), normalized heat release rate $\Delta H/\Delta H_L$ and mass fractions of OH and CH radicals on a typical plane for the case 1 are shown in Fig. 3.8. The typical plane means an $x-y$ or $x-z$ cross sectional plane which can represent the characteristics of each flame structure well. The corresponding laminar profile is shown in the bottom of each image. In the circled region in Fig. 3.8 , the concentration of OH is relatively low. However, heat release rate around 0.50-0.60ΔH_L and temperature around 1960 K can be found in the same region, which is indicated by arrows. In Fig. 3.9, the distributions of normalized heat release rate $\Delta H/\Delta H_L$ and mass fractions of

OH, CH and CH_2O radicals on a typical plane are shown for the case 2. In the circled region, heat release rate shows around 30%-50% that of laminar flame, while almost no OH and CH concentration can be observed and relatively high concentration of CH_2O can be found in the same region. It is difficult to measure this kind of flame structure if only OH is used to identify flame front in planar laser induced fluorescence (PLIF) measurements. These results actually reveal the limitations and drawbacks of OH, which is a commonly used flame marker in experiments. These sorts of flame structures in thin reaction zones could have significant effects on fractal analysis of the flame surface, which is one of the useful techniques to investigate characteristics of global flame structures and is often used for developments of turbulent combustion model for large eddy simulation (LES). Figure 3.10 shows scatter plots of normalized mass fractions of HCO versus normalized heat release rate ($\Delta H/\Delta H_L$). Values of the corresponding laminar flame are also plotted. HCO is known to be a good flame marker for methane–air premixed flames [68]. It can be observed that the mass fractions of HCO correlates well with heat release rate, which shows that HCO is a good flame marker as well, for the present stoichiometric and lean CH_4-air premixed flames in the thin reaction zones. Due to low signal to noise ratio of PLIF of HCO, it was proposed that simultaneous CH_2O-OH PLIF measurement is a good flame indicator [69] as pixel by pixel multiplication of CH_2O and OH correlates well with local heat release rate. Figure 3.11 shows pixel by pixel multiplication of mass fractions of CH_2O and OH versus local heat release rate. It can be seen that pixel by pixel multiplication of mass fractions of CH_2O and OH correlates well with local heat release rate for the both stoichiometric and lean methane–air premixed flames. Several studies on turbulent methane–air flames have used simultaneous CH-OH PLIF [14, 70] and CH_2O-OH PLIF [69, 71–76] measurements to identify local heat release rate and flame front. Therefore, simultaneous CH-OH or CH_2O-OH PLIF measurements may give more accurate results than single OH PLIF on the flame front measurement in thin reaction zones.

For methane–air flames, many chemical species have different time scales.

In order to clarify how turbulence influences each chemical species, the ratio of turbulence time scale to chemical time scale [77] of each chemical species are drawn in Fig. 3.12-3.13 for the case 1 and the case 2, respectively. The turbulence time scale (τ_η) can be written as

$$\tau_\eta = \frac{D}{1.2u_k} \tag{3.6}$$

where D and u_k denote 8 times of η and the Kolmogorov velocity, respectively. τ_c denotes the chemical time scale of the reactive species i and is derived from the ratio of the maximum value of molar concentration and the maximum value of reaction rates of the chemical species i in the laminar flame. τ_c can be written as

$$\tau_{c_i} = \frac{[X_i]_{max}}{|\omega_i|_{max}} \tag{3.7}$$

The life time of reactive species are longer than the turbulence time scale ($\tau_\eta/\tau_{c_i} < 1$) means the mass distributions of that species are strongly affected by turbulence. In Figs. 3.12-3.13, it is shown that most of the flame radicals chemical life times are longer than the turbulence time scale, such as NO_2, HO_2, CH_2O. Figures 3.14-3.15 for the case 1 and Figures 3.16-3.17 for the case 2 show the distributions of mass fractions of each chemical species on a typical plane. The corresponding laminar profile is shown in the bottom of each image. As can be seen, the mass distributions of NO_2, NO, CH_2O for the both cases are strongly affected by turbulence and have relatively complicated distributions compared to its laminar flame, whereas CH, CH_2 and CN show relatively smooth distributions. It should be noted that several intermediate species show relatively smooth distributions although the $\tau_\eta/\tau_{c_i} < 1$, such as HCCOH and NCO in the case 1. Saito et al. [78] conducted two-dimensional (2D) DNS and showed that for almost all the species that are strongly affected by turbulence ($\tau_\eta/\tau_{c_i} < 1$), their distributions are much broadened and complicated compared to their laminar profiles. The difference between the results from Saito et al. [78] and present methane–air flames might be attributed to several reasons. Compared with the 2D DNS of Saito et al. [78],

an updated chemical mechanism, a lower Reynolds number and a more realistic three-dimensional turbulent field are considered in the present case.

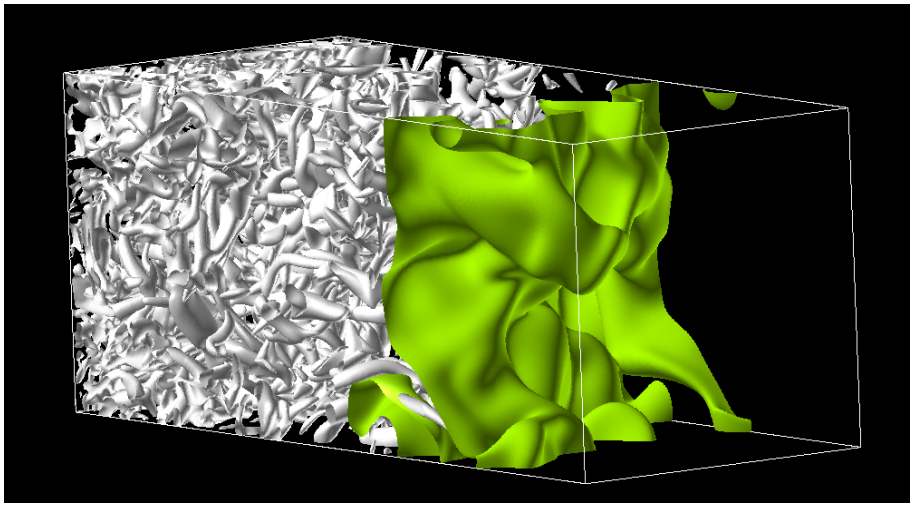

(a) Case 1 (T=1944 K)

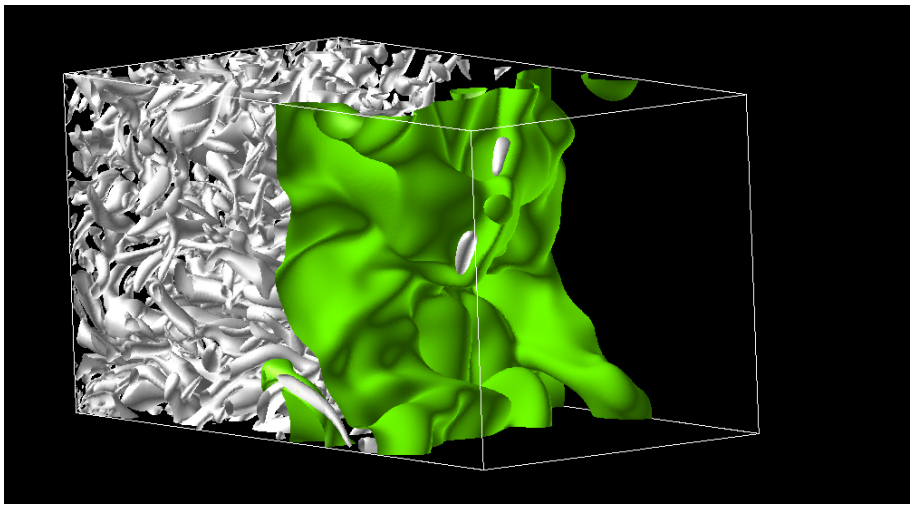

(b) Case 2 (T=1675 K)

Figure 3.5: Contour surfaces of temperature (T) and second invariant (Q^*) of the velocity gradient tensor (white) for case 1 (a) and case 2 (b). ($Q^* = 0.01$)

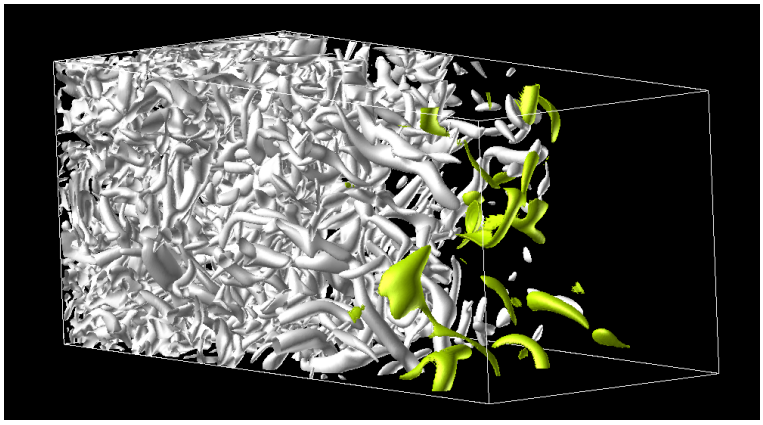

(a) $\Delta H/\Delta H_L$ = 1.0

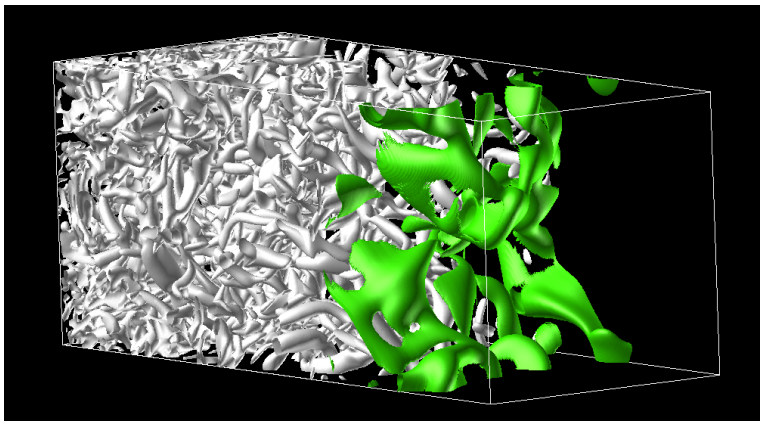

(b) $\Delta H/\Delta H_L$ = 0.8

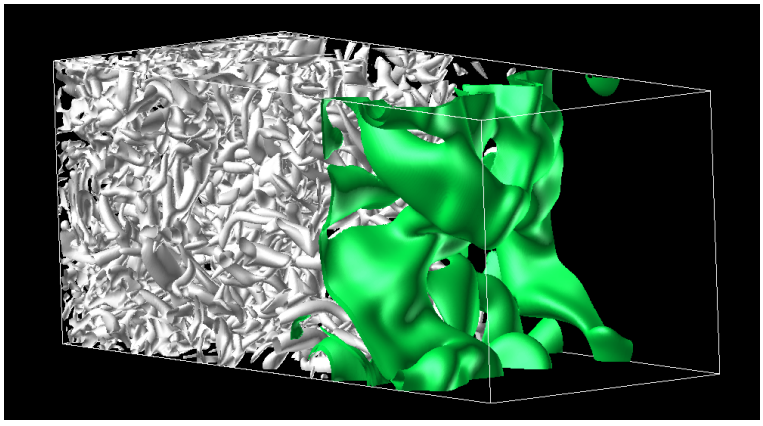

(c) $\Delta H/\Delta H_L$ = 0.6

Figure 3.6: Contour surfaces of heat release rate ($\Delta H/\Delta H_L$) and second invariant (Q^*) of the velocity gradient tensor (white) for case 1. ($Q^* = 0.01$)

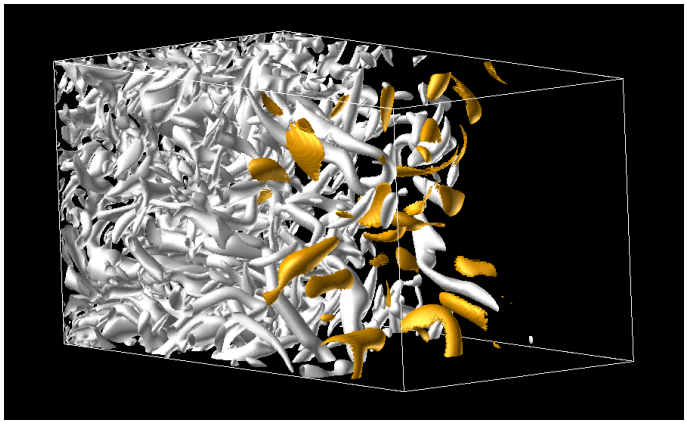

(a) $\Delta H/\Delta H_L$ = 1.0

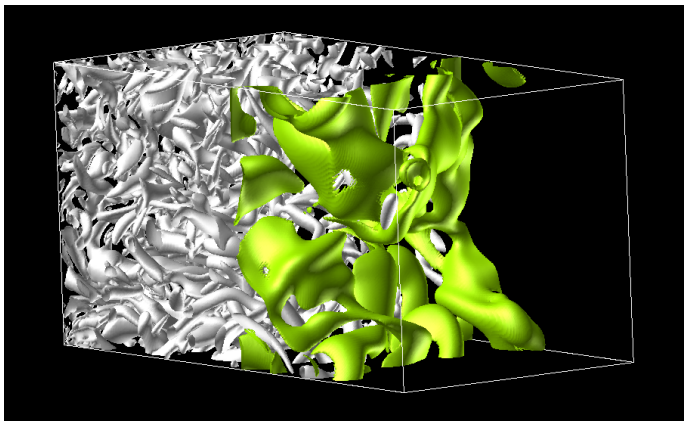

(b) $\Delta H/\Delta H_L$ = 0.8

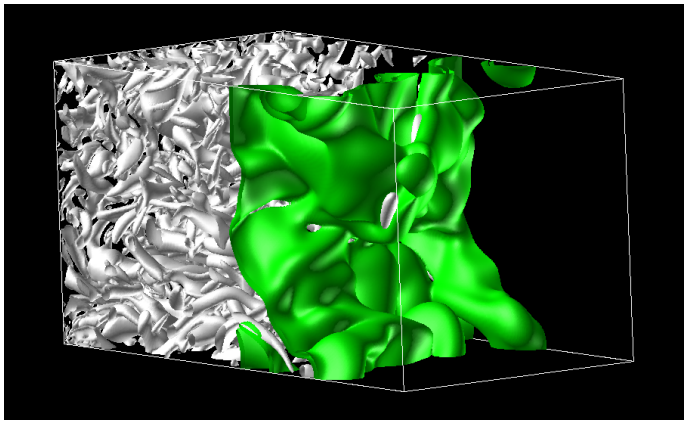

(c) $\Delta H/\Delta H_L$ = 0.6

Figure 3.7: Contour surfaces of heat release rate ($\Delta H/\Delta H_L$) and second invariant (Q^*) of the velocity gradient tensor (white) for case 2. ($Q^* = 0.01$)

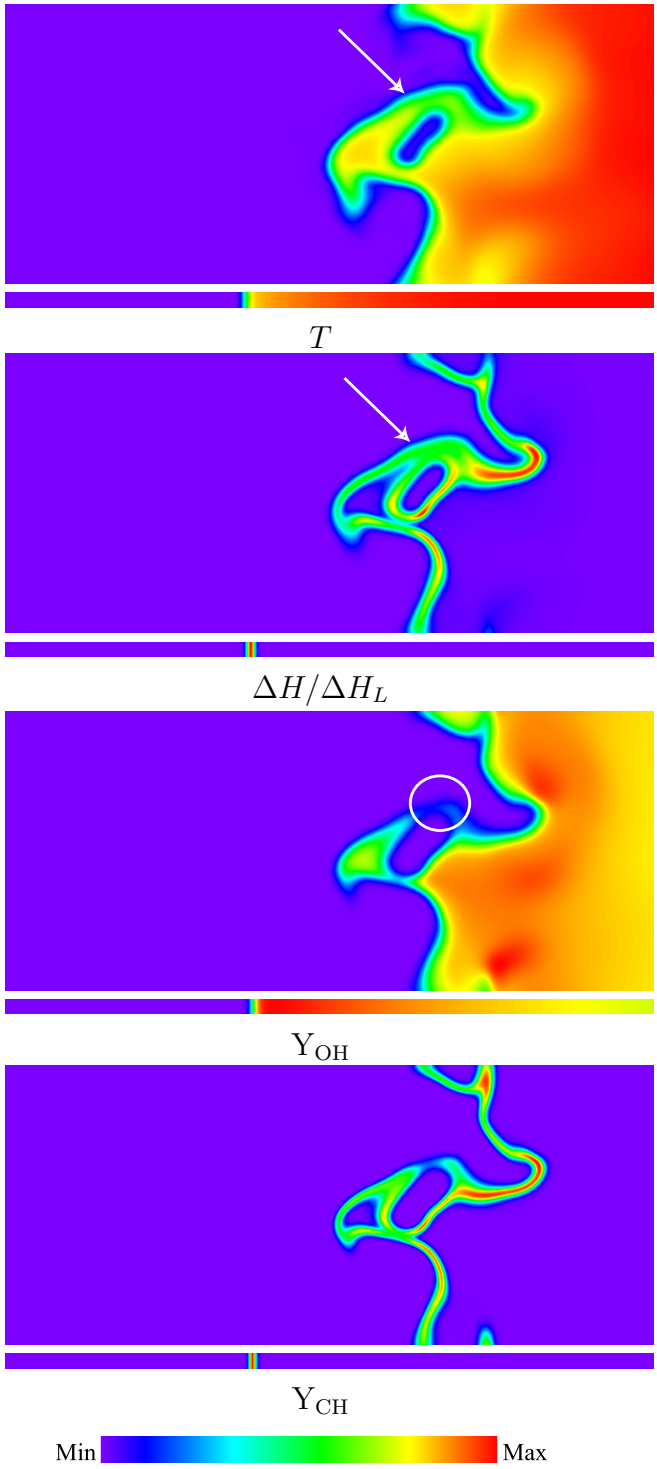

Figure 3.8: Distributions of Temperature (T), normalized heat release rate ($\Delta H/\Delta H_L$) and mass fractions of OH and CH on a typical plane for case 1.

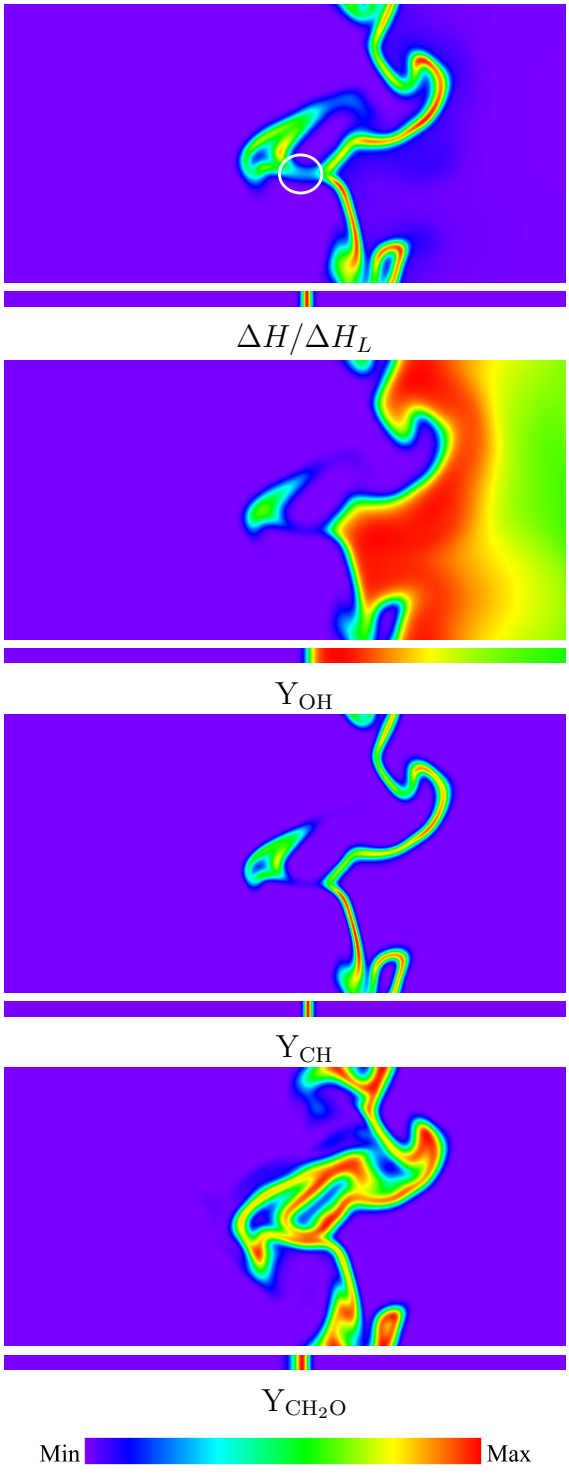

Figure 3.9: Distributions of normalized heat release rate ($\Delta H/\Delta H_L$) and mass fractions of OH, CH and CH_2O on a typical plane for case 2.

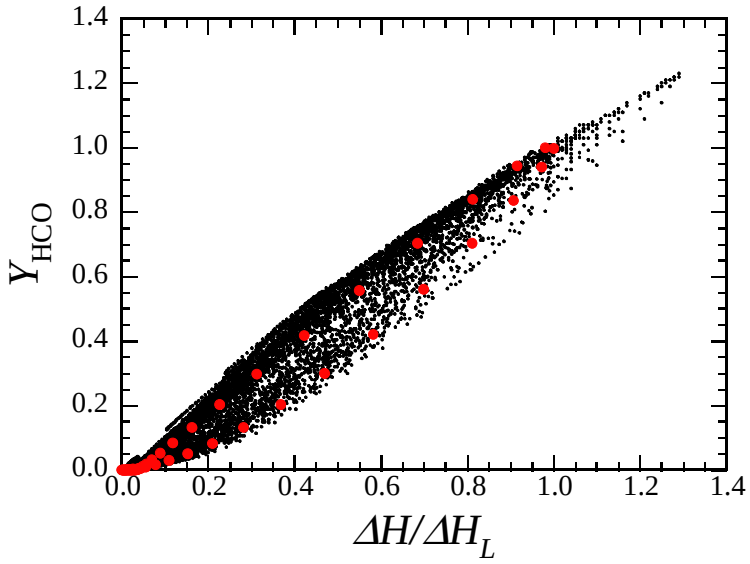

(a) Case 1

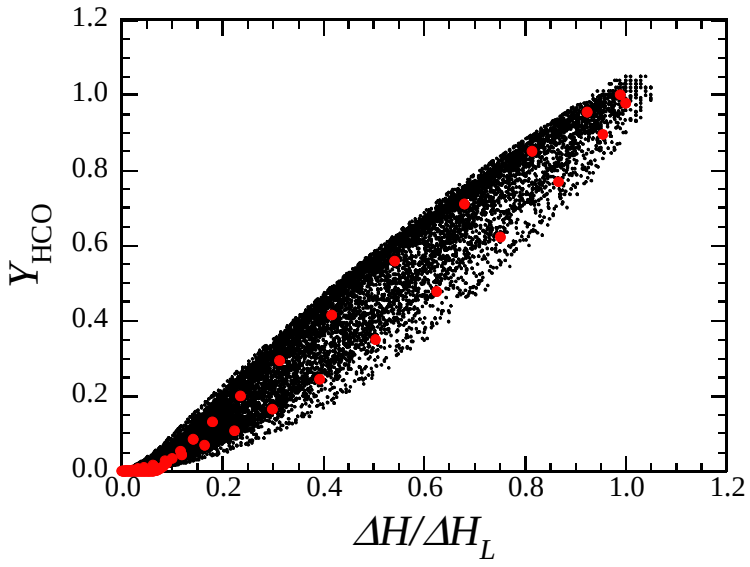

(b) Case 2

Figure 3.10: Scatter plots of mass fractions of HCO and local heat release rate. (Red symbols correspond to laminar flame.)

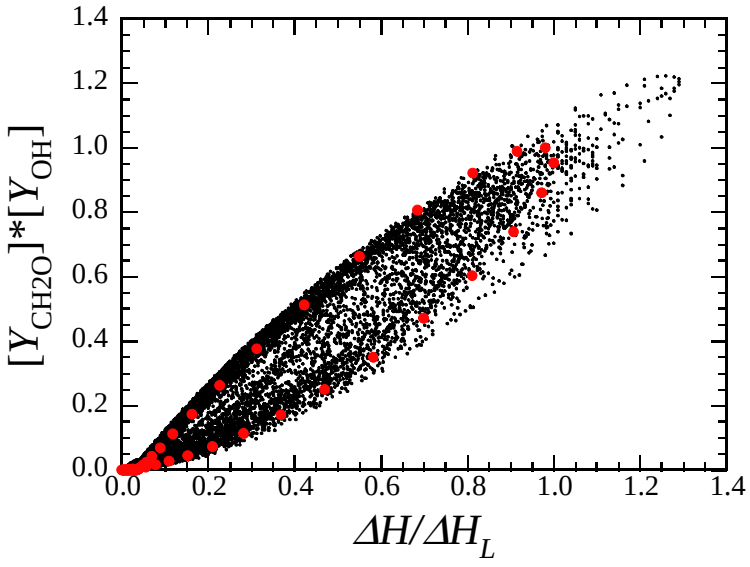

(a) Case 1

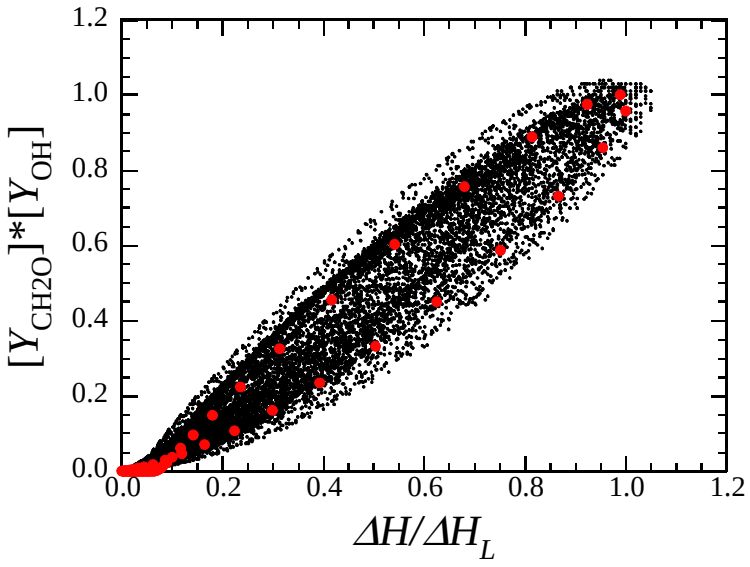

(b) Case 2

Figure 3.11: Scatter plots of mass fractions of CH_2O-OH and local heat release rate. (Red symbols correspond to laminar flame.)

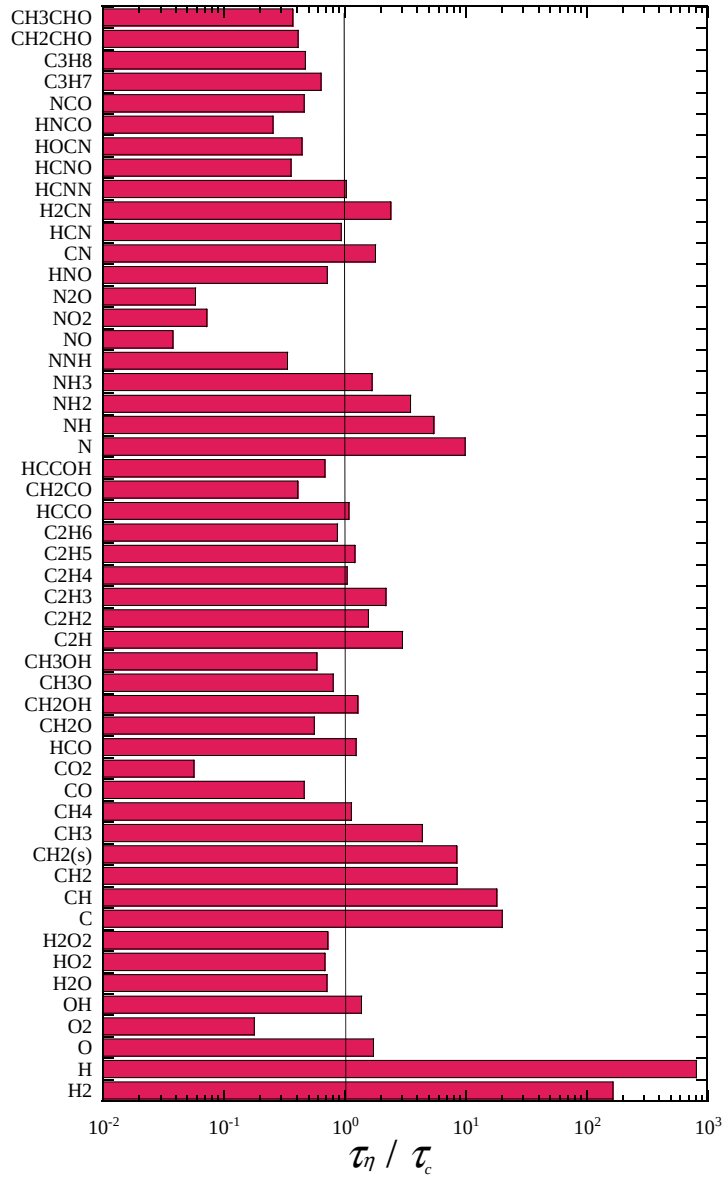

Figure 3.12: Ratios of turbulence time scale to chemical time scale in case 1.

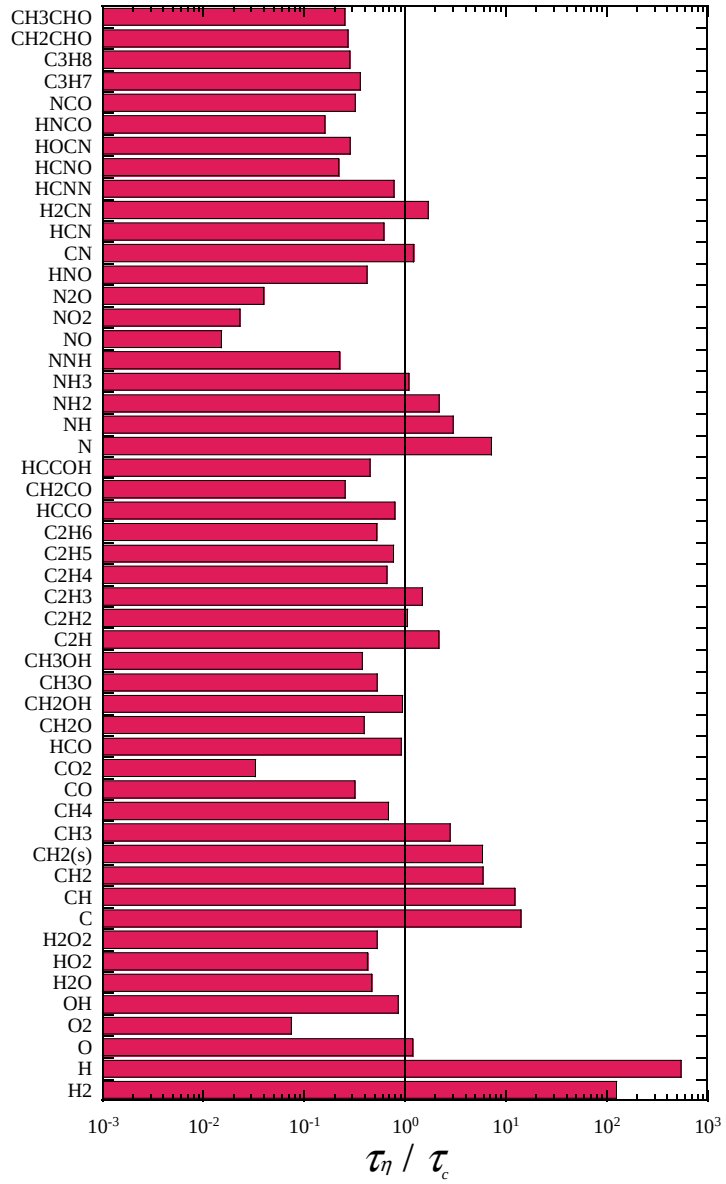

Figure 3.13: Ratios of turbulence time scale to chemical time scale in case 2.

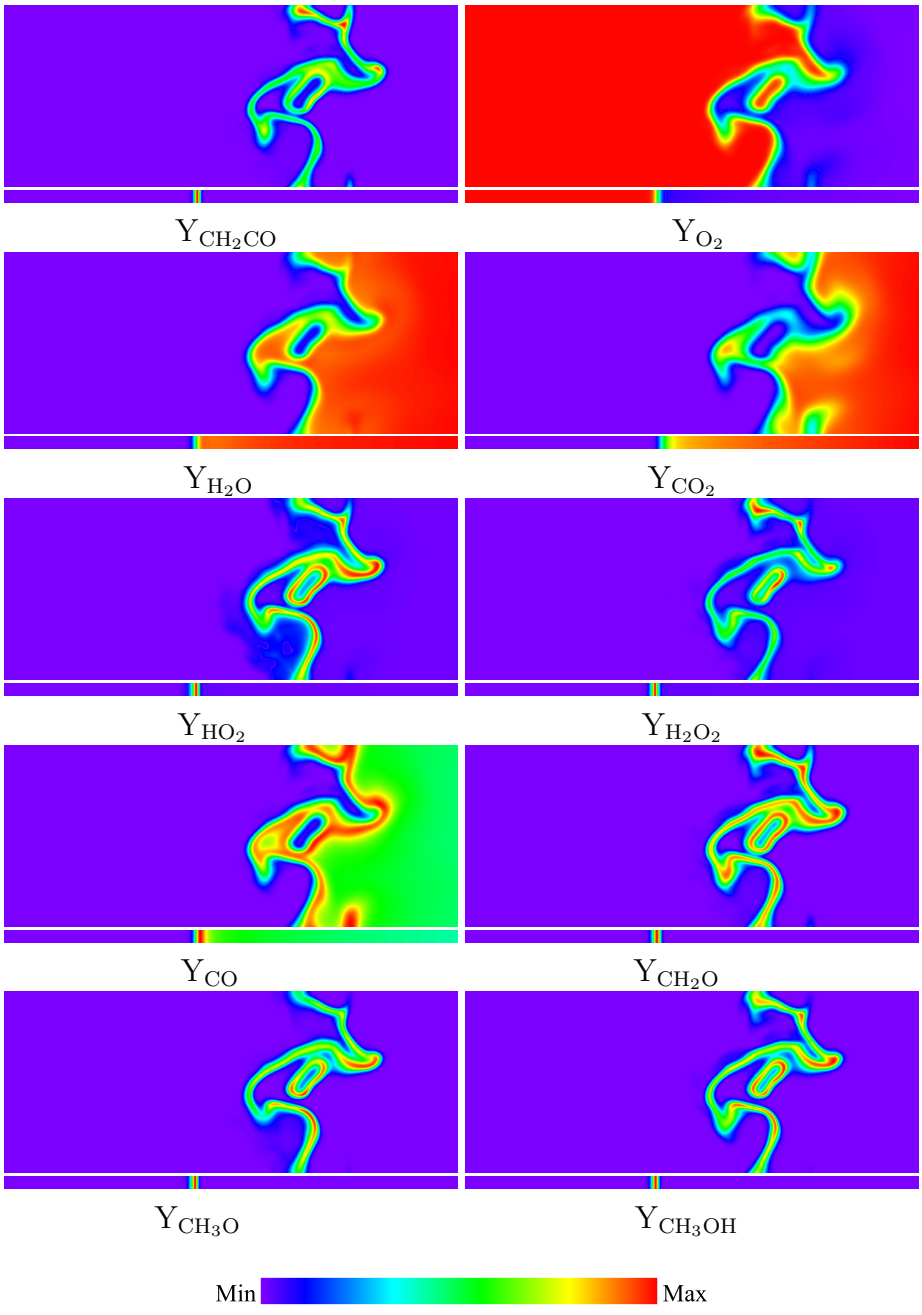

Figure 3.14: Mass fraction distributions of chemical species on a typical plane for case 1. Strong effect of turbulence to the mass distributions.

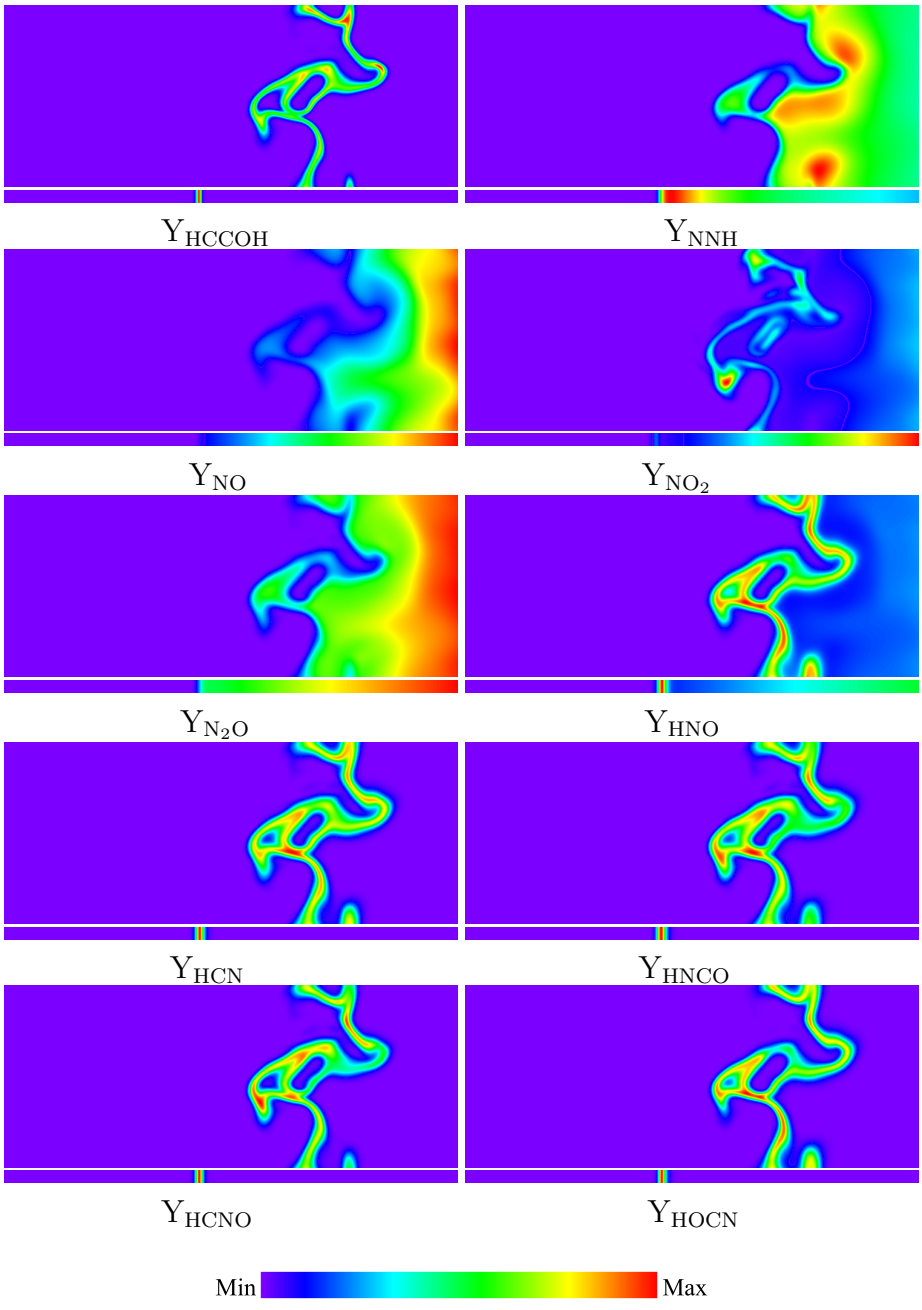

Figure 3.14: (continued) Mass fraction distributions of chemical species on a typical plane for case 1. Strong effect of turbulence to the mass distributions.

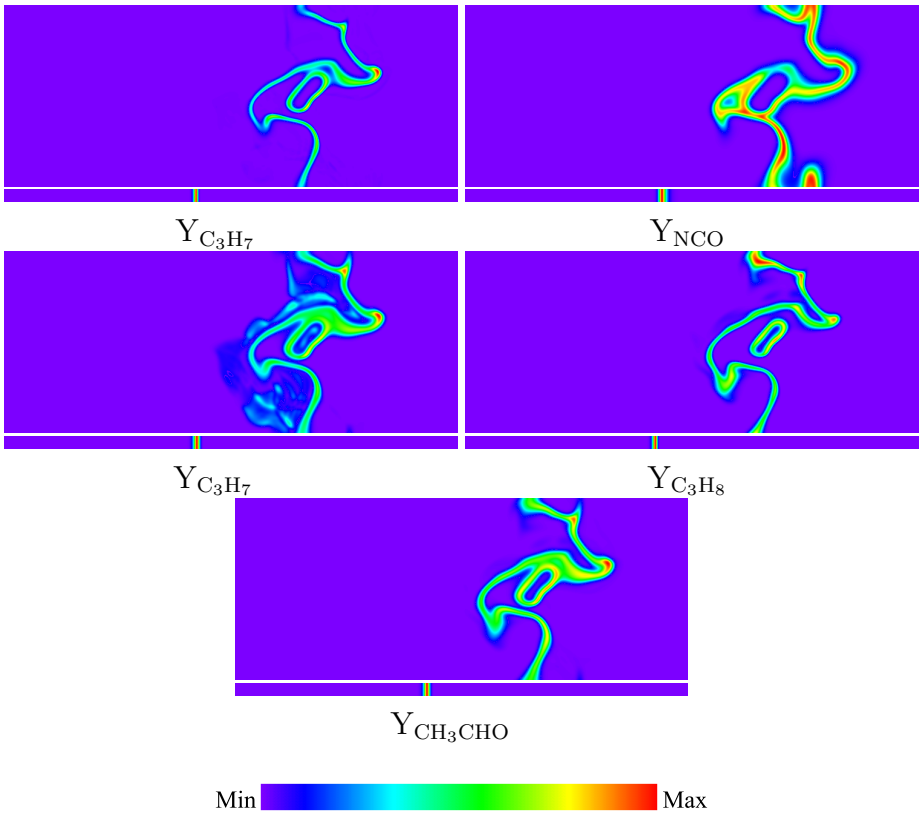

Figure 3.14: (continued) Mass fraction distributions of chemical species on a typical plane for case 1. Strong effect of turbulence to the mass distributions.

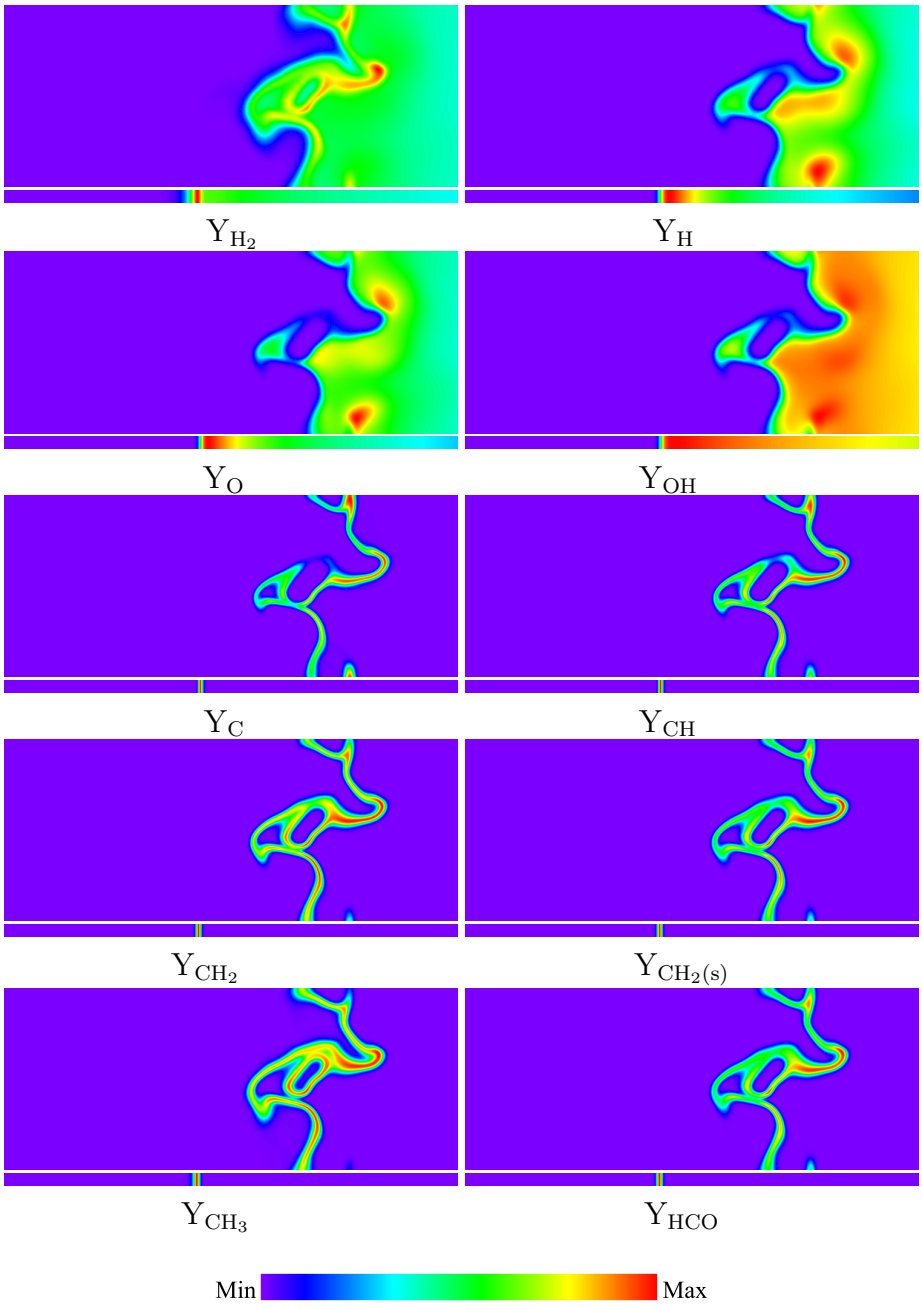

Figure 3.15: Mass fraction distributions of chemical species on a typical plane for case 1. Weak effect of turbulence to the mass distributions.

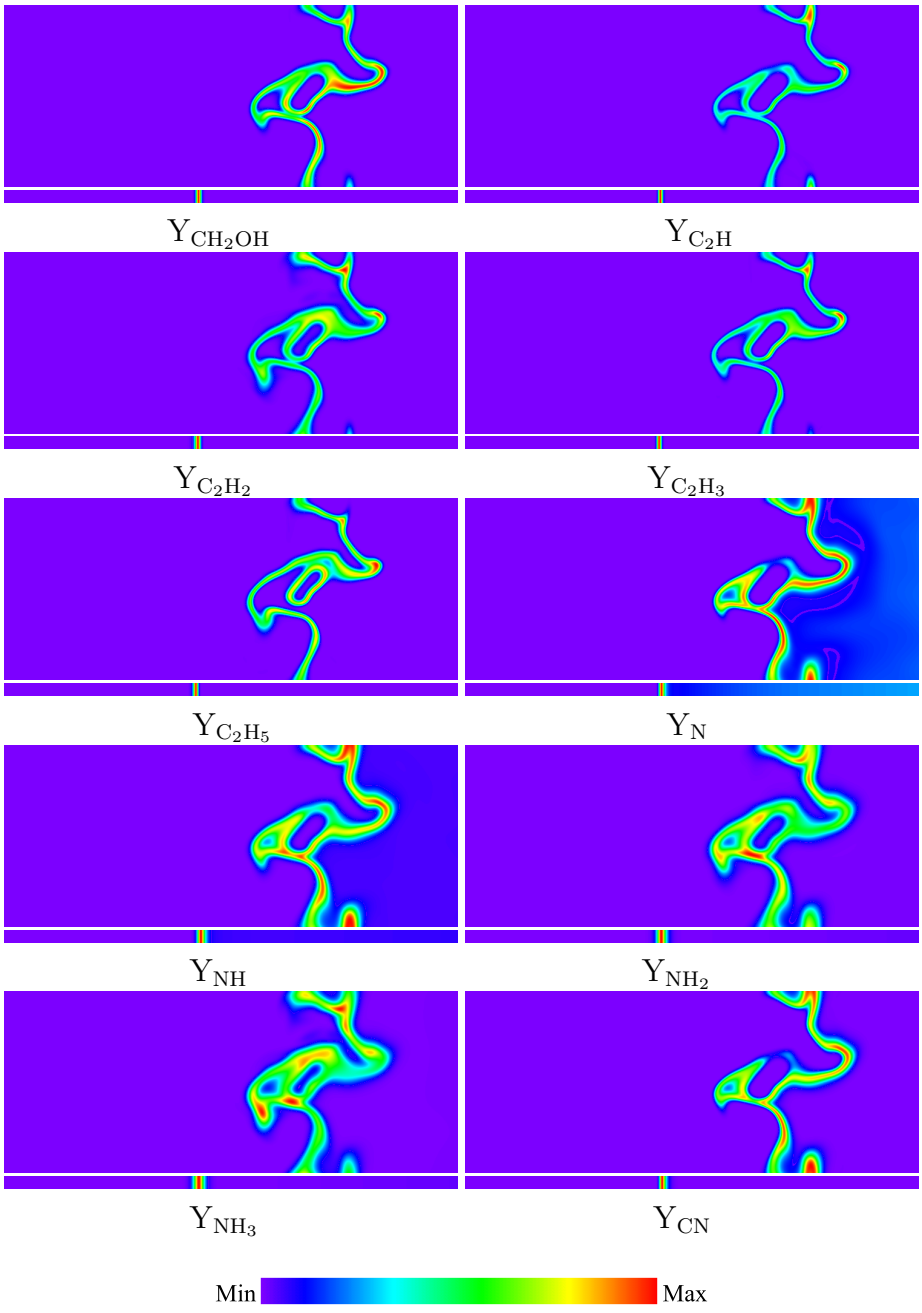

Figure 3.15: (continued) Mass fraction distributions of chemical species on a typical plane for case 1. Weak effect of turbulence to the mass distributions.

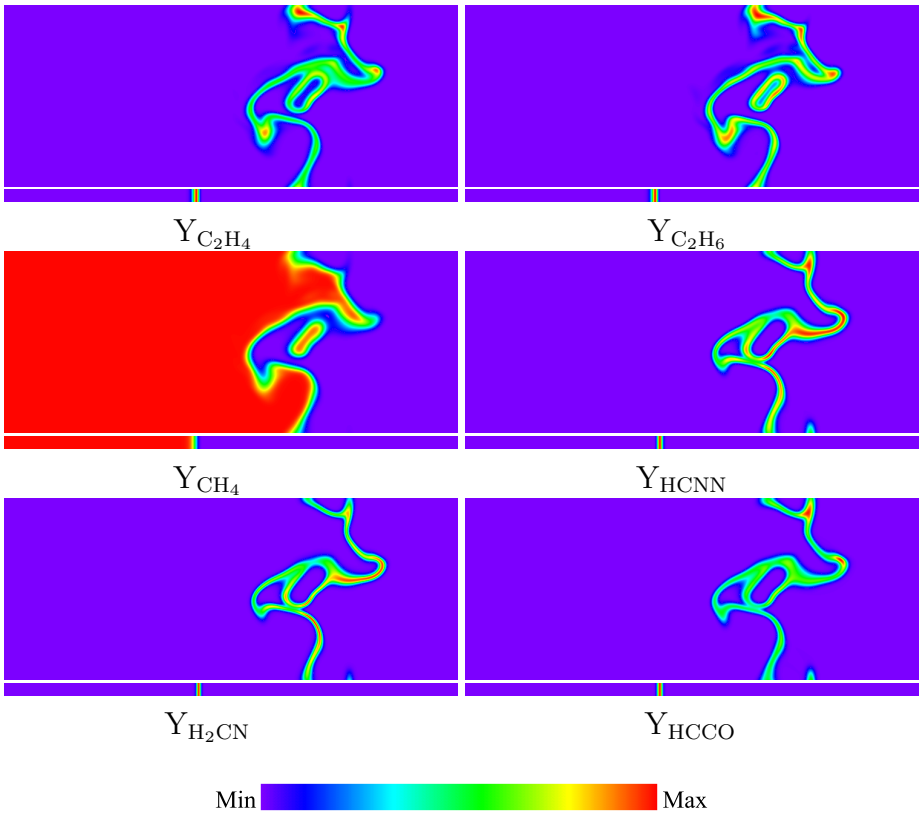

Figure 3.15: (continued) Mass fraction distributions of chemical species on a typical plane for case 1. Weak effect of turbulence to the mass distributions.

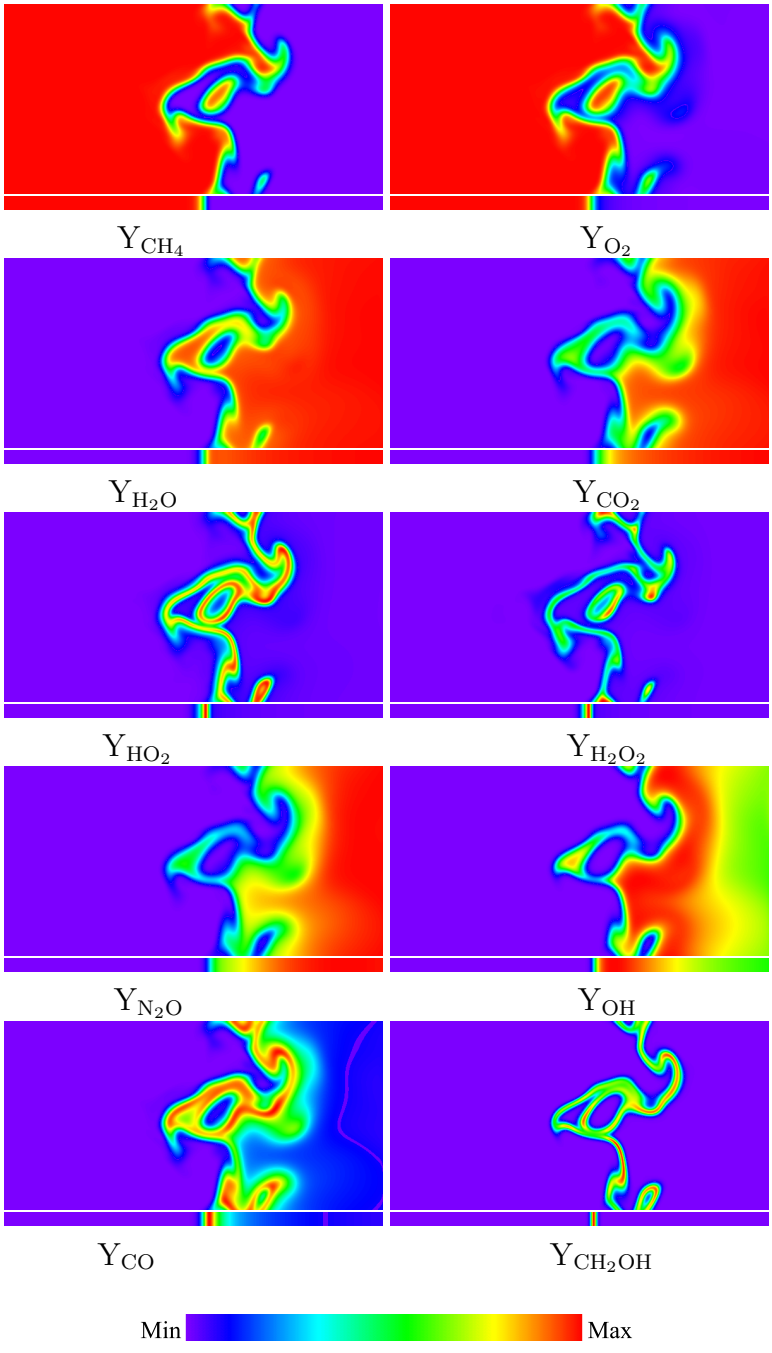

Figure 3.16: Mass fraction distributions of chemical species on a typical plane for case 2. Strong effect of turbulence to the mass distributions.

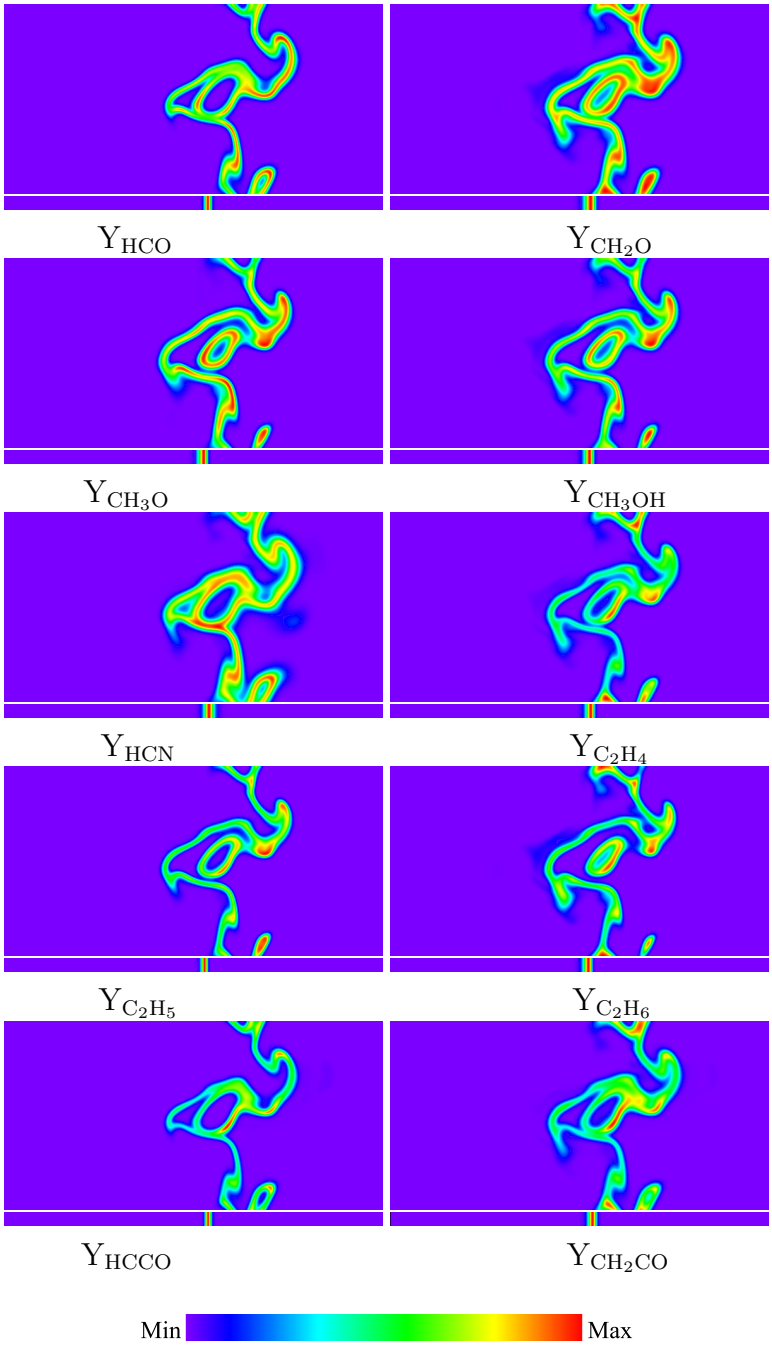

Figure 3.16: (continued) Mass fraction distributions of chemical species on a typical plane for case 2. Strong effect of turbulence to the mass distributions.

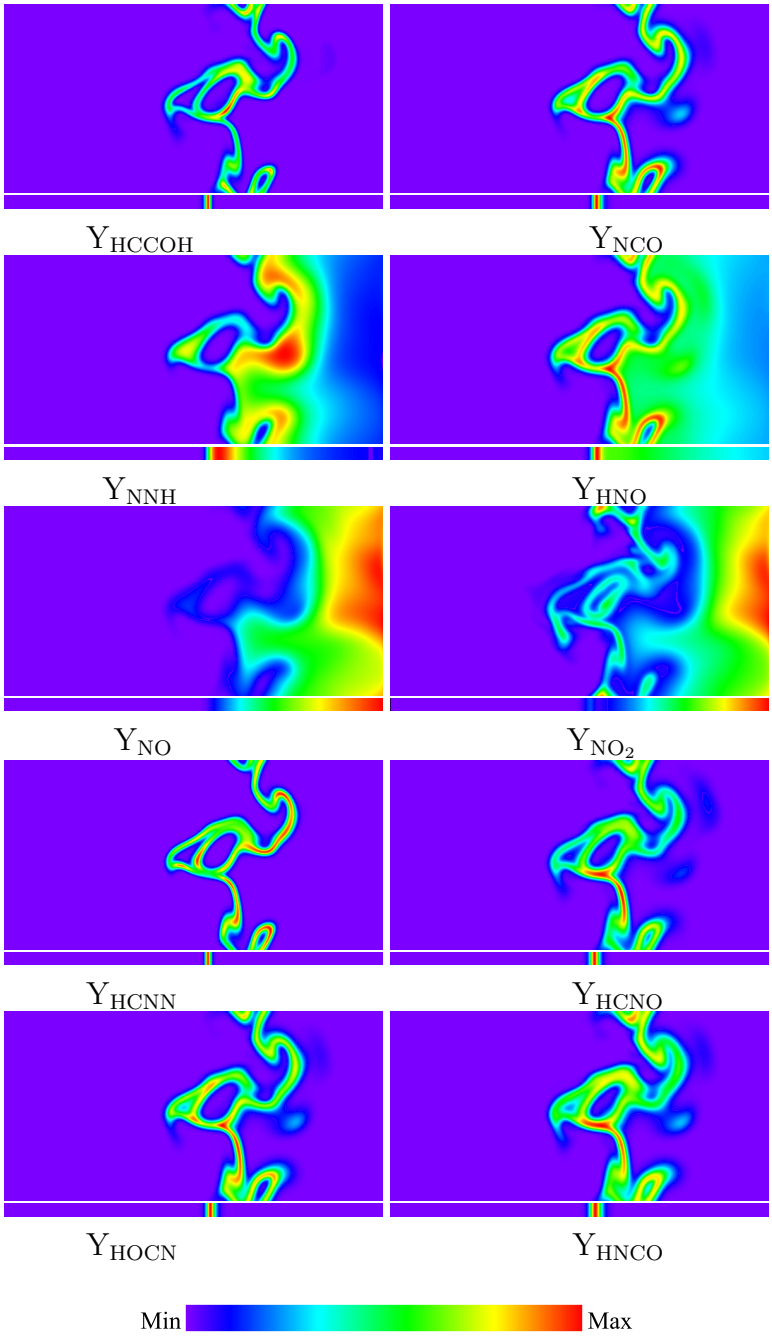

Figure 3.16: (continued) Mass fraction distributions of chemical species on a typical plane for case 2. Strong effect of turbulence to the mass distributions.

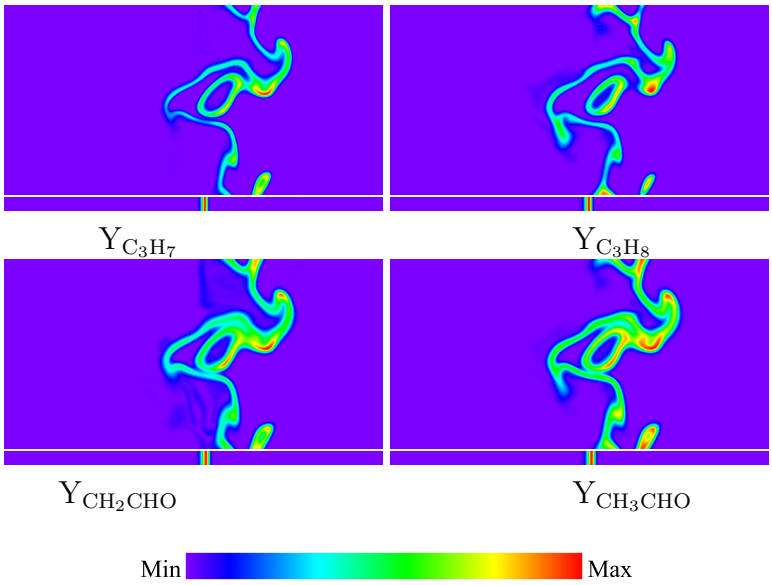

Figure 3.16: (continued) Mass fraction distributions of chemical species on a typical plane for case 2. Strong effect of turbulence to the mass distributions.

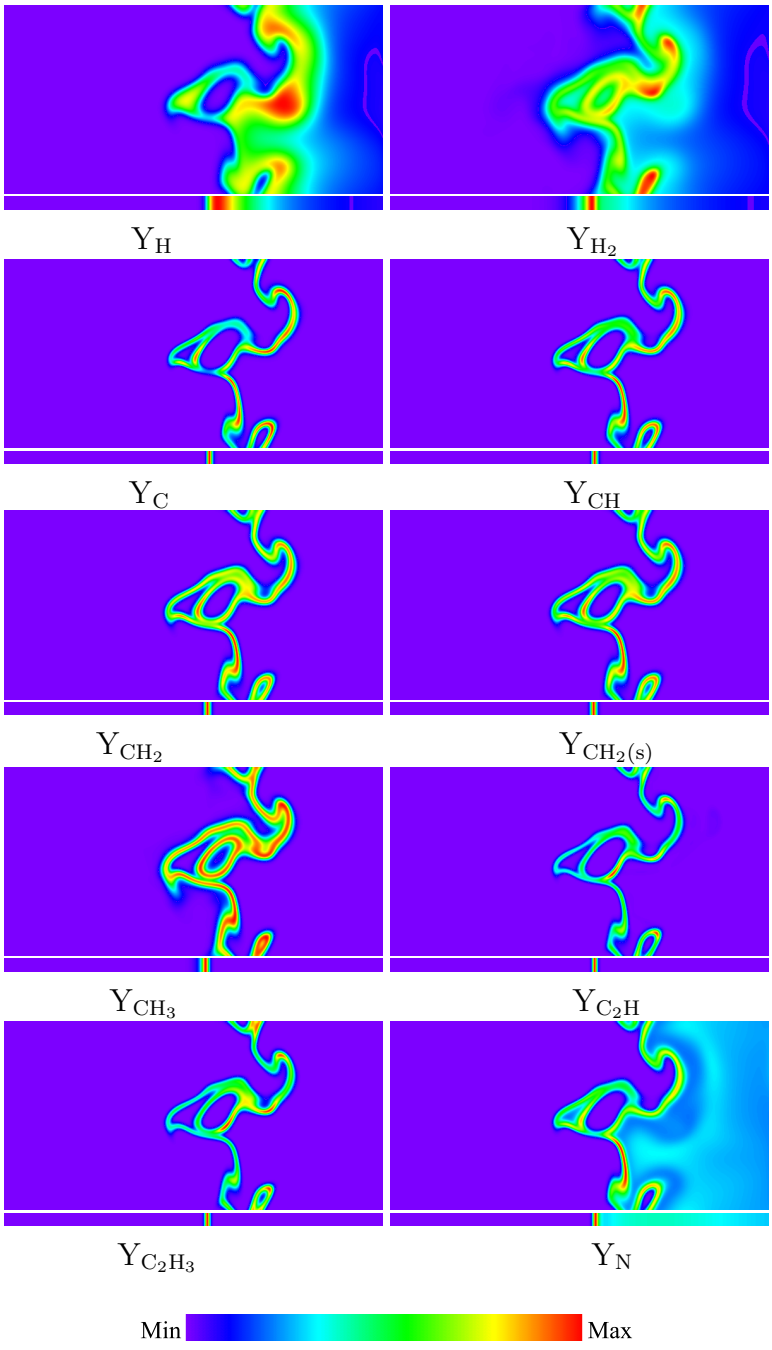

Figure 3.17: Mass fraction distributions of chemical species on a typical plane for case 2. Weak effect of turbulence to the mass distributions.

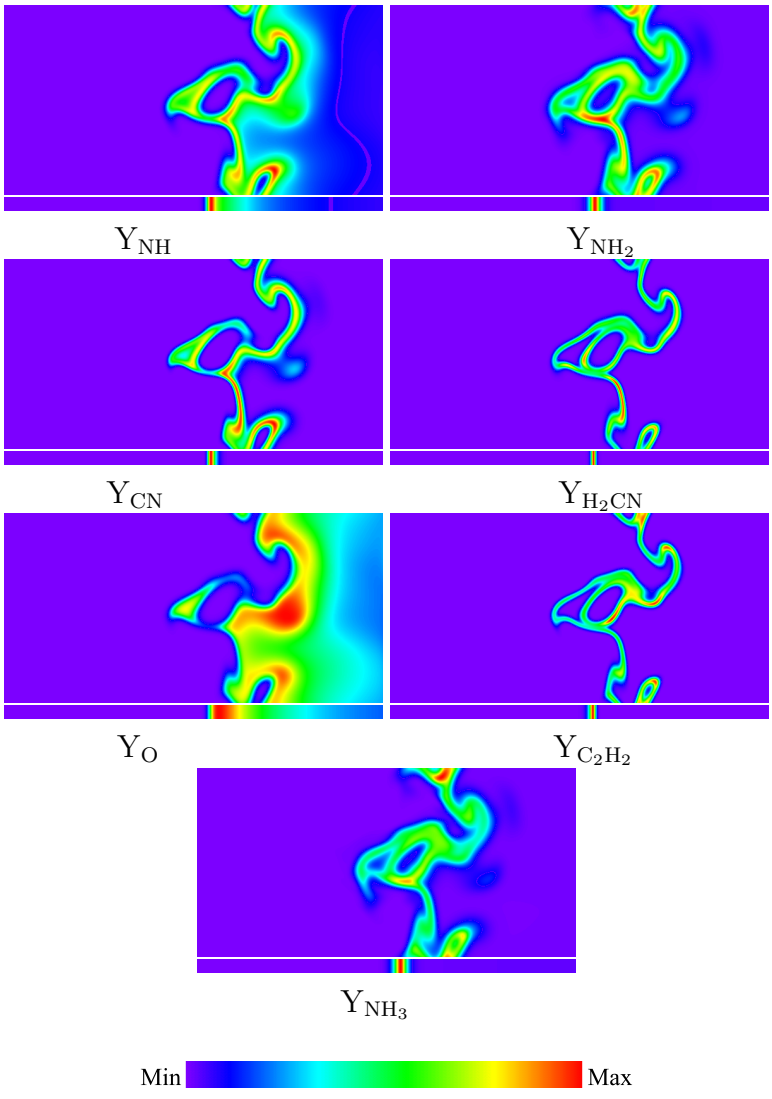

Figure 3.17: (continued) Mass fraction distributions of chemical species on a typical plane for case 2. Weak effect of turbulence to the mass distributions.

3.4 Statistical characteristics of local flame structures

In this section, the statistical characteristics of flame elements are investigated to understand the effects of turbulence on local flame structures in the thin reaction zones. The two cases are compared with hydrogen–air flame from the previous DNS study by Shim et al. [54]. In the turbulent combustion diagram proposed by Peters [10], as shown in Fig. 3.18, all three cases are located in the thin reaction zones regime, and the locations of H_2–air flame and the stoichiometric CH_4–air flame are almost identical. The initial numerical parameters for these flames can be found in Table 3.2. Although the normalized turbulent intensity (u'_{rms}/S_L) is the lowest in hydrogen–air flame, u'_{rms} is around 3 times larger than that in both methane cases, as the laminar burning velocity of H_2–air flame is much faster (S_L = 10.3 m/s).

3.4.1 Effects of turbulence on local flame thickness and local mean curvature

It should be noted that the flame front is defined as surfaces with local maximum temperature gradient, as in section 2.5. Figure 3.19 shows the pdfs of the local heat release rate on the flame front. The local heat release rate of all cases are normalized by the maximum heat release rate of their corresponding laminar flame. The most expected heat release rate in the both methane flames are lower than their corresponding laminar flame, as the peaks of the pdf shows value around $0.90\Delta H_L$ and $0.95\Delta H_L$ for the case 1 and the case 2, respectively. For H_2–air flame, however, the most expected heat release rates are in the range from 1.0 to 1.1 times that of laminar flame. The maximum heat release rate reaches up to $1.4\Delta H_L$ and $1.2\Delta H_L$ for the case 1 and the case 2, respectively, while the maximum local heat release rate shows values around $1.3\Delta H_L$ in the hydrogen case.

Figure 3.20 shows the pdfs of the local flame thickness (δ) for all cases, and the local flame thickness are normalized by their corresponding laminar flame thickness δ_L. The definition of δ can be found in section 2.5. It can be clearly

seen that, although very thick flames can be found locally, the most expected local flame thickness for all cases are thinner than their corresponding laminar flame. On average, however, the mean flame thickness, δ_m, increases 10% that of laminar flame in the case 1. For the lean methane flame, the case 2, δ_m decreases 3% that of laminar flame. Sankaran et al. [51] have conducted three-dimensional DNS of lean methane–air Bunsen flame (ϕ = 0.7), which is classified into the thin reaction zones. They have found a thickening flame on average. Thinner flames results, however, were obtained for lean methane–air premixed flames from several experimental studies [79–81]. Recently, Tamadonfar and Gülder [82] have conducted experiment on premixed turbulent CH_4–air flames in the thin reaction zones, they have shown that the preheat zone and the reaction zone thicknesses are thinner than the corresponding laminar flame for equivalence ratios ranging from 0.6 to 0.7, and thicker than the corresponding laminar flame for equivalence ratios ranging from 0.8 to 1.0. However, they have discussed that the creation of the thicker flame front is not due to the turbulence but may be due to the overestimation of flame front thickness when using 2D image processing [83]. In Fig. 3.20, for hydrogen case, the mean flame thickness decreases about 26% that of laminar flame.

The pdfs of the local mean curvature (k) on the flame front are shown in Fig. 3.21. k is normalized by the corresponding η in the unburned side. The flame elements convex toward the unburned side have negative values. The most expected k shows 0 for all cases, and the probability of positive curvature is relatively higher. This result is more pronounced in the methane cases than that in the hydrogen case. For all cases, the minimum curvature radius of the flame front is about twice of the Kolmogorov length scale.

Figure 3.22 demonstrates the pdfs of tangential strain rate (a_t) which is normalized by u'_{rms}/λ in the unburned side. The positive and the negative strains represent stretch and compression, respectively. It can be seen that, all pdfs skew to the positive side and the mean a_t is positive for all cases. This means that for methane flames and hydrogen flame, most of the flame elements tend to be

stretched in the tangential direction.

It is known that stretched flames tend to get thinner, therefore the relationship between local flame thickness, tangential strain rate and local mean curvature is studied next. Figure 3.23 shows the joint probability density function (jpdf) of tangential strain rate and local flame thickness for the case 1. The jpdf of mean curvature and local flame thickness for the case 1 is shown in Fig. 3.24. These two jpdfs are also drawn for the case 2 and the hydrogen flame in Figs. 3.25-3.26 and Figs. 3.27-3.28, respectively. As expected, for all cases, flame tends to get thinner at high positive strain region, as can be seen in Figs. 3.23, 3.25 and 3.27. It can be observed that this tendency is the strongest in the case of hydrogen flame, and the most of the flame elements thinner than the corresponding laminar flame ($\delta/\delta_L <$ 1.0) are in the positive strain region. In the cases of methane flames, it can be seen that the probability of thicker flame elements ($\delta/\delta_L > 1.0$) in the positive strain region is substantially higher than that in hydrogen flame. This result reveals that why the present methane flames thickness do not decrease as much, on average, as in hydrogen flames. The flame thickening on average in the case 1 could be attributed to the stretch effects.

In Figs. 3.24 and 3.26, for the both methane cases, an asymmetrical dependence of flame elements on the flame front curvature can be observed. The majority of the thin flames ($\delta/\delta_L < 1.0$) are found in the positive curvature region. The thinnest flame can be found between 0-2/δ_L curvature region. Similar tendency has been reported in the previous three-dimensional DNS study of lean CH_4–air Bunsen flame [51]. A recent experimental study [82] on methane–air Bunsen flame in the thin reaction zones has shown that the amount of flame front thickening however, is equally distributed in the positive and the negative curvature regions while the thinnest flame is found to be located in the zero curvature region. In hydrogen case, as shown in Fig. 3.28, similar tendency can be seen compared to the methane cases. However, the probability of flame elements thinner than the corresponding laminar flame in the negative curvature region is relatively higher compared with those in the cases of methane flames. The asymmetrical

dependence of flame elements to the flame front is also much less pronounced.

Table 3.2: Numerical parameters for DNS of turbulent premixed flames.

	ϕ	T_{ini} [K]	Re_λ	Re_l	u'_{rms}/S_L	l/δ_F	D/δ_F	η [mm]
Case 1	1.0	950	37.4	144	7.14	20.1	4.64	0.0189
Case 2	0.6	950	37.4	144	9.78	14.7	3.39	0.0189
H_2–air flame [54]	1.0	700	37.4	144	6.81	21.1	4.85	0.0054

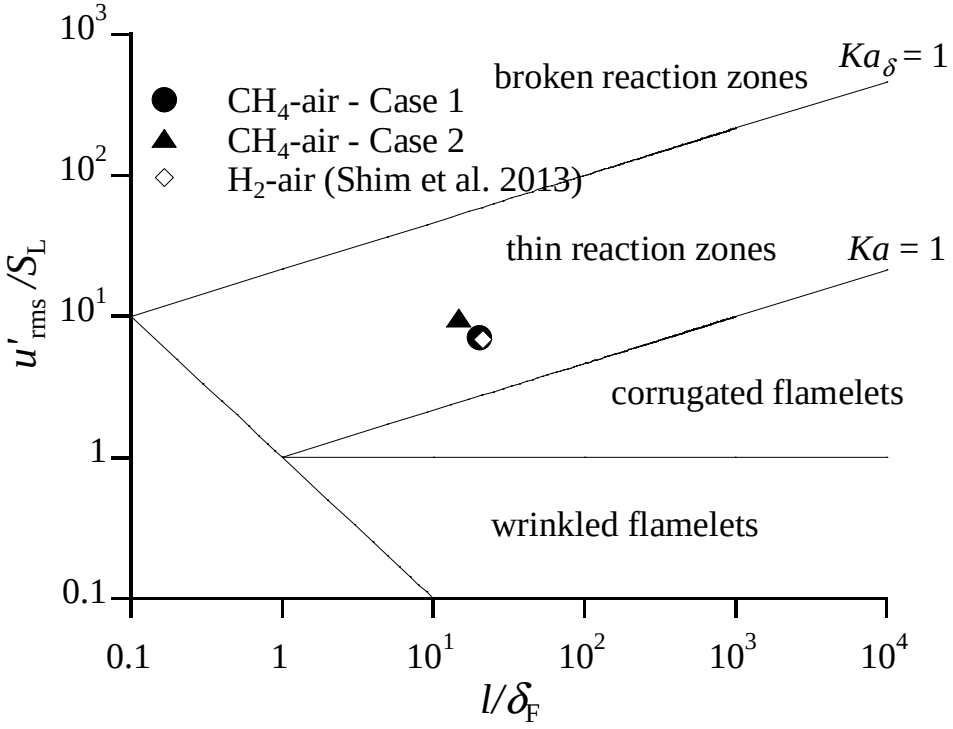

Figure 3.18: Turbulent combustion diagram. H_2–air planar premixed flame is from the previous DNS study by Shim et al. [54].

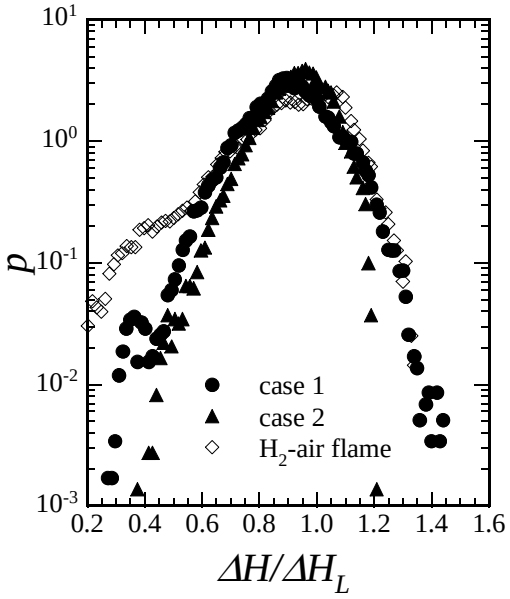

Figure 3.19: Probability density functions of the local heat release rate on the flame front.

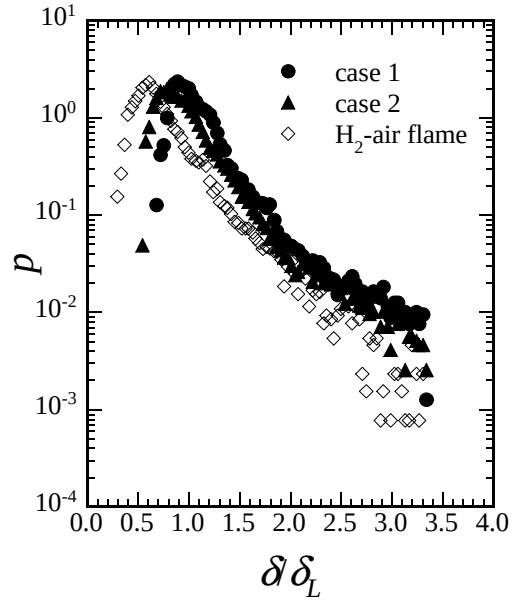

Figure 3.20: Probability density functions of the local flame thickness.

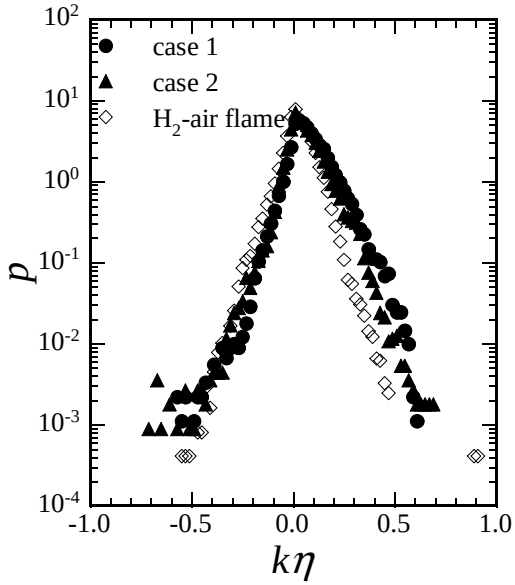

Figure 3.21: Probability density functions of the local mean curvature on the flame front.

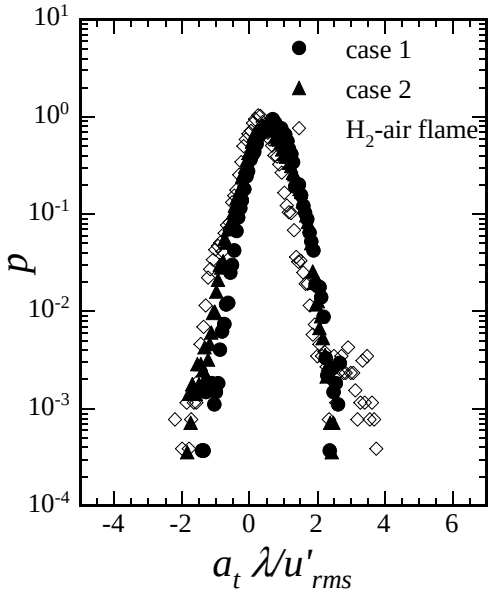

Figure 3.22: Probability density functions of the tangetial strain rate.

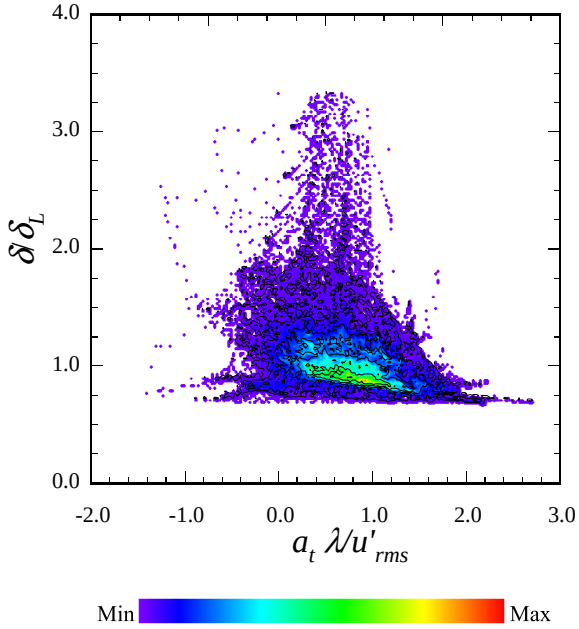

Figure 3.23: Joint probability density function of tangential strain rate and local flame thickness for case 1.

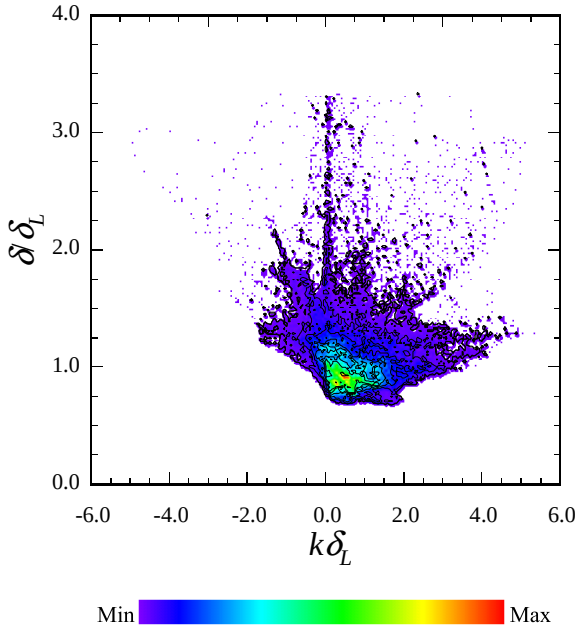

Figure 3.24: Joint probability density function of mean curvature and local flame thickness for case 1.

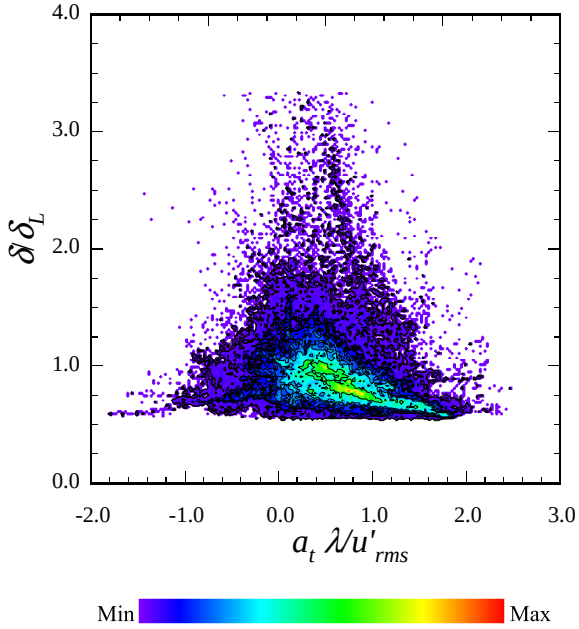

Figure 3.25: Joint probability density function of tangential strain rate and local flame thickness for case 2.

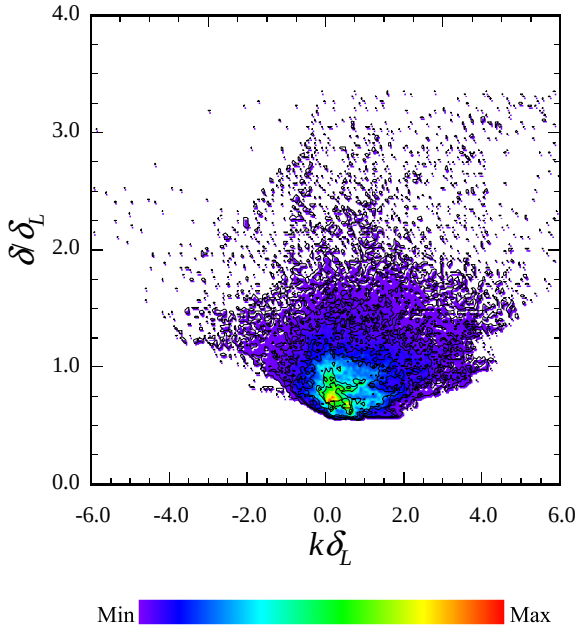

Figure 3.26: Joint probability density function of mean curvature and local flame thickness for case 2.

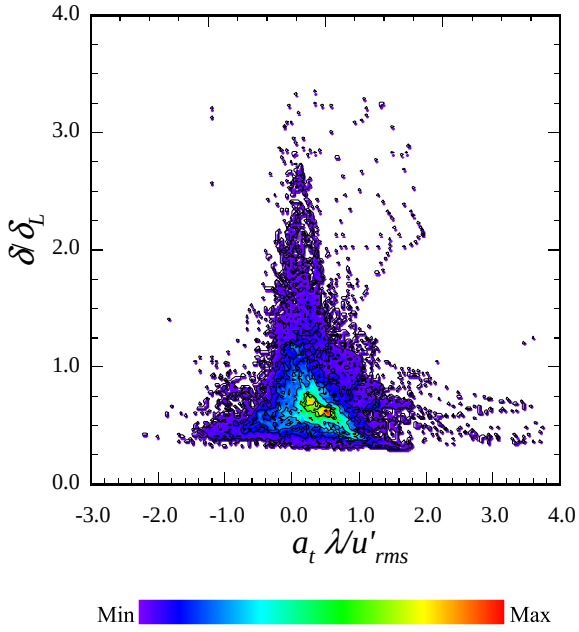

Figure 3.27: Joint probability density function of tangential strain rate and local flame thickness for H_2–air flame.

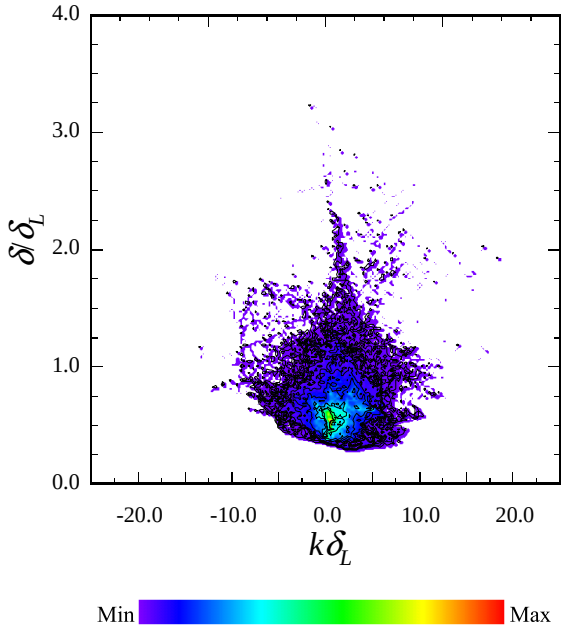

Figure 3.28: Joint probability density function of mean curvature and local flame thickness for H_2–air flame.

3.4.2 Effects of turbulence to the reaction and preheat zones

The effects of turbulence are investigated to clarify whether there is a significant disturbance on the reaction zones layer. Positive means production and negative means consumption. Figure 3.29 shows the conditional means of reaction rates (ω) of CH_4 and O_2 on the progress variable (c). Here, c is based on temperature and defined as follows:

$$c = \frac{T - T_u}{T_b - T_u} \tag{3.8}$$

Other key species' reaction rates in the reaction zones; CH, CO and OH are shown in Fig. 3.30 for the case 1. Reaction rates of the same chemical species for the case 2 are shown in Fig. 3.32 and 3.33. The reaction rates are normalized by the maximum reaction rate in their corresponding laminar flame, and their laminar reaction rates are also plotted. It can be clearly seen that the reaction rates of these species have similar profiles to that of laminar flames. However, the mean reaction rate values of the case 1 and the case 2 decreases around 20% and 15% that of laminar flame, respectively.

To investigate the reaction rate profiles of species that are formed in front of the flame front, the conditional means of reaction rates of species C_2H_4, C_2H_6, CH_2O and HO_2 are plotted along with their laminar flame values in Fig. 3.31 and 3.34 for the case 1 and the case 2, respectively. Similar reaction rate profiles to that of laminar flames can be observed while their mean values decrease. It can be seen that the reaction rate profiles in the reaction zone and preheat zone skew to the higher temperature region due to turbulence. These result show that, for the conditions considered in the present methane–air flames, turbulence significantly affect the reaction layers although the reaction rates have similar profiles compared with those in the laminar flame.

Figure 3.35 shows the conditional means of reaction rates of H_2 and HO_2 for hydrogen case. In the reaction zone, it can be seen that the profile of H_2 is close to its laminar flame. In the preheat zone, in Fig. 3.35 (b), the reaction rates of HO_2 is disturbed significantly. The region represented by solid box in Fig. 3.35 (b) is

magnified and drawn in Fig. 3.36.

Although the locations of these three flames in the turbulent combustion diagram are very close to each other, it has been revealed that the effects of turbulence to the preheat zones is much stronger in H_2–air flame. This might be attributed to a much smaller Kolmogorov length scale and higher turbulent intensity in H_2–air flame, which is shown in Table 3.2.

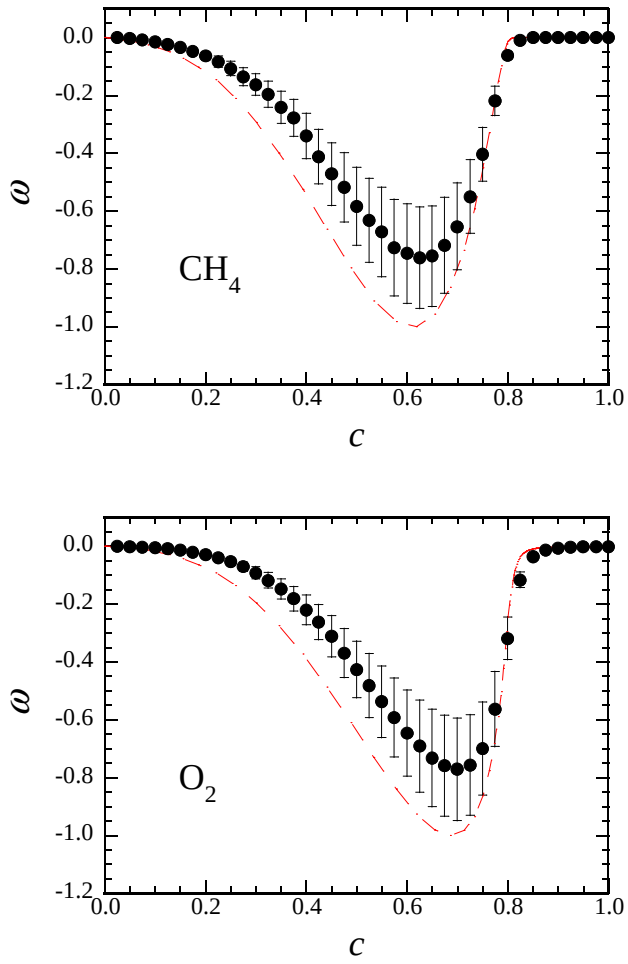

Figure 3.29: Normalized conditional means of reaction rates on the progress variable (c) for case 1 in reaction zone. (Red dashed line correspond to laminar flame. Full black symbols represent the conditional means of reaction rates for turbulent flame. Error bars represent the standard deviation of each reaction rate.)

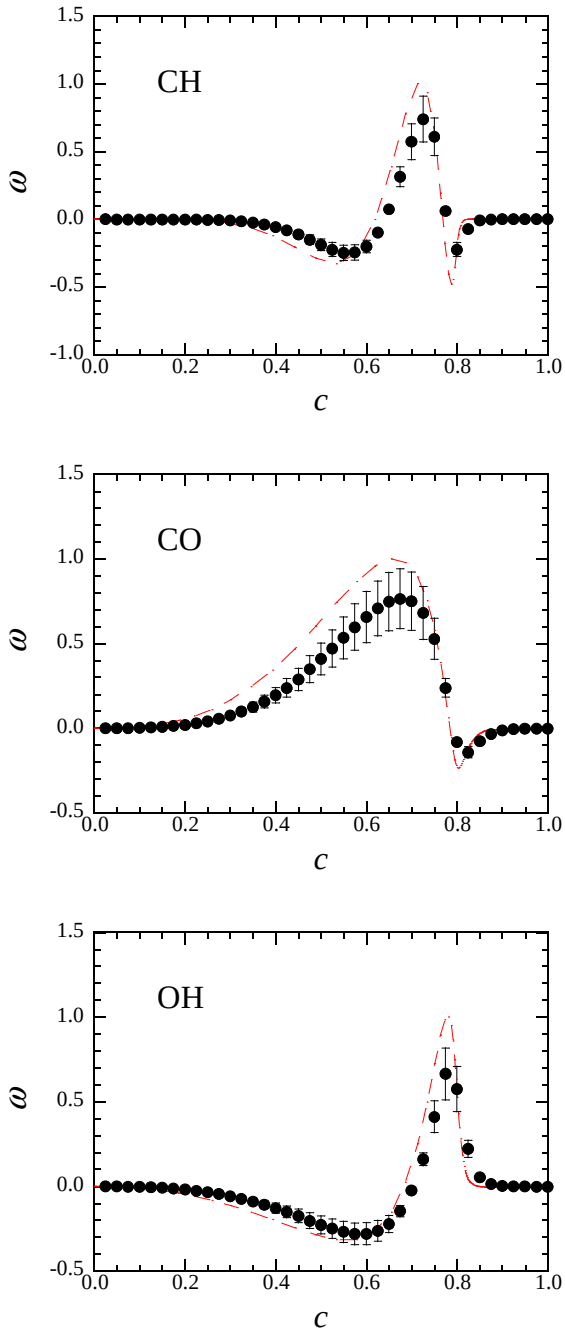

Figure 3.30: Normalized conditional means of reaction rates of the key species on the progress variable (c) for case 1. (Red dashed line correspond to laminar flame. Full black symbols represent the conditional means of reaction rates for turbulent flame. Error bars represent the standard deviation of each reaction rate.)

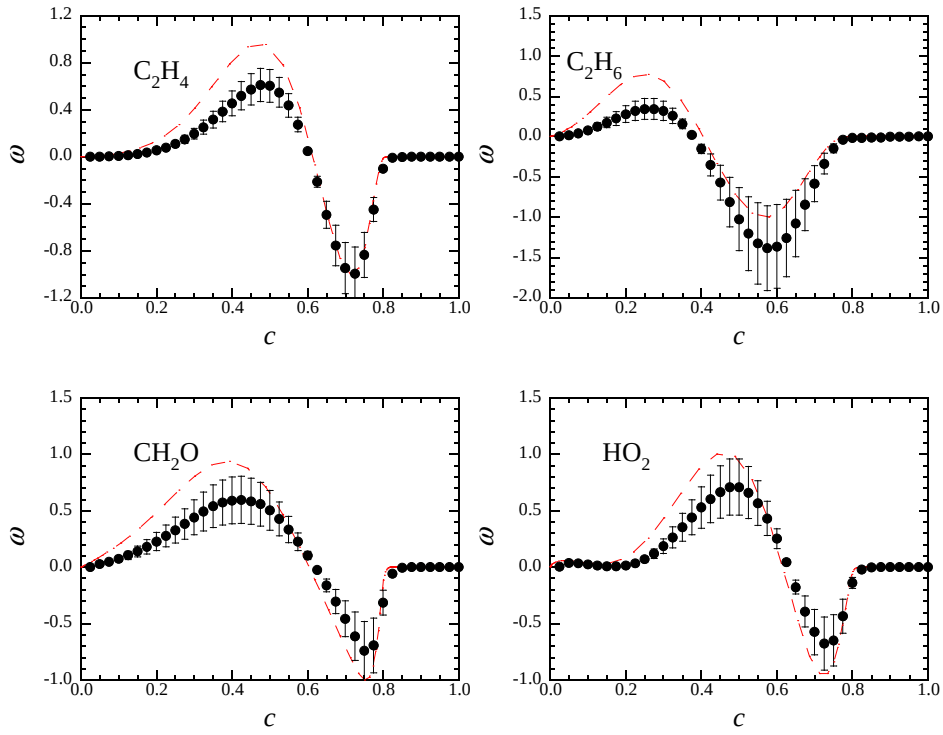

Figure 3.31: Normalized conditional means of reaction rates on the progress variable (c) for case 1 in preheat zone. (Red dashed line correspond to laminar flame. Full black symbols represent the conditional means of reaction rates for turbulent flame. Error bars represent the standard deviation of each reaction rate.)

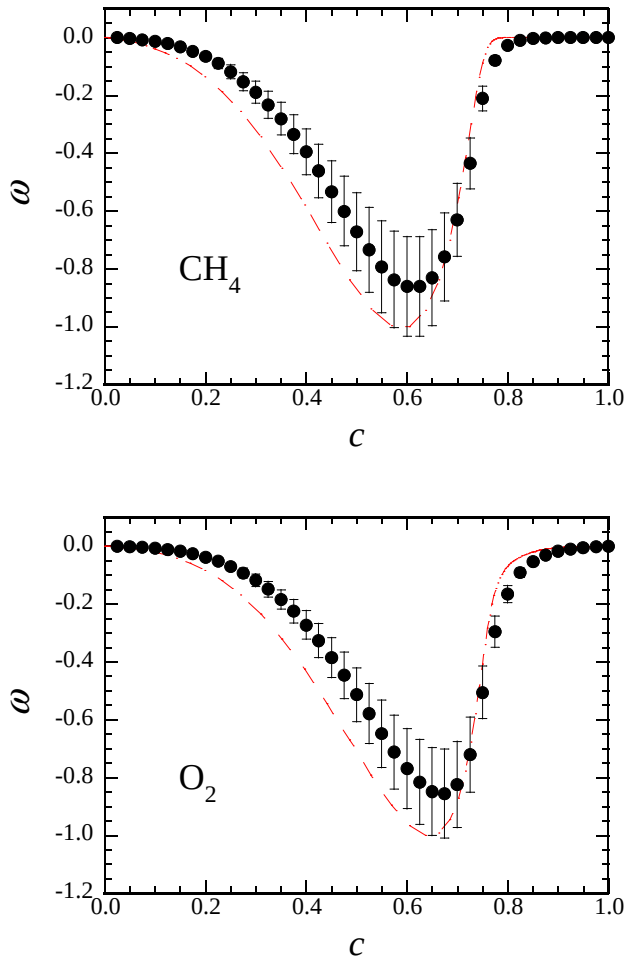

Figure 3.32: Normalized conditional means of reaction rates on the progress variable (c) for case 2 in reaction zone. (Red dashed line correspond to laminar flame. Full black symbols represent the conditional means of reaction rates for turbulent flame. Error bars represent the standard deviation of each reaction rate.)

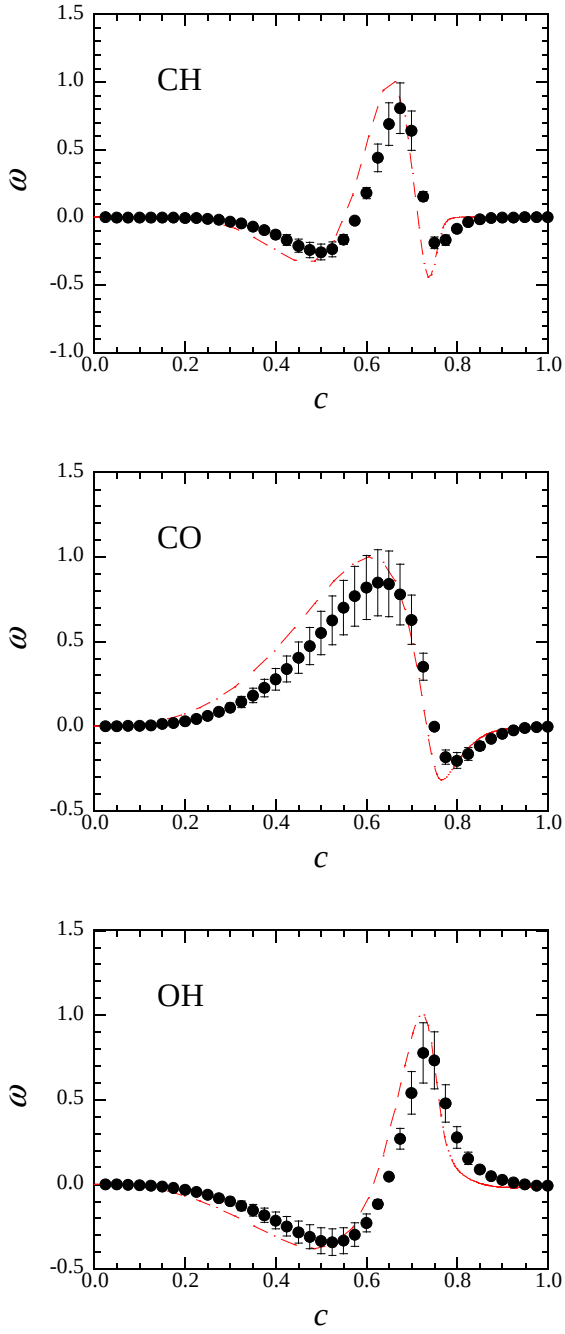

Figure 3.33: Normalized conditional means of reaction rates of the key species on the progress variable (c) for case 2. (Red dashed line correspond to laminar flame. Full black symbols represent the conditional means of reaction rates for turbulent flame. Error bars represent the standard deviation of each reaction rate.)

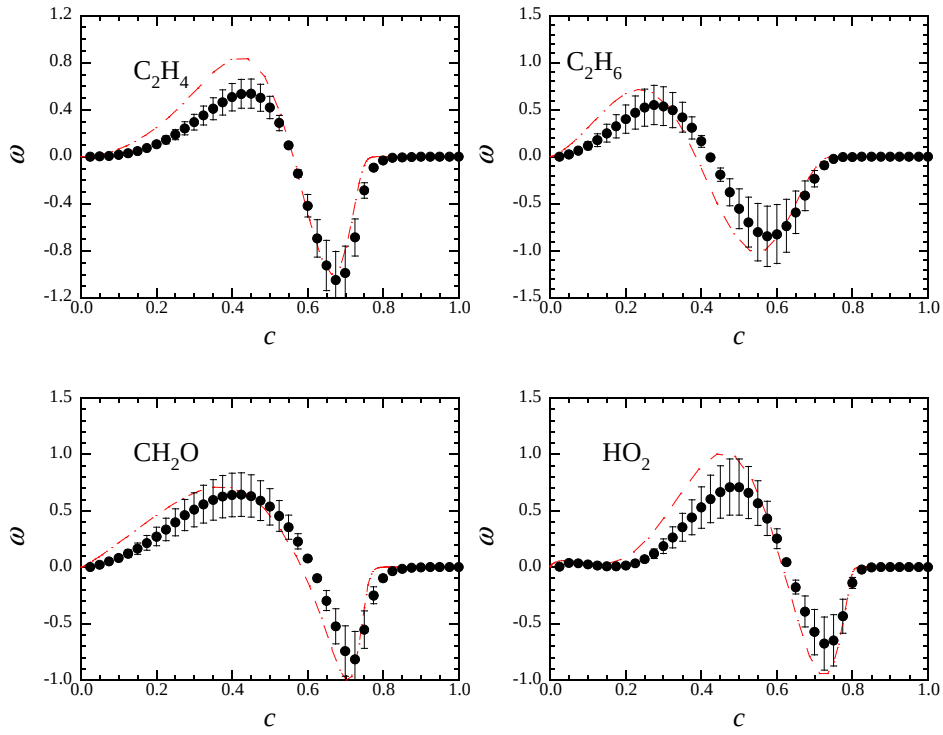

Figure 3.34: Normalized conditional means of reaction rates on the progress variable (c) for case 2 in preheat zone. (Red dashed line correspond to laminar flame. Full black symbols represent the conditional means of reaction rates for turbulent flame. Error bars represent the standard deviation of each reaction rate.)

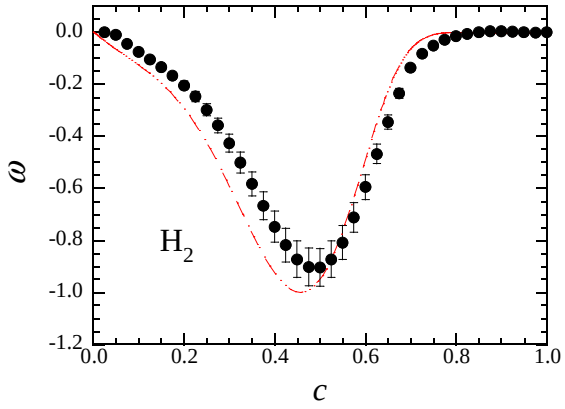

(a)

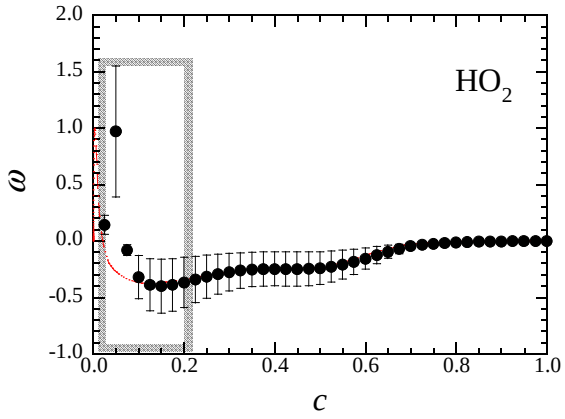

(b)

Figure 3.35: Normalized conditional means of reaction rates on the progress variable (c) for H_2–air flame. (Red dashed line correspond to laminar flame. Full black symbols represent the conditional means of reaction rates for turbulent flame. Error bars represent the standard deviation of each reaction rate.)

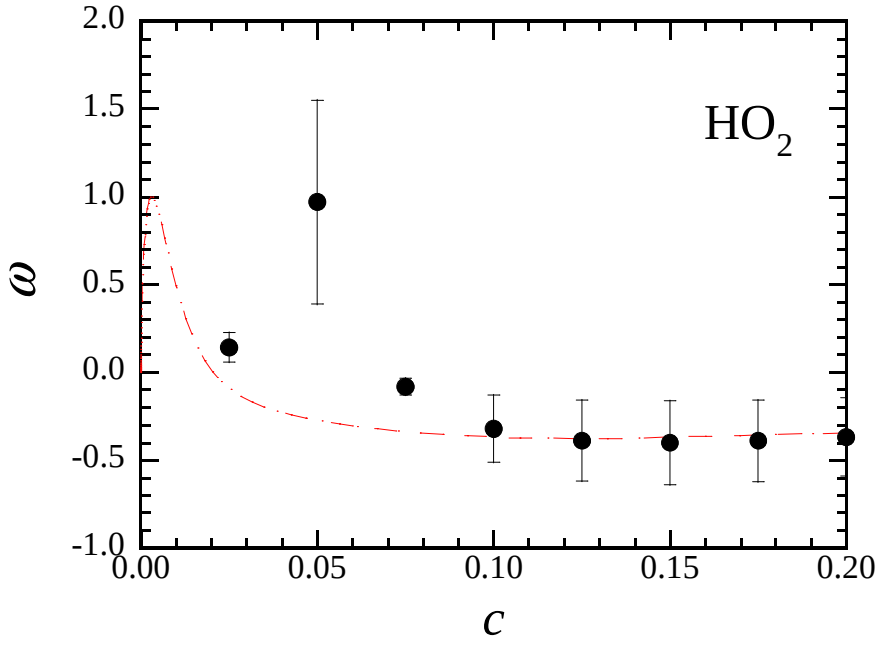

Figure 3.36: Magnification of the region represented by solid box in Figure 3.35 (b)

3.4.3 Correlations of heat release rate with flame curvature and tangential strain rate in methane–air premixed flames

In our previous studies [23, 33, 37, 54], it was revealed that the heat release rate has good correlation with flame front curvature in H_2–air flames in the corrugated flamelets and the thin reaction zones regime. This phenomena is also investigated in the present methane–air premixed flames. Figure 3.37 shows the joint pdf of principle curvatures (k_1 and k_2) with the conditional mean value of heat release rate normalized by ΔH_L. Here, the principle curvature are normalized by η in the unburned side. Probability difference between neighboring contour lines are 2.0. Tanahashi et al. [84] have shown that, with k_1 and k_2, the shape of flame front can be classified into spherical surface convex toward the burned side (S-B), cylindrical surface convex toward the burned side (C-B), hyperboloidal surface (HB), cylindrical surface convex toward the unburned side (C-U) and spherical surface convex toward the unburned side (S-U). For the case 1, as shown in Fig. 3.37 (a), the heat release rate higher than the corresponding laminar flame, around 40% and 30% higher, can be observed in the S-B and C-B region, respectively. For the lean methane flame, the case 2, in Fig. 3.37 (b), heat release reaches up to 1.2 times that of laminar flame in S-B and C-B regions. The heat release rate correlates well with flame front curvature for the both flames, in other words, the flame front convex towards the burned side tends to have higher heat release rate than that convex towards the unburned side. Similar correlations were also observed for the lean methane–air premixed flames [49] and the hydrogen–air premixed flames [23, 37, 54].

Figure 3.38 shows the joint pdf of tangential strain rate with conditional mean value of normalized heat release rate. α_{t1} and α_{t2} represent the minimum and maximum tangential strain rates. Probability difference between neighboring contour lines are 2.0. With these two values, it has been shown that [84] tangential strain rate on the flame surface can be classified into stretching in two directions (S-S), stretching and compression in each direction (S-C) and compression in two

directions (C-C). The tangential strain rate is normalized by u'_{rms}/λ in the unburned side. As shown in Fig. 3.38 (a) and (b), for the both cases, most of the flame elements are stretched at least in one direction, and the maximum heat release can be found in S-S region. Although the heat release in S-S regime is relatively higher than that in S-C regime, the correlation between heat release and tangential strain rate is much weaker than that of heat release and principal curvature.

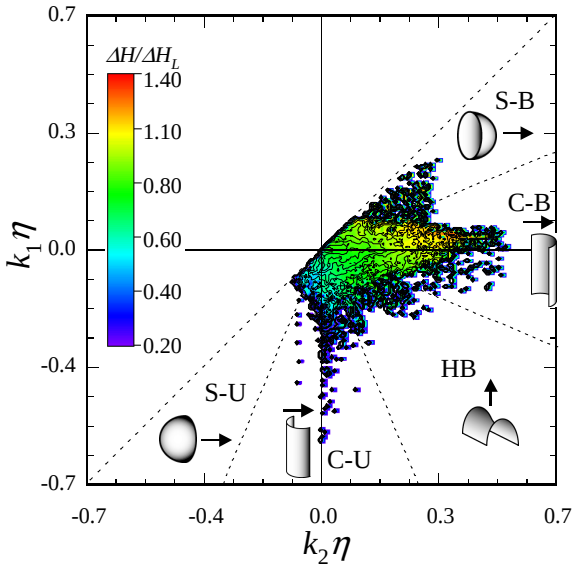

(a) Case 1

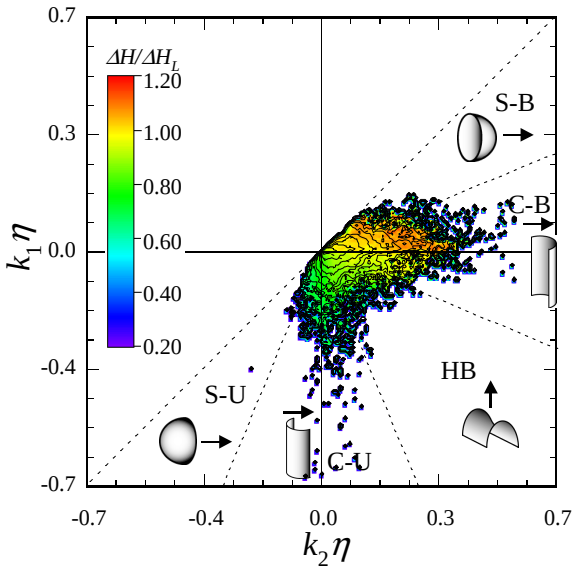

(b) Case 2

Figure 3.37: Joint pdfs of principal curvatures of flame front with conditional mean value of heat release rate. (Arrows show the burned side.)

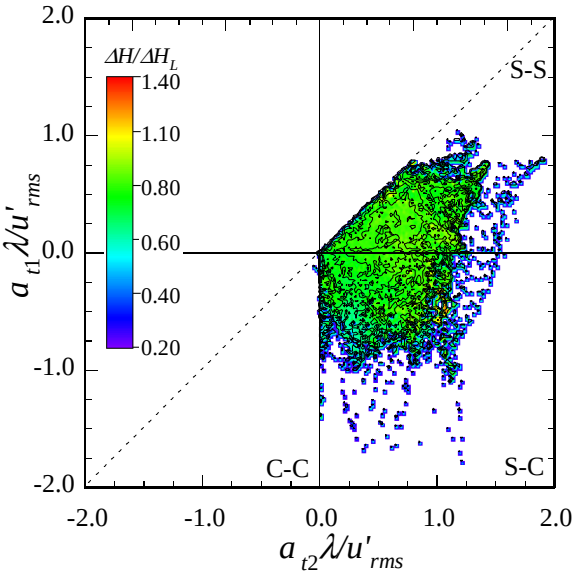

(a) Case 1

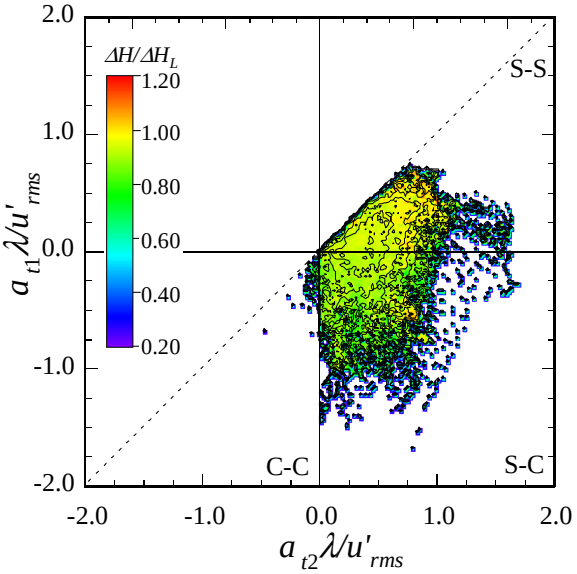

(b) Case 2

Figure 3.38: Joint pdfs of the minimum and maximum tangential strain rate with conditional mean value of heat release rate.

3.5 Conclusions of this chapter

In this chapter, three-dimensional DNS of methane–air turbulent premixed flames have been conducted using GRI-Mech 3.0 kinetic mechanism to investigate the local flame structures in the thin reaction zones regime. The following conclusions are obtained:

(1) The fine vortices make the flame front more complicated and increase the flame surface area. The fine vortices cannot survive behind the flame front due to the increase of viscosity and temperature rise in the burned region. Large region of heat release rate lower than the corresponding laminar flame was observed while heat release rate distributions show continuous structures at contour levels of $\Delta H/\Delta H_L$ = 0.8 and 0.6

(2) At relatively high temperature region where heat release rate is around 0.50-0,60ΔH_L, very low concentrations of OH radicals are observed which could result in difficulties in OH PLIF measurement to identify flame front in experiments. These sorts of flame structures could have significant effects on fractal analysis of the flame surface, therefore, for methane–air premixed flames, simultaneous CH-OH or CH_2O-OH PLIF measurements may give more accurate results on the flame front measurement in the thin reaction zones.

(3) The statistical characteristics of local flame elements have been investigated and compared with hydrogen–air premixed flame in the thin reaction zones. The most expected heat release rate in methane–air premixed flames are lower than their corresponding laminar flame, as the peaks of the pdfs show value around 90% that of laminar flame. For H_2–air flame, however, the most expected heat release rates are in the range from 1.0 to 1.1 times that of laminar flame.

(4) The most expected local flame thickness for all flames are thinner than

their corresponding laminar flame. On average, however, the mean flame thickness, δ_m, increases 10% that of laminar flame in the stoichiometric methane–air premixed flame despite the existence of mean positive strain rate. For the lean methane–air premixed flame, δ_m decreases 3% that of laminar flame. For H_2–air premixed flame, δ_m decreases around 26%. In the methane–air premixed flames, it has been found that the probability of thicker flame elements ($\delta/\delta_L > 1.0$) in the positive strain region is substantially higher than that in hydrogen–air flame. The flame thickening on average in the stoichiometric methane–air combustion could be attributed to the stretch effects.

(5) It is revealed that in the thin reaction zones, the minimum curvature radius of the flame front is about twice of the Kolmogorov scale. The peak of the pdf of the tangential strain rate is less than 1 Taylor time scale. The maximum strain rate tangential to the flame front in the thin reaction zones is about half of the value that is observed in the flamelet regime such as the corrugated flamelet and the wrinkled flamelet. These results show that in the thin reaction zones, the effect of turbulence motion on the flame front is not as strong.

(6) In methane flames, an asymmetrical dependence of flame elements on the flame front curvature can be observed. The majority of the thin flames ($\delta/\delta_L < 1.0$) are found in the positive curvature region. The thinnest flame can be found around 0-2/δ_L curvature region. In hydrogen flame, the probability of flame elements thinner than the corresponding laminar flame in the negative curvature region is relatively higher compared with those in methane flames. The asymmetrical dependence of flame elements to the flame front is also much less noticeable.

(7) In methane flames, the reaction rate profiles in the reaction zone and preheat zone skew to the higher temperature region and the mean value of reaction

rates decrease about 20% that of laminar flame due to turbulence. These results show that turbulence significantly affect the reaction layers although the reaction rates have similar profiles compared with those in the laminar flame. For hydrogen flame, the reaction rate profile in the preheat zone is significantly disturbed by turbulence. The stronger effects of turbulence on the preheat zone in hydrogen flame could be attributed to a much smaller Kolmogorov length scale and higher turbulent intensity.

(8) The correlation between heat release rate and three-dimensional geometrical shapes of the flame elements have been investigated for methane–air premixed flames. It has been revealed that the heat release rate tends to be larger in the positive curvature region than that in the negative curvature region, and increases up to 20-40% that of laminar flame. Most of the flame elements are stretched into one tangential direction at least, while a weaker correlation can be found between the heat release and tangential strain than that with curvature.

Chapter 4

Fractal characteristics of turbulent premixed flames

4.1 Preface

In turbulent premixed flames, wrinkling of flame surface area shows fractal characteristics [12, 37, 38]. Fractal characteristic means a geometric shape that shows similar pattern at different scale. It was first suggested by Mandelbrot [85] that the scalar iso-surfaces in turbulent flows exhibit fractal characteristics. An example for a fractal geometry is shown in Fig. 4.1. It can be seen that similar patterns can be found at different levels of magnification.

In flamelet regimes, increase in flame surface area mainly accounts for the increased turbulent burning velocity. Therefore, it is important to clarify global flame structures such as fractal dimension (D_3) and inner cutoff (ϵ_i) to develop a turbulent combustion model for large eddy simulation (LES). The ratio of wrinkled turbulent flame surface area (A_T) to laminar flame surface area (A_L) can be written as follows.

$$\frac{A_T}{A_L} = \left(\frac{\epsilon_i}{\epsilon_o}\right)^{2-D_3}, \tag{4.1}$$

Here, ϵ_o denote the outer cutoff of the flame surface area. Yoshikawa et al. [28] have proposed a fractal dynamic subgrid scale (FDSGS) combustion model which dynamically calculates the fractal dimension of the flame surface and effectively predicts the flame surface area.

Several studies have been done for the fractal characteristics of turbulent premixed flames. Shim et al. [37] conducted DNSs of hydrogen–air flames and investigated fractal dimension by a three-dimensional box counting method [86]. They showed that the fractal dimensions of hydrogen flames were $2.3 - 2.5$ and do not show systematic dependence on Reynolds number and equivalence ratio. Chatakonda et al. [38] investigated fractal characteristics of low Damköhler number flames and showed that fractal dimensions of premixed flames vary in time in the range of 2.1 and 2.7. Several researchers have proposed inner cutoff expression [7, 87]. On the other hand, Gülder and Smallwood [88] and Gülder et al. [12] showed that the fractal dimension is about 2.2 and inner cutoff expressions [7, 87] do not agree with experimental results and explained that these differences might be caused by the accuracy of the adopted different technique for fractal dimension analysis. These experimental and DNS data on the fractal characteristics of flame surface in literature show significant differences. Therefore, no general agreement has yet been reached on fractal characteristics.

In this chapter, fractal characteristics of hydrogen–air premixed flames in a constant volume vessel described in Chapter 2 and methane–air premixed flames in the thin reaction zones described in Chapter 3 are investigated.

4.2 Fractal characteristics of hydrogen–air premixed flames in a constant volume vessel

In this section, fractal characteristics of hydrogen–air premixed flames in a constant volume vessel (CVV) is investigated using the DNS database presented in chapter 2. A two-dimensional box counting method which gives fractal dimension within 1% [86] is adopted to calculate flame surface area due to the geometrical constraint. The flame front is defined by the contour surface of temperature as in our previous study [23]. The fractal dimension (D_2) is calculated in the center $x-z$ plane for both cases. A red-line plane represents the center $x-z$ plane in the computational domain is drawn in Fig. 4.2. Temperature distribution on the center

$x - z$ plane with contour surface of temperature can be seen in Fig. 4.3. Figure 4.4 shows fractal plots for the small vessel. The slope of this fractal plot gives the fractal dimension as $1 - D_2$. As this is a two-dimensional analysis, the additive rule [89] is applied. The additive rule states that the dimension of the measured cross sectional area plus one equals to true dimension of that object. Therefore, The slope of the fractal plot becomes $2 - D_2$. Fractal characteristics were calculated at different pressure (until flame impinging the side walls) to investigate the pressure rising effect. Since temperature and pressure increase in the present DNS, one-dimensional DNSs of laminar flame propagation were conducted to obtain the corresponding threshold temperature in which the heat release has a peak value in laminar flame, at each pressure. As shown in Fig. 4.5, pressure dependence of D_2 cannot be observed for both cases. The averaged value of the fractal dimension is 2.24 and 2.23 for the small and large vessels, respectively. Different values of fractal dimension obtained from experiments [12, 90–93] could be caused by several factors such as experimental and analysis methods [94]. The inner cutoff is about 10.9η and 10.6η for the small and large vessels, respectively as shown in Fig. 4.6. In our previous study [37], it has been shown that inner cutoff is larger than that of nonreactive scalars in turbulence. Note that the most expected diameter of coherent fine scale eddies $D = 8\eta$ is the inner cutoff for non-reactive scalars [34–36].

Gülder and Smallwood [88] expressed inner cutoff as a function of Karlovitz number ($Ka = (u'_{rms}/S_L)^{3/2}(l/\delta_F)^{-1/2}$). Inner cutoff with respect to Ka is shown in Fig. 4.7 for both vessels as well as for the whole range of pressure. Ka number values are 0.0781 to 0.0491 for small vessel, and 0.0650 to 0.0372 for large vessel case in the increasing order of pressure ranging from 1.1 to 1.5 atm. Ka number decreases with increasing mean pressure for the both cases. Several experimental and DNS results [12, 37, 90, 95–97] and inner cutoff expressions [7, 87, 88, 98] listed in Table 4.1 are also plotted. Most of the expressions do not predict inner cutoff accurately except Poinsot et al. [87] at lower Ka number regime.

Shim et al. [37] expressed inner cutoff as a function of D/δ_F, where D and δ_F denote the most expected diameter of coherent fine scale eddy and laminar flame thickness, respectively. Figure 4.8 shows inner cutoff as a function of D/δ_F for both cases. For comparison, several experimental and DNS data are also plotted [12, 37, 90, 95–97]. Inner cutoff expressions of several researchers [7, 87, 88, 98] from Table 4.1 are re-expressed by a function of D/δ_F and listed in Table 4.2. Here, in the formulae of Shim et al. [37], C was selected to be 6.0 by the least-squares method. Only the formulae of Poinsot et al. [87] and Shim et al. [37] can predict the inner cutoff. However, the formula of Poinsot et al. [87] cannot make accurate prediction of inner cutoff for small D/δ_F. Inner cutoff calculated from this study and all other sets of data show good agreement with the formula of Shim et al. [37]. This result suggests that the D/δ_F based expression can be applied for the pressure rising condition.

Table 4.1: Inner cutoff expression as a function of Ka in previous studies.

Reference	ϵ_i/δ_F
Peters [7]	Ka^{-2}
Poinsot et al. [87]	$0.74 + 16.4Ka^{-1/3}$
Roberts et al. [98]	$7Ka^{-1/2}$
Gülder and Smallwood [88]	$22Ka^{-1/2}$

Table 4.2: Inner cutoff expression as a function of D/δ_F.

Reference	ϵ_i/η
Peters [7]	$1/8^3(D/\delta_F)^3$
Poinsot et al. [87]	$5.92(D/\delta_F)^{-1} + 32.8(D/\delta_F)^{-1/3}$
Roberts et al. [98]	7
Gülder and Smallwood [88]	22
Shim et al. [37]	$8\exp[C(\delta_F/D)]$

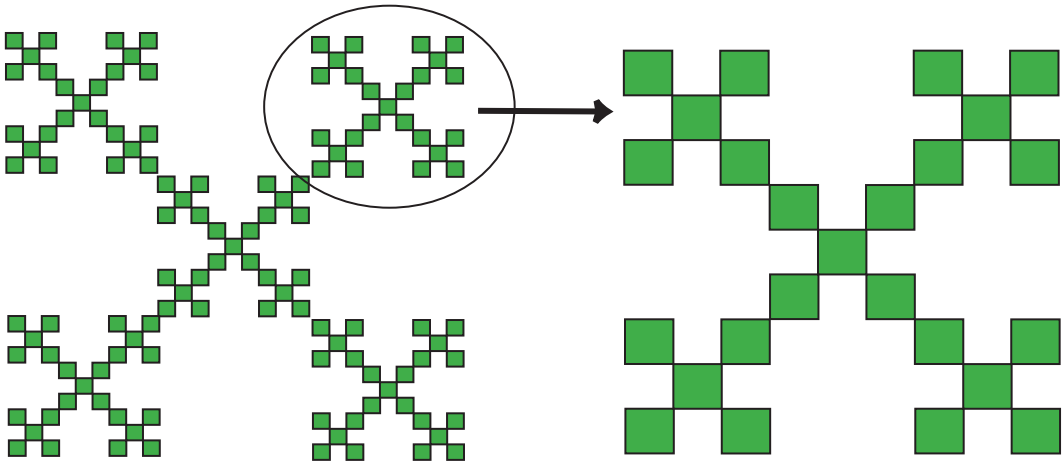

Figure 4.1: An example for the box fractal geometry [99].

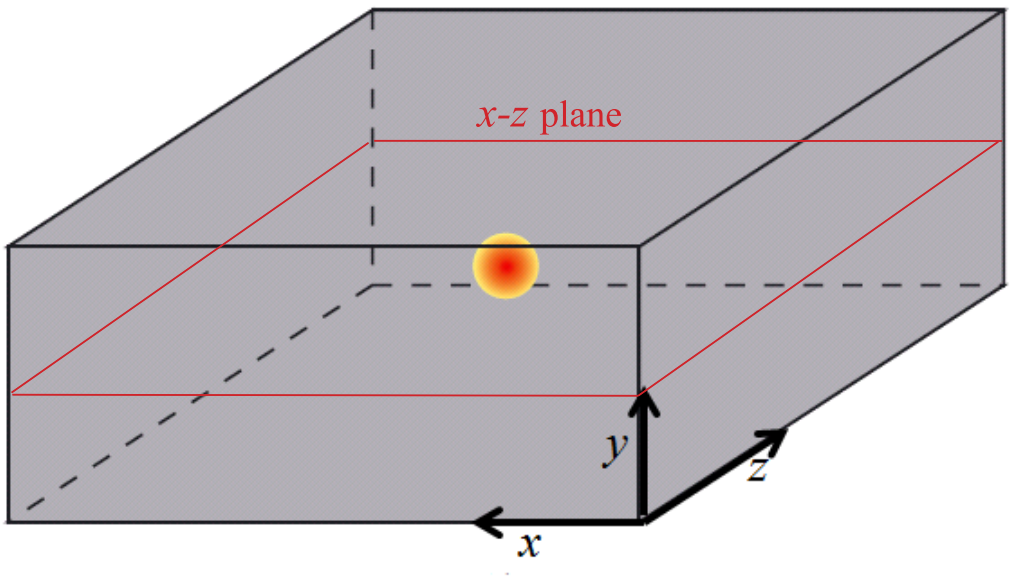

Figure 4.2: Schematic of computational domain.

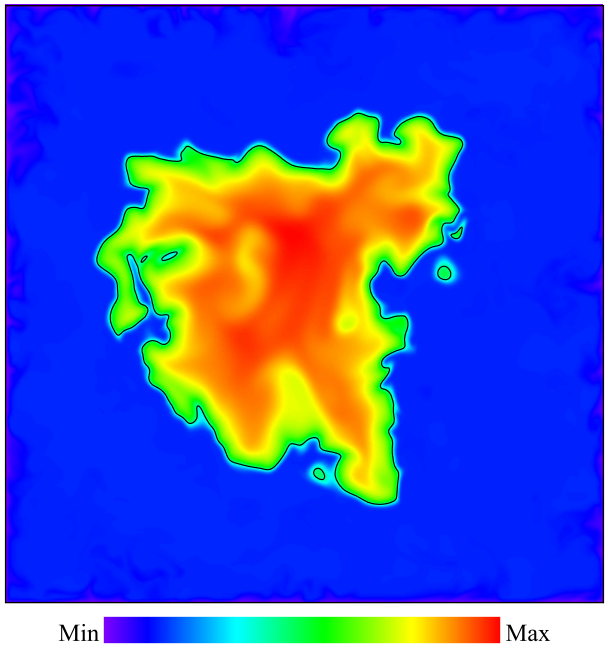

Figure 4.3: Temperature distribution with contour line (Black, T=1260 K.)on the center $x-z$ plane (a red-line plane in Fig. 4.2) for the small vessel.

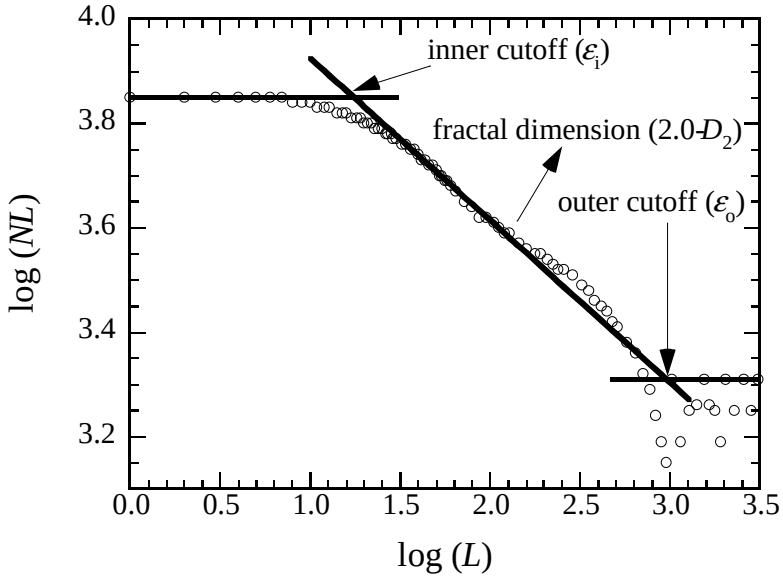

Figure 4.4: An example of fractal plots of flame surface defined from temperature for the small vessel.

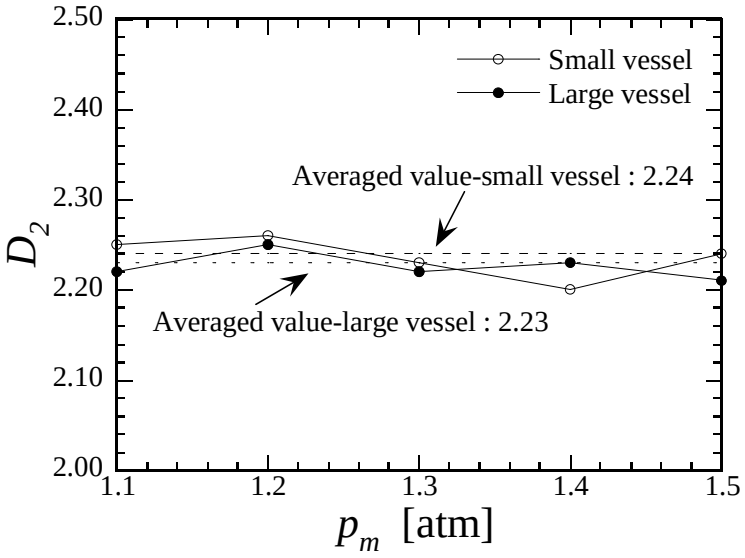

Figure 4.5: Fractal dimension as a function of mean pressure in the small and large vessels.

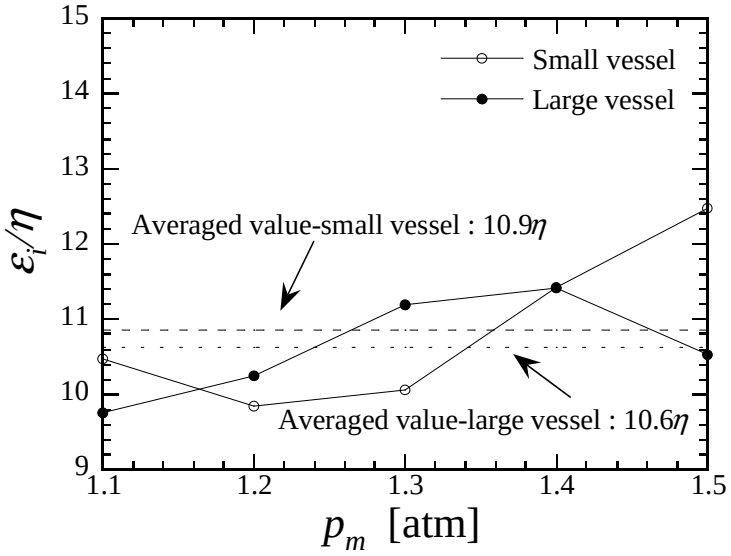

Figure 4.6: Inner cutoff as a function of mean pressure in the small and large vessels.

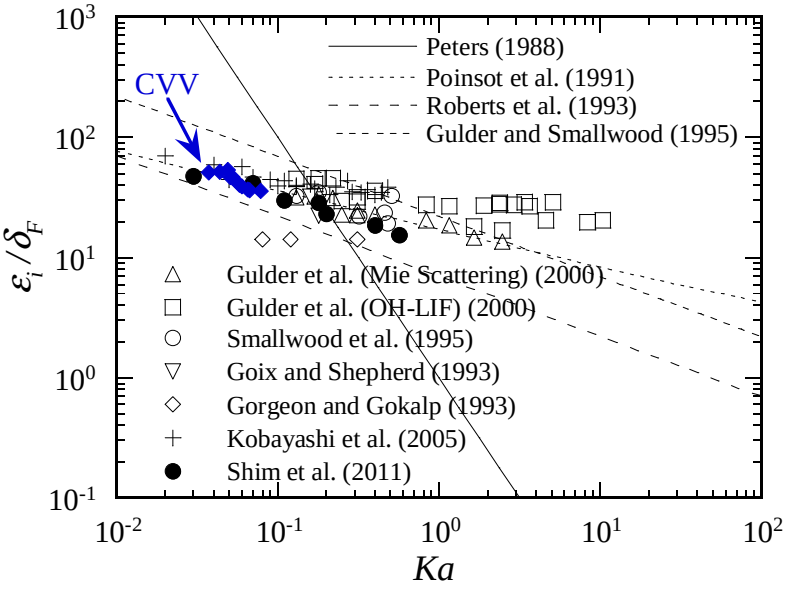

Figure 4.7: Relationship between the inner cutoff of flame surface and Karlovitz number.

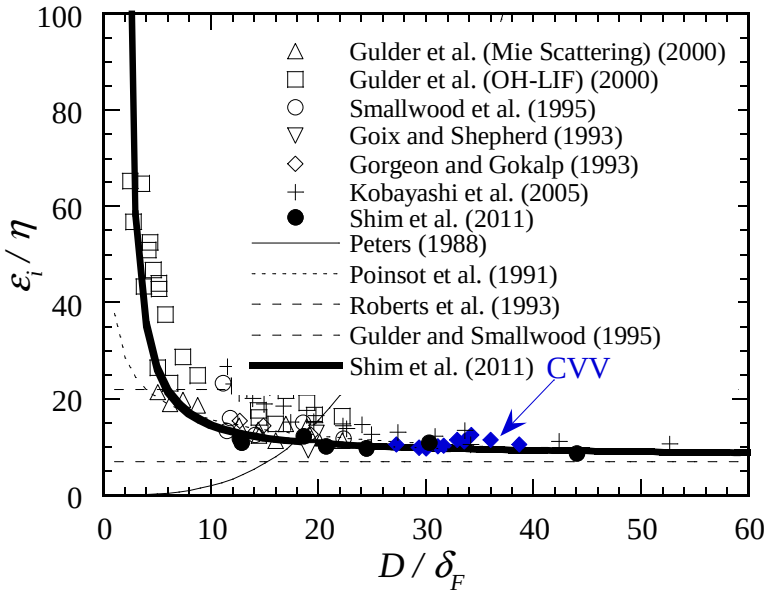

Figure 4.8: Dependence of the inner cutoff on D/δ_F and comparison of various inner cutoff expressions and experimental results.

4.3 Fractal characteristics of methane–air premixed flames in thin reaction zones

In this section, fractal characteristics of the stoichiometric (Case 1) and the lean (Case 2) methane–air turbulent premixed planar flames in the thin reaction zones are investigated using the DNS database presented in chapter 3. A three-dimensional box counting method which gives fractal dimension within 1% [86] is adopted to calculate the flame surface area. The flame front is defined by the contour surface of temperature as in our previous study [23]. Threshold temperatures are calculated by one-dimensional DNS of laminar methane–air premixed flame. The temperature contour surface which shows the peak value of heat release rate in the corresponding laminar flame are 1944 K and 1675 K for the case 1 and the case 2, respectively. The temperature contour surfaces for both cases were drawn and shown in Fig. 3.5. Distribution of temperature on a typical plane for both methane flames with temperature contour surface can be seen in Fig. 4.9.

Figure 4.10 shows the fractal plots of flame surface defined from temperature for both cases. From these plots, the fractal dimension (D_3) and inner cutoff can be calculated as the slope of the fractal plot equals to $2 - D_3$. Figure 4.11 shows temporal developments of D_3 for both cases. Here, the time is normalized by eddy turn-over time. It can be seen that D_3 increases linearly as the flame surface develops and has higher values for the case 1. After 3 eddy turnover time, the increase rate of D_3 for the case 2 decreases. D_3 reaches up to around 2.5 for the both cases. Temporal developments of the inner cutoff normalized by η are shown in Fig. 4.12. For the both cases, the inner cutoff reaches up to higher values as flame develops while showing somewhat different profiles. Between $2\tau_l$ and $3\tau_l$, the case 2 shows almost constant ϵ_i, while in the case 1, ϵ_i increases slowly. After that period, ϵ_i starts to increase linearly in the case 2, whereas a decreasing profile can be observed for the case 1. It can be seen that ϵ_i reaches up to around 16η for the both cases.

Inner cutoff as a function of Karlovitz number are drawn for the both cases in

Fig. 4.13. It should be noted that the inner cutoff values obtained from hydrogen–air flames in CVV in section 4.2 are also plotted along with DNS and experimental data [12, 37, 90, 95–97]. As was discussed in section 4.2, the inner cutoff expressions presented in Table 4.1 cannot predict the inner cutoff and the only relatively good prediction was made at lower Ka number. The present methane flames have relatively high Ka number, as shown in Fig. 4.13.

Inner cutoff as a function of D/δ_F can be seen in Fig. 4.14. For comparison, the results from section 4.2, the DNS and experimental data [12, 37, 90, 95–97] from literature are also plotted. From this figure, it can be clearly seen that the correlation function based on D/δ_F from Shim et al. [37] which is listed in Table 4.2 can predict the inner cutoff of present methane–air premixed flames. Hiraoka et al. [100] recently conducted fractal analysis and showed that the correlation function from Shim et al. [37] successfully predicts the inner cutoff of hydrogen–air premixed flames close to the boundary between the corrugated flamelet and the thin reaction zones regimes. The present study shows that the D/δ_F based expression can be used even in the thin reaction zones regime.

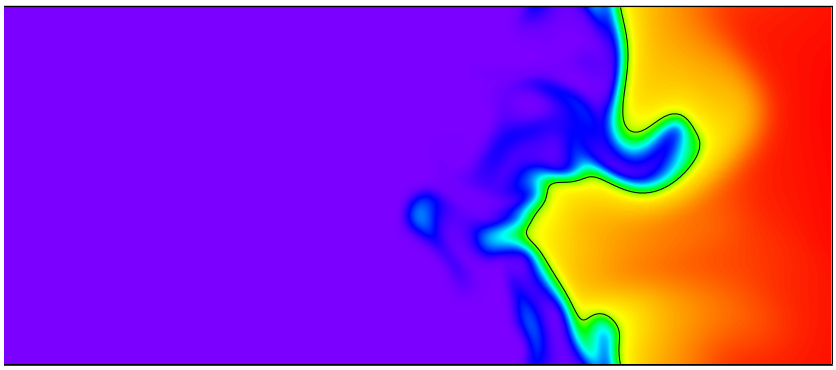

(a) Case 1 (Black, T=1944 K)

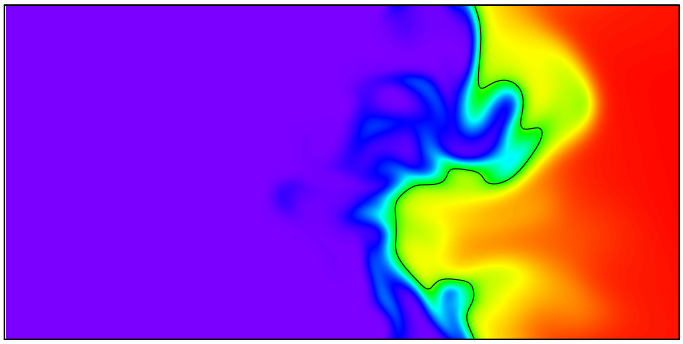

(b) Case 2 (Black, T=1675 K)

Figure 4.9: Distributions of Temperature on a typical plane with contour line for case 1 (a) and case 2 (b).

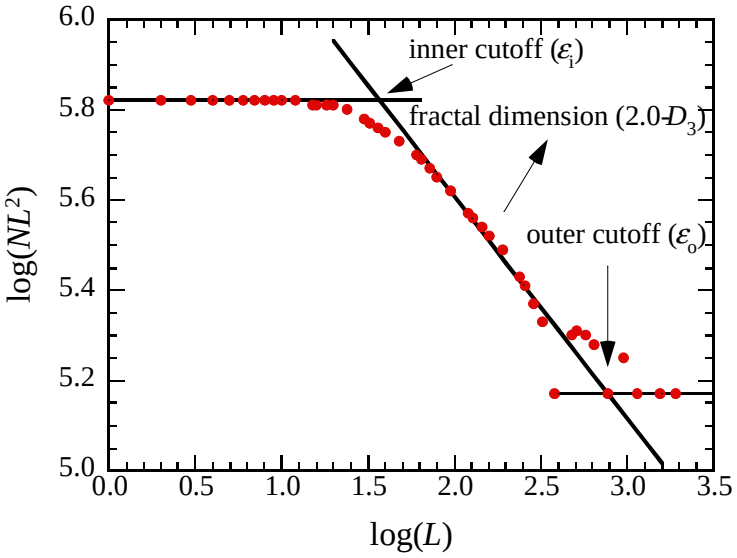

(a) Case 1

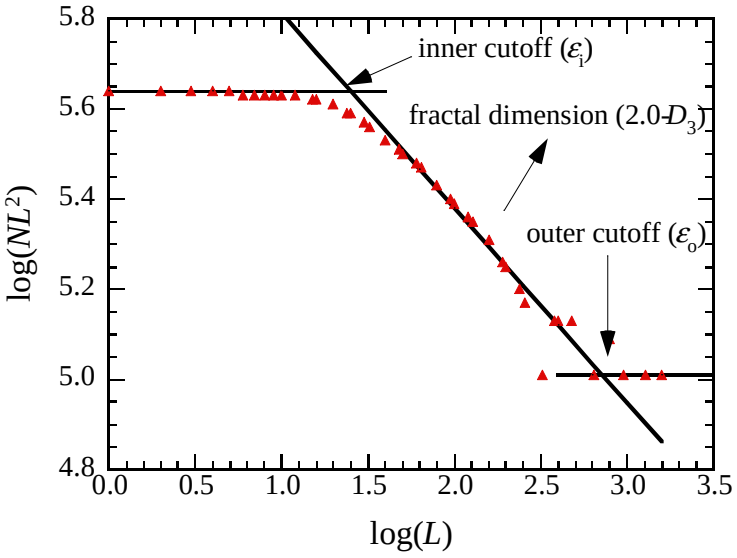

(b) Case 2

Figure 4.10: Fractal plots of flame surface defined from temperature contour surface for case 1 (a) and case 2 (b).

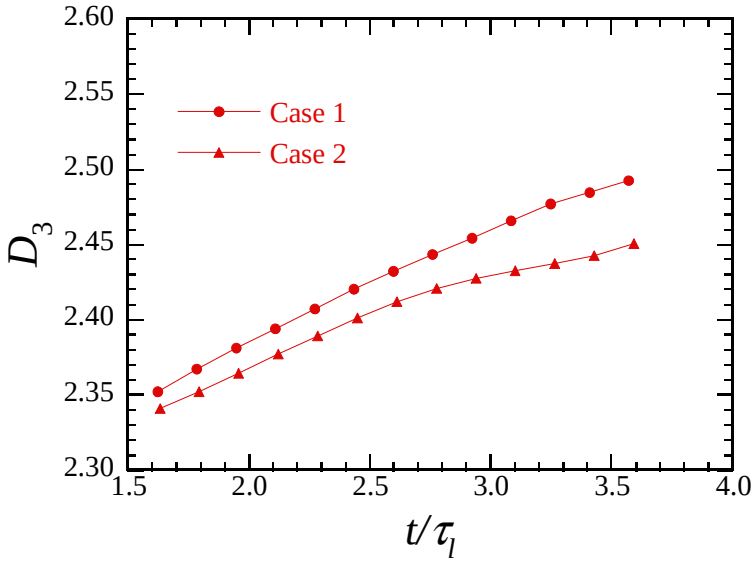

Figure 4.11: Temporal developments of fractal dimension for case 1 and case 2.

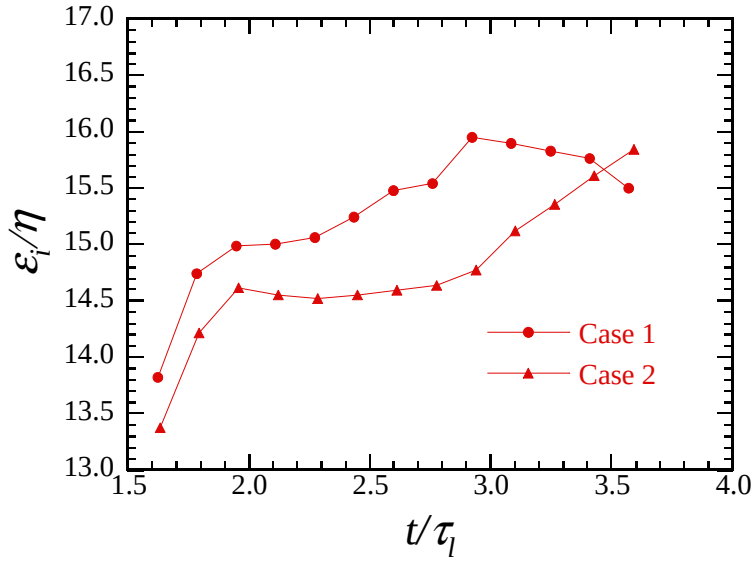

Figure 4.12: Temporal developments of inner cutoff for case 1 and case 2.

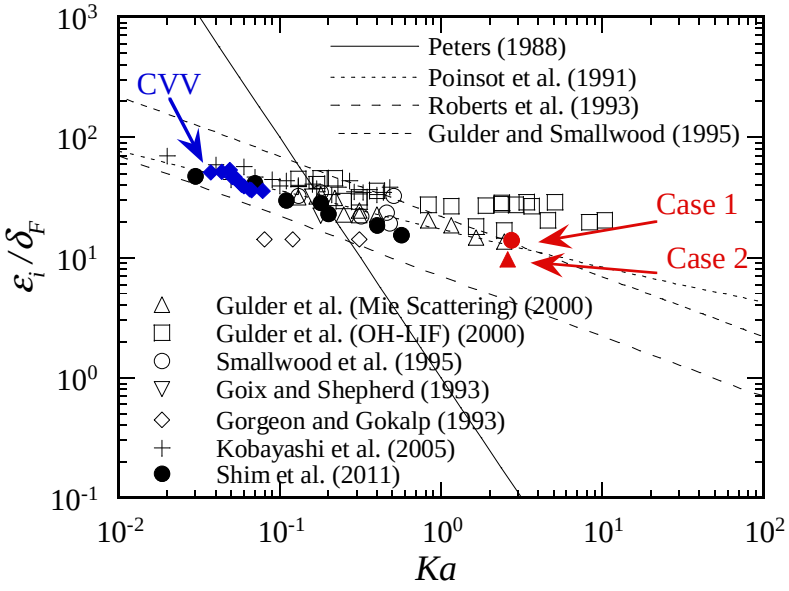

Figure 4.13: Relationship between the inner cutoff of flame surface and Karlovitz number.

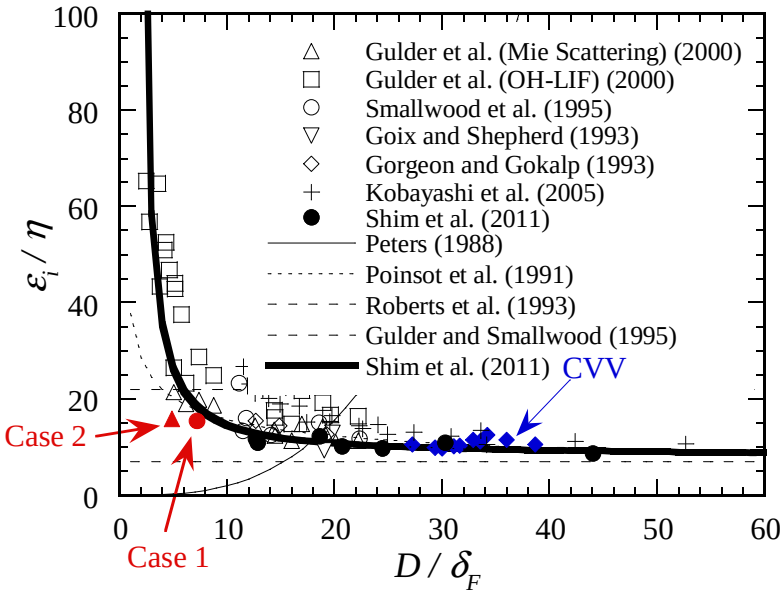

Figure 4.14: Dependence of the inner cutoff on D/δ_F and comparison of various inner cutoff expressions and experimental results.

4.4 Conclusions of this chapter

In this chapter, fractal characteristics of hydrogen–air premixed flame in a constant volume vessel and methane–air turbulent premixed planar flames in the thin reaction zones have been investigated using the DNS database from chapter 2 and 3. The following conclusions are obtained:

(1) For the hydrogen–air turbulent premixed flame in a constant volume vessel, it is clarified that the fractal dimension of the flame surface does not show any dependence on pressure increase, the averaged fractal dimension is 2.2. The inner cutoff is about 11η and larger than that of nonreactive scalars in turbulence. The inner cutoff obtained in the pressure rising condition is in good agreement with the expression proposed by Shim et al. [37]. This result suggests that the D/δ_F based expression can be applied for the pressure rising condition.

(2) For the methane–air turbulent premixed planar flames in the thin reaction zones, the fractal dimension increases as the flame develops and reaches about 2.5. The inner cutoff reaches about 16η. It is revealed that a good prediction of the inner cutoff of methane–air premixed flames in the thin reaction zones can be made with the D/δ_F based expression [37]. This result shows that the D/δ_F based expression can be used to predict inner cutoff in the thin reaction zones.

Chapter 5

Conclusions

In this thesis, direct numerical simulations have been conducted to investigate the turbulence–flame interactions and fractal characteristics of turbulent premixed flames. The results from each chapter are summarized as follows:

In chapter 2, three-dimensional DNS of hydrogen–air turbulent premixed flames at relatively high Reynolds number in a constant volume vessel configuration has been conducted considering the detailed kinetic mechanism to investigate the turbulence–flame interaction under pressure rising conditions. The following conclusions are obtained:

(1) The pressure increase in the vessel reduces the flame thickness and enhances the heat release rate at the flame front. The local pressure increase due to dilatation also enhances turbulence and finer scale vortices which results in a more complicated flame surface and an increase in the flame surface area.

(2) The Reynolds number based on Taylor micro scale increases with the mean pressure in the vessel, as turbulent intensity decreases.

(3) The increase in the mean pressure enhances the wall heat flux. The maximum wall heat flux is approximately proportional to the mean pressure after

the flame impinges on the wall, which suggests a possibility that the wall heat flux may be described as a function of pressure.

(4) Although the vessel sizes are different, 90% of the initial fuel has been consumed. However, when the combustion is almost over (R_{reac} = 0.9), heat loss is a little higher for the large vessel and reaches about 17%, this could be attributed to the different aspect ratio of 2 vessels and 2 times longer combustion in the large vessel.

(5) Local heat release rate, flame curvature and tangential strain rate could be scaled by ΔH_L of the corresponding pressure, η and u'_{rms}/λ in the unburned side, respectively, even for the pressure rising condition.

In chapter 3, three-dimensional DNSs of methane–air turbulent premixed flame have been conducted using GRI-Mech 3.0 kinetic mechanism to investigate the local flame structures in the thin reaction zones regime. The following conclusions are obtained:

(1) The fine vortices make the flame front more complicated and increase the flame surface area. The fine vortices cannot survive behind the flame front due to the increase of viscosity and temperature rise in the burned region. Large region of heat release rate lower than the corresponding laminar flame was observed while heat release rate distributions show continuous structures at contour levels of $\Delta H/\Delta H_L$ = 0.8 and 0.6

(2) At relatively high temperature region where heat release rate is around 0.50-0,60ΔH_L, very low concentrations of OH radicals are observed which could result in difficulties in OH PLIF measurement to identify flame front in experiments. These sorts of flame structures could have significant effects on fractal analysis of the flame surface, therefore, for methane–air premixed

flames, simultaneous CH-OH or CH_2O-OH PLIF measurements may give more accurate results on the flame front measurement in the thin reaction zones.

(3) The statistical characteristics of local flame elements have been investigated and compared with hydrogen–air premixed flame in the thin reaction zones. The most expected heat release rate in methane–air premixed flames are lower than their corresponding laminar flame, as the peaks of the pdfs show value around 90% that of laminar flame. For hydrogen–air flame, however, the most expected heat release rates are in the range from 1.0 to 1.1 times that of laminar flame.

(4) The most expected local flame thickness for all flames are thinner than their corresponding laminar flame. On average, however, the mean flame thickness, δ_m, increases 10% that of laminar flame in the stoichiometric methane–air premixed flame despite the existence of mean positive strain rate. For the lean methane–air premixed flame, δ_m decreases 3% that of laminar flame. For hydrogen–air premixed flame, δ_m decreases around 26%. In the methane–air premixed flames, it has been found that the probability of thicker flame elements ($\delta/\delta_L > 1.0$) in the positive strain region is substantially higher than that in hydrogen–air flame. The flame thickening on average in the stoichiometric methane–air combustion could be attributed to the stretch effects.

(5) It is revealed that in the thin reaction zones, the minimum curvature radius of the flame front is about twice of the Kolmogorov scale. The peak of the pdf of the tangential strain rate is less than 1 Taylor time scale. The maximum strain rate tangential to the flame front in the thin reaction zones is about half of the value that is observed in the flamelet regime such as the corrugated flamelet and the wrinkled flamelet. These results show that in the thin reaction zones, the effect of turbulence motion on the flame front is

not as strong.

(6) In methane flames, an asymmetrical dependence of flame elements on the flame front curvature can be observed. The majority of the thin flames ($\delta/\delta_L < 1.0$) are found in the positive curvature region. The thinnest flame can be found around 0-2/δ_L curvature region. In hydrogen flame, the probability of flame elements thinner than the corresponding laminar flame in the negative curvature region is relatively higher compared with those in methane flames. The asymmetrical dependence of flame elements to the flame front is also much less noticeable.

(7) In methane flames, the reaction rate profiles in the reaction zone and preheat zone skew to the higher temperature region and the mean value of reaction rates decrease about 20$\%$ that of laminar flame due to turbulence. These results show that turbulence significantly affect the reaction layers although the reaction rates have similar profiles compared with those in the laminar flame. For hydrogen flame, the reaction rate profile in the preheat zone is significantly disturbed by turbulence. The stronger effects of turbulence on the preheat zone in hydrogen flame could be attributed to a much smaller Kolmogorov length scale and higher turbulent intensity.

(8) The correlation between heat release rate and three-dimensional geometrical shapes of the flame elements have been investigated for methane–air premixed flames. It has been revealed that the heat release rate tends to be larger in the positive curvature region than that in the negative curvature region, and increases up to 20-40$\%$ that of laminar flame. Most of the flame elements are stretched into one tangential direction at least, while a weaker correlation can be found between the heat release and tangential strain than that with curvature.

In chapter 4, fractal characteristics of hydrogen–air premixed flame in a constant volume vessel and methane–air turbulent premixed planar flames in the thin reaction zones have been investigated using the DNS database from chapter 2 and 3. The following conclusions are obtained:

(1) For the hydrogen–air turbulent premixed flame in a constant volume vessel, it is clarified that the fractal dimension of the flame surface does not show any dependence on pressure increase, the averaged fractal dimension is 2.24. The inner cutoff is about 11η and larger than that of nonreactive scalars in turbulence. The inner cutoff obtained in the pressure rising condition is in good agreement with the expression proposed by Shim et al. [37]. This result suggests that the D/δ_F based expression can be applied for the pressure rising condition.

(2) For the methane–air turbulent premixed planar flames in the thin reaction zones, the fractal dimension increases as the flame develops and reaches about 2.5. The inner cutoff reaches about 16η. It is revealed that a good prediction of the inner cutoff of methane–air premixed flames in the thin reaction zones can be made with the D/δ_F based expression [37]. This result shows that the D/δ_F based expression can be used to predict inner cutoff in the thin reaction zones.

References

[1] C. Le Quéré, R. J. Andres, T. Boden, T. Conway, R. A. Houghton, J. I. House, G. Marland, G. P. Peters, G. R. van der Werf, A. Ahlström, R. M. Andrew, L. Bopp, J. G. Canadell, P. Ciais, S. C. Doney, C. Enright, P. Friedlingstein, C. Huntingford, A. K. Jain, C. Jourdain, E. Kato, R. F. Keeling, K. Klein Goldewijk, S. Levis, P. Levy, M. Lomas, B. Poulter, M. R. Raupach, J. Schwinger, S. Sitch, B. D. Stocker, N. Viovy, S. Zaehle, N. Zeng, The global carbon budget 1959-2011, Earth System Science Data 5 (1) (2013) 165–185.
URL `http://www.earth-syst-sci-data.net/5/165/2013/`

[2] International energy outlook 2013, U.S. Energy Information Administration (2013) DOE/EIA–0484.

[3] International energy outlook 2014, U.S. Energy Information Administration (2014) DOE/EIA–0484.

[4] International energy statistics database; electricity generation, U.S. Energy Information Administration (2011).

[5] U.S. Energy Information Administration (2013)[link].
URL `www.eia.gov/todayinenergy/detail.cfm?id=13711`

[6] The Institute of Energy Economics, Japan (2014).

[7] N. Peters, Laminar flamelet concepts in turbulent combustion, Symposium (International) on Combustion 21 (1) (1988) 1231 – 1250. doi:http://dx.doi.org/10.1016/S0082-0784(88)80355-2.

[8] S. Pope, Computations of turbulent combustion: Progress and challenges, Symposium (International) on Combustion 23 (1) (1991) 591 – 612. doi:http://dx.doi.org/10.1016/S0082-0784(06)80307-3.

[9] K. Bray, Turbulent flows with premixed reactants, Turbulent Reacting Flows, Topics in Applied Physics 44 (1980) 115–183.

[10] N. Peters, Turbulent Combustion, Cambridge Monographs on Mechanics, Cambridge University Press, 2000.

[11] J. H. Frank, P. A. Kalt, R. W. Bilger, Measurements of conditional velocities in turbulent premixed flames by simultaneous OH PLIF and PIV, Combustion and Flame 116 (1-2) (1999) 220 – 232. doi:http://dx.doi.org/10.1016/S0010-2180(98)00041-8.

[12] Ö. L. Gülder, G. Smallwood, R. Wong, D. Snelling, R. Smith, B. Deschamps, J.-C. Sautet, Flame front surface characteristics in turbulent premixed propane/air combustion, Combustion and Flame 120 (4) (2000) 407 – 416. doi:http://dx.doi.org/10.1016/S0010-2180(99)00099-1.

[13] C. Kortschik, T. Plessing, N. Peters, Laser optical investigation of turbulent transport of temperature ahead of the preheat zone in a premixed flame, Combustion and Flame 136 (1-2) (2004) 43 – 50. doi:http://dx.doi.org/10.1016/j.combustflame.2003.09.018.

[14] M. Tanahashi, S. Murakami, G.-M. Choi, Y. Fukuchi, T. Miyauchi, Simultaneous CH-OH PLIF and stereoscopic PIV measurements of turbulent premixed flames, Proceedings of the Combustion Institute 30 (1) (2005) 1665 – 1672. doi:http://dx.doi.org/10.1016/j.proci.2004.08.270.

[15] F. T. Yuen, Ö. L. Gülder, Premixed turbulent flame front structure investigation by rayleigh scattering in the thin reaction zone regime, Proceedings of the Combustion Institute 32 (2) (2009) 1747 – 1754. doi:http://dx.doi.org/10.1016/j.proci.2008.08.005.

[16] M. Shimura, T. Ueda, G.-M. Choi, M. Tanahashi, T. Miyauchi, Simultaneous dual-plane CH PLIF, single-plane OH PLIF and dual-plane stereoscopic PIV measurements in methane-air turbulent premixed flames, Proceedings of the Combustion Institute 33 (1) (2011) 775 – 782. doi:http://dx.doi.org/10.1016/j.proci.2010.05.026.

[17] F. T. Yuen, Ö. L. Gülder, Turbulent premixed flame front dynamics and implications for limits of flamelet hypothesis, Proceedings of the Combustion Institute 34 (1) (2013) 1393 – 1400. doi:http://dx.doi.org/10.1016/j.proci.2012.06.167.

[18] W. Jones, B. Launder, The prediction of laminarization with a two-equation model of turbulence, International Journal of Heat and Mass Transfer 15 (2) (1972) 301 – 314. doi:http://dx.doi.org/10.1016/0017-9310(72)90076-2.

[19] B. Launder, D. Spalding, Lectures in mathematical models of turbulence, Academic Press, London (1972) .

[20] D. B. Spalding, Development of the eddy-break-up model of turbulent combustion, Symposium (International) on Combustion 16 (1) (1977) 1657 – 1663. doi:http://dx.doi.org/10.1016/S0082-0784(77)80444-X.

[21] B. Magnussen, B. Hjertager, On mathematical modeling of turbulent combustion with special emphasis on soot formation and combustion, Symposium (International) on Combustion 16 (1) (1977) 719 – 729. doi:http://dx.doi.org/10.1016/S0082-0784(77)80366-4.

[22] N. Swaminathan, K. N. C. Bray, Turbulent premixed flames, Cambridge University Press, Cambridge, UK (2011) .

[23] M. Tanahashi, M. Fujimura, T. Miyauchi, Coherent fine-scale eddies in turbulent premixed flames, Proceedings of the Combustion Institute 28 (1) (2000) 529 – 535. doi:http://dx.doi.org/10.1016/S0082-0784(00)80252-0.

[24] M. Tanahashi, Y. Nada, Y. Ito, T. Miauchi, Local flame structure in the well-stirred reactor regime, Proceedings of the Combustion Institute 29 (2) (2002) 2041 – 2049. doi:http://dx.doi.org/10.1016/S1540-7489(02)80249-8.

[25] A. Poludnenko, E. Oran, The interaction of high-speed turbulence with flames: Global properties and internal flame structure, Combustion and Flame 157 (5) (2010) 995 – 1011. doi:http://dx.doi.org/10.1016/j.combustflame.2009.11.018.

[26] A. Poludnenko, E. Oran, The interaction of high-speed turbulence with flames: Turbulent flame speed, Combustion and Flame 158 (2) (2011) 301 – 326. doi:http://dx.doi.org/10.1016/j.combustflame.2010.09.002.

[27] H. Kolla, J. W. Rogerson, N. Chakraborty, N. Swaminathan, Scalar dissipation rate modeling and its validation, Combustion Science and Technology 181 (3) (2009) 518–535. doi:http://dx.doi.org/10.1080/00102200802612419.

[28] I. Yoshikawa, Y.-S. Shim, Y. Nada, M. Tanahashi, T. Miyauchi, A dynamic SGS combustion model based on fractal characteristics of turbulent premixed flames, Proceedings of the Combustion Institute 34 (1) (2013) 1373 – 1381. doi:http://dx.doi.org/10.1016/j.proci.2012.06.166.

[29] J. Warnatz, Concentration-, pressure-, and temperature-dependence of the flame velocity in hydrogen-oxygen-nitrogen mixtures, Combustion Science and Technology 26 (5-6) (1981) 203–213. doi:http://dx.doi.org/10.1080/00102208108946961.

[30] T. Poinsot, D. Veynante, S. Candel, Quenching processes and premixed turbulent combustion diagrams, Journal of Fluid Mechanics 228 (1991) 561–606. doi:http://dx.doi.org/10.1017/S0022112091002823.

[31] M. Baum, T. J. Poinsot, D. C. Haworth, N. Darabiha, Direct numerical simulation of $H_2/O_2/N_2$ flames with complex chemistry in two-dimensional turbulent flows, Journal of Fluid Mechanics 281 (1994) 1–32. doi:http://dx.doi.org/10.1017/S0022112094003010.

[32] A. Trouvé, T. Poinsot, The evolution equation for the flame surface density in turbulent premixed combustion, Journal of Fluid Mechanics 278 (1994) 1–31. doi:http://dx.doi.org/10.1017/S0022112094003599.

[33] Y. Nada, M. Tanahashi , T. Miyauchi, Effect of turbulence characteristics on local flame structure of H_2-air premixed flames, Journal of Turbulence (2004) N16.doi:http://dx.doi.org/10.1088/1468-5248/5/1/016.

[34] M. Tanahashi, S.-J. Kang, T. Miyamoto, S. Shiokawa, T. Miyauchi, Scaling law of fine scale eddies in turbulent channel flows up to Re_τ=800, International Journal of Heat and Fluid Flow 25 (3) (2004) 331 – 340. doi:http://dx.doi.org/10.1016/j.ijheatfluidflow.2004.02.016.

[35] Y. Wang, M. Tanahashi, T. Miyauchi, Coherent fine scale eddies in turbulence transition of spatially-developing mixing layer, International Journal of Heat and Fluid Flow 28 (6) (2007) 1280 – 1290. doi:http://dx.doi.org/10.1016/j.ijheatfluidflow.2007.06.009.

[36] M. Tanahashi, K. Fujibayashi, T. Miyauchi, Fine scale eddy cluster and energy cascade in homogeneous isotropic turbulence, IUTAM Symposium on Computational Physics and New Perspectives in Turbulence 4 (2008) 67–72.

[37] Y.-S. Shim, S. Tanaka, M. Tanahashi, T. Miyauchi, Local structure and fractal characteristics of H_2-air turbulent premixed flame, Pro-

ceedings of the Combustion Institute 33 (1) (2011) 1455 – 1462. doi:http://dx.doi.org/10.1016/j.proci.2010.09.002.

[38] O. Chatakonda, E. R. Hawkes, A. J. Aspden, A. R. Kerstein, H. Kolla, J. H. Chen, On the fractal characteristics of low damkohler number flames, Combustion and Flame 160 (11) (2013) 2422 – 2433. doi:http://dx.doi.org/10.1016/j.combustflame.2013.05.007.

[39] E. R. Hawkes, O. Chatakonda, H. Kolla, A. R. Kerstein, J. H. Chen, A petascale direct numerical simulation study of the modelling of flame wrinkling for large-eddy simulations in intense turbulence, Combustion and Flame 159 (8) (2012) 2690 – 2703, special Issue on Turbulent Combustion. doi:http://dx.doi.org/10.1016/j.combustflame.2011.11.020.

[40] J. B. Bell, M. S. Day, I. G. Shepherd, M. R. Johnson, R. K. Cheng, J. F. Grcar, V. E. Beckner, M. J. Lijewski, Numerical simulation of a laboratory-scale turbulent V-flame, Proceedings of the National Academy of Sciences of the United States of America 102 (29) (2005) 10006–10011. doi:http://dx.doi.org/10.1073/pnas.0504140102.

[41] Y. Minamoto, N. Fukushima, M. Tanahashi, T. Miyauchi, T. D. Dunstan, N. Swaminathan, Effect of flow-geometry on turbulence-scalar interaction in premixed flames, Physics of Fluids 23 (12) (2011) 125107. doi:http://dx.doi.org/10.1063/1.3665619.

[42] A. Gruber, R. Sankaran, E. R. Hawkes, J. H. Chen, Turbulent flame-wall interaction: a direct numerical simulation study, Journal of Fluid Mechanics 658 (2010) 5–32. doi:http://dx.doi.org/10.1017/S0022112010001278.

[43] S. Tanaka, M. Shimura, N. Fukushima, M. Tanahashi, T. Miyauchi, DNS of turbulent swirling premixed flame in a micro gas turbine combustor, Proceedings of the Combustion Institute 33 (2) (2011) 3293 – 3300. doi:http://dx.doi.org/10.1016/j.proci.2010.07.034.

[44] H. Wang, K. Luo, K. Qiu, S. Lu, J. Fan, A DNS study of hydrogen/air swirling premixed flames with different equivalence ratios, International Journal of Hydrogen Energy 37 (6) (2012) 5246 – 5256. doi:http://dx.doi.org/10.1016/j.ijhydene.2011.12.043.

[45] M. Shimura, K. Yamawaki, N. Fukushima, Y. S. Shim, Y. Nada, M. Tanahashi, T. Miyauchi, Flame and eddy structures in hydrogen-air turbulent jet premixed flame, Journal of Turbulence (2012) N42doi:http://dx.doi.org/10.1080/14685248.2012.720022.

[46] T. Jin, K. Luo, S. Lu, J. Fan, DNS investigation on flame structure and scalar dissipation of a supersonic lifted hydrogen jet flame in heated coflow, International Journal of Hydrogen Energy 38 (23) (2013) 9886 – 9896. doi:http://dx.doi.org/10.1016/j.ijhydene.2013.05.107.

[47] J. B. Bell, M. S. Day, J. F. Grcar, M. J. Lijewski, J. F. Driscoll, S. A. Filatyev, Numerical simulation of a laboratory-scale turbulent slot flame, Proceedings of the Combustion Institute 31 (1) (2007) 1299 – 1307. doi:http://dx.doi.org/10.1016/j.proci.2006.07.186.

[48] G. A. Karim, Hydrogen as a spark ignition engine fuel, International Journal of Hydrogen Energy 28 (5) (2003) 569 – 577. doi:http://dx.doi.org/10.1016/S0360-3199(02)00150-7.

[49] J. B. Bell, M. S. Day, J. F. Grcar, Numerical simulation of premixed turbulent methane combustion, Proceedings of the Combustion Institute 29 (2) (2002) 1987 – 1993. doi:http://dx.doi.org/10.1016/S1540-7489(02)80242-5.

[50] D. Thevenin, Three-dimensional direct simulations and structure of expanding turbulent methane flames, Proceedings of the Combustion Institute 30 (1) (2005) 629 – 637. doi:http://dx.doi.org/10.1016/j.proci.2004.08.037.

[51] R. Sankaran, E. R. Hawkes, J. H. Chen, T. Lu, C. K. Law, Structure of a spatially developing turbulent lean methane-air bunsen flame, Proceedings of the Combustion Institute 31 (1) (2007) 1291 – 1298. doi:http://dx.doi.org/10.1016/j.proci.2006.08.025.

[52] G. Smith, D. Golden, M. Frenklach, N. Moriarty, B. Eiteneer, M. Goldenberg, C. Bowman, R. Hanson, S. Song, W. Gardiner, V. Lissianski, Z. Qin, Gri-mech 3.0.
URL `http://www.me.berkeley.edu/gri_mech/`

[53] R. Owston, V. Magi, J. Abraham, Interactions of hydrogen flames with walls: Influence of wall temperature, pressure, equivalence ratio, and diluents, International Journal of Hydrogen Energy 32 (12) (2007) 2094 – 2104. doi:http://dx.doi.org/10.1016/j.ijhydene.2006.07.030.

[54] Y.-S. Shim, N. Fukushima, M. Shimura, Y. Nada, M. Tanahashi, T. Miyauchi, Radical fingering in turbulent premixed flame classified into thin reaction zones, Proceedings of the Combustion Institute 34 (1) (2013) 1383 – 1391. doi:http://dx.doi.org/10.1016/j.proci.2012.08.005.

[55] R. J. Kee, G. Dixon-Lewis, J. Warnatz, M. E. Coltrin, J. A. Miller, A fortran computer code package for the evaluation of gas-phase multicomponent transport properties, Sandia National Laboratories (1986) Report No. SAND86–8246.

[56] R. J. Kee, F. M. Rupley, J. A. Miller, A fortran chemical kinetics package for the analysis of gas phase chemical kinetics, Sandia National Laboratories (1989) Report No. SAND89–8009B.

[57] E. Gutheil, G. Balakrishnan, F. Williams, Structure and extinction of hydrogen-air diffusion flames, in: N. Peters, B. Rogg (Eds.), Reduced Kinetic Mechanisms for Applications in Combustion Systems, Vol. 15 of Lec-

ture Notes in Physics Monographs, Springer Berlin Heidelberg, 1993, pp. 177–195.

[58] S. K. Lele, Compact finite difference schemes with spectral-like resolution, Journal of Computational Physics 103 (1) (1992) 16 – 42. doi:http://dx.doi.org/10.1016/0021-9991(92)90324-R.

[59] P. Brown, G. Byrne, A. Hindmarsh, Vode: A variable-coefficient ode solver, SIAM Journal on Scientific and Statistical Computing 10 (5) (1989) 1038–1051. doi:http://dx.doi.org/10.1137/0910062.

[60] T. Poinsot, S. Lele, Boundary conditions for direct simulations of compressible viscous flows, Journal of Computational Physics 101 (1) (1992) 104 – 129. doi:http://dx.doi.org/10.1016/0021-9991(92)90046-2.

[61] M. Baum, T. Poinsot, D. Thevenin, Accurate boundary conditions for multicomponent reactive flows, Journal of Computational Physics 116 (2) (1995) 247 – 261. doi:http://dx.doi.org/10.1006/jcph.1995.1024.

[62] J. Sotton, B. Boust, S. A. Labuda, M. Bellenoue, Head-on quenching of transient laminar flame: Heat flux and quenching distance measurements, Combustion Science and Technology 177 (7) (2005) 1305–1322. doi:http://dx.doi.org/10.1080/00102200590950485.

[63] H. Kobayashi, Experimental study of high-pressure turbulent premixed flames, Experimental Thermal and Fluid Science 26 (2-4) (2002) 375 – 387. doi:http://dx.doi.org/10.1016/S0894-1777(02)00149-8.

[64] A. Soika, F. Dinkelacker, A. Leipertz, Pressure influence on the flame front curvature of turbulent premixed flames: comparison between experiment and theory, Combustion and Flame 132 (3) (2003) 451 – 462. doi:http://dx.doi.org/10.1016/S0010-2180(02)00490-X.

[65] M. Emadi, D. Karkow, T. Salameh, A. Gohil, A. Ratner, Flame structure changes resulting from hydrogen-enrichment and pressurization for low-swirl premixed methane-air flames, International Journal of Hydrogen Energy 37 (13) (2012) 10397 – 10404. doi:http://dx.doi.org/10.1016/j.ijhydene.2012.04.017.

[66] H. Carlsson, R. Yu, X.-S. Bai, Flame structure analysis for categorization of lean premixed CH_2/air and H_2/air flames at high karlovitz numbers: Direct numerical simulation studies, Proceedings of the Combustion Institute 35 (2) (2015) 1425 – 1432. doi:http://dx.doi.org/10.1016/j.proci.2014.09.002.

[67] R. J. Kee, J. F. Gracar, M. D. Smooke, J. A. Miller, A fortran program for modelling steady laminar one-dimensional premixed flames, Sandia National Laboratories (1985) Report No. SAND85–8240.

[68] H. N. Najm, P. H. Paul, C. J. Mueller, P. S. Wyckoff, On the adequacy of certain experimental observables as measurements of flame burning rate, Combustion and Flame 113 (3) (1998) 312 – 332. doi:http://dx.doi.org/10.1016/S0010-2180(97)00209-5.

[69] P. H. Paul, H. N. Najm, Planar laser-induced fluorescence imaging of flame heat release rate, Symposium (International) on Combustion 27 (1) (1998) 43 – 50. doi:http://dx.doi.org/10.1016/S0082-0784(98)80388-3.

[70] J. Sjoholm, J. Rosell, B. Li, M. Richter, Z. Li, X.-S. Bai, M. Alden, Simultaneous visualization of OH, CH, CH_2O and toluene PLIF in a methane jet flame with varying degrees of turbulence, Proceedings of the Combustion Institute 34 (1) (2013) 1475 – 1482. doi:http://dx.doi.org/10.1016/j.proci.2012.05.037.

[71] S. Böckle, J. Kazenwadel, T. kunzelmann, D.-I. Shin, C. Schulz, J. Wolfrum, Simultaneous single-shot laser-based imaging of formaldehyde, OH,

and temperature in turbulent flames, Proceedings of the Combustion Institute 28 (1) (2000) 279 – 286. doi:http://dx.doi.org/10.1016/S0082-0784(00)80221-0.

[72] R. Balachandran, B. Ayoola, C. Kaminski, A. Dowling, E. Mastorakos, Experimental investigation of the nonlinear response of turbulent premixed flames to imposed inlet velocity oscillations, Combustion and Flame 143 (1-2) (2005) 37 – 55. doi:http://dx.doi.org/10.1016/j.combustflame.2005.04.009.

[73] M. Roder, T. Dreier, C. Schulz, Simultaneous measurement of localized heat-release with OH/CH_2O-LIF imaging and spatially integrated OH* chemiluminescence in turbulent swirl flames, Proceedings of the Combustion Institute 34 (2) (2013) 3549 – 3556. doi:http://dx.doi.org/10.1016/j.proci.2012.06.102.

[74] J. Kariuki, A. Dowlut, R. Yuan, R. Balachandran, E. Mastorakos, Heat release imaging in turbulent premixed methane-air flames close to blow-off, Proceedings of the Combustion Institute 35 (2) (2015) 1443 – 1450. doi:http://dx.doi.org/10.1016/j.proci.2014.05.144.

[75] R. L. Gordon, A. R. Masri, E. Mastorakos, Simultaneous rayleigh temperature, OH- and CH_2O-LIF imaging of methane jets in a vitiated coflow, Combustion and Flame 155 (1-2) (2008) 181 – 195. doi:http://dx.doi.org/10.1016/j.combustflame.2008.07.001.

[76] B. Zhou, C. Brackmann, Z. Li, M. Aldén, X.-S. Bai, Simultaneous multi-species and temperature visualization of premixed flames in the distributed reaction zone regime, Proceedings of the Combustion Institute 35 (2) (2015) 1409 – 1416. doi:http://dx.doi.org/10.1016/j.proci.2014.06.107.

[77] D. Haworth, R. Blint, B. Cuenot, T. Poinsot, Numerical simulation of turbulent propane-air combustion with nonhomogeneous reactants, Combustion

and Flame 121 (3) (2000) 395 – 417. doi:http://dx.doi.org/10.1016/S0010-2180(99)00148-0.

[78] T. Saito, M. Tanahashi, T. Miyauchi, Influence of turbulent intensity and fuel on the turbulent premixed flames, Journal of Combustion Society of Japan 44 (2002) 35 – 44.

[79] F. Dinkelacker, A. Soika, D. Most, D. Hofmann, A. Leipertz, W. Polifke, K. Dobbeling, Structure of locally quenched highly turbulent lean premixed flames, Symposium (International) on Combustion 27 (1) (1998) 857 – 865. doi:http://dx.doi.org/10.1016/S0082-0784(98)80482-7.

[80] A. Soika, F. Dinkelacker, A. Leipertz, Measurement of the resolved flame structure of turbulent premixed flames with constant reynolds number and varied stoichiometry, Symposium (International) on Combustion 27 (1) (1998) 785 – 792. doi:http://dx.doi.org/10.1016/S0082-0784(98)80473-6.

[81] A. Buschmann, F. Dinkelacker, T. Schafer, M. Schafer, J. Wolfrum, Measurement of the instantaneous detailed flame structure in turbulent premixed combustion, Symposium (International) on Combustion 26 (1) (1996) 437 – 445. doi:http://dx.doi.org/10.1016/S0082-0784(96)80246-3.

[82] P. Tamadonfar, O. L. Gülder, Experimental investigation of the inner structure of premixed turbulent methane/air flames in the thin reaction zones regime, Combustion and Flame 162 (1) (2015) 115 – 128. doi:http://dx.doi.org/10.1016/j.combustflame.2014.07.001.

[83] L. de Goey, T. Plessing, R. Hermanns, N. Peters, Analysis of the flame thickness of turbulent flamelets in the thin reaction zones regime, Proceedings of the Combustion Institute 30 (1) (2005) 859 – 866. doi:http://dx.doi.org/10.1016/j.proci.2004.08.016.

[84] M. Tanahashi, Y. Nada, N. Shiwaku, T. Miyauchi, Direct numerical simulations of turbulent premixed flames with realistic kinetic mechanisms (2007) 107–113.

[85] B. B. Mandelbrot, On the geometry of homogeneous turbulence, with stress on the fractal dimension of the iso-surfaces of scalars, Journal of Fluid Mechanics 72 (1975) 401–416. doi:http://dx.doi.org/10.1017/S0022112075003047.

[86] T. Miyauchi, M. Tanahashi, F. Gao, Fractal characteristics of turbulent diffusion flames, Combustion Science and Technology 96 (1-3) (1994) 135–154. doi:http://dx.doi.org/10.1080/00102209408935351.

[87] T. Poinsot, D. Veynante, S. Candel, Diagrams of premixed turbulent combustion based on direct simulation, Symposium (International) on Combustion 23 (1) (1991) 613 – 619. doi:http://dx.doi.org/10.1016/S0082-0784(06)80308-5.

[88] Ö. L. Gülder, G. J. Smallwood, Inner cutoff scale of flame surface wrinkling in turbulent premixed flames, Combustion and Flame 103 (1-2) (1995) 107 – 114. doi:http://dx.doi.org/10.1016/0010-2180(95)00073-F.

[89] B. B. Mandelbrot, The fractal geometry of nature, The American Mathematical Monthly 91 (9) (1984) 594–598.
URL `http://www.jstor.org/stable/2323761`

[90] G. Smallwood, Ö. L. Gülder, D. Snelling, B. Deschamps, I. Gokalp, Characterization of flame front surfaces in turbulent premixed methane/air combustion, Combustion and Flame 101 (4) (1995) 461 – 470. doi:http://dx.doi.org/10.1016/0010-2180(94)00226-I.

[91] J. Mantzaras, P. Felton, F. Bracco, Fractals and turbulent premixed engine flames, Combustion and Flame 77 (3-4) (1989) 295 – 310. doi:http://dx.doi.org/10.1016/0010-2180(89)90136-3.

[92] E. Cintosun, G. Smallwood, Ö. Gülder, Flame surface fractal characteristics in premixed turbulent combustion at high turbulence intensities, AIAA Journal 45 (11) (2007) 2785–2789. doi:http://dx.doi.org/10.2514/1.29533.

[93] C. Cohé, F. Halter, C. Chauveau, I. Gökalp, Ö. L. Gülder, Fractal characterisation of high-pressure and hydrogen-enriched CH_4-air turbulent premixed flames 31 (1) (2007) 1345–1352. doi:http://dx.doi.org/10.1016/j.proci.2006.07.181.

[94] I. Shepherd, R. Cheng, L. Talbot, Experimental criteria for the determination of fractal parameters of premixed turbulent flames, Experiments in Fluids 13 (6) (1992) 386–392. doi:http://dx.doi.org/10.1007/BF00223246.

[95] P. J. Goix, I. G. Shepherd, Lewis number effects on turbulent premixed flame structure, Combustion Science and Technology 91 (4-6) (1993) 191–206. doi:http://dx.doi.org/10.1080/00102209308907644.

[96] A. Gorgeon, I. Gokalp, A planar laser induced fluorescence study of turbulent flame kernel growth and fractal characteristics, Combustion Science and Technology 92 (4-6) (1993) 265–290. doi:http://dx.doi.org/10.1080/00102209308907675.

[97] H. Kobayashi, K. Seyama, H. Hagiwara, Y. Ogami, Burning velocity correlation of methane/air turbulent premixed flames at high pressure and high temperature, Proceedings of the Combustion Institute 30 (1) (2005) 827 – 834. doi:http://dx.doi.org/10.1016/j.proci.2004.08.098.

[98] W. L. Roberts, J. F. Driscoll, M. C. Drake, L. P. Goss, Images of the quenching of a flame by a vortex-to quantify regimes of turbulent combustion, Combustion and Flame 94 (1-2) (1993) 58 – 69. doi:http://dx.doi.org/10.1016/0010-2180(93)90019-Y.

[99] E. Weisstein, Box fractal, From MathWorld–A Wolfram Web Resource. URL `http://mathworld.wolfram.com/BoxFractal.html`

[100] K. Hiraoka, M. Shimura, Y. Naka, N. Fukushima, M. Tanahashi, T. Miyauchi, Fractal characteristics of hydrogen-air turbulent jet and V-shape premixed flames, TEDCONF2014 USB, Tokyo, Japan (2014) I123.

Appendix A

The detailed kinetic mechanism for hydrogen–air premixed flame

Table A.1: 12 reactive species [57].

NO.	Species
1	H_2
2	H
3	O_2
4	O
5	OH
6	HO_2
7	H_2O_2
8	H_2O
9	N
10	NO_2
11	NO
12	N_2

Table A.2: The elementary reaction mechanism [57].

	Reaction	A	β	E
1f	$H+O_2 \Longrightarrow OH+O$	2.00E+14	0	16800
1b	$OH+O \Longrightarrow H+O_2$	1.58E+09	0	690
2f	$H_2+O \Longrightarrow OH+H$	1.80E+10	1	8826
2b	$OH+H \Longrightarrow H_2+O$	8.00E+09	1	6760
3f	$H_2+OH \Longrightarrow H_2O+H$	1.17E+09	1.3	3626
3b	$H_2O+H \Longrightarrow H_2+OH$	5.09E+09	1.3	18588
4f	$OH+OH \Longrightarrow O+H_2O$	6.00E+08	1.3	0
4b	$H_2O+O \Longrightarrow OH+OH$	5.90E+09	1.3	17029
5	$H_2+O_2 \Longleftrightarrow OH+OH$	1.70E+14	0	47780
6	$H+O_2+M \Longleftrightarrow HO_2+M$	3.61E+17	-0.72	0
	$H_2O/18.6/@H_2/2.9/@N_2/1.3/$			
7	$OH+HO_2 \Longleftrightarrow H_2O+O$	7.50E+12	0	0
8	$H+HO_2 \Longleftrightarrow OH+OH$	1.40E+14	0	1073
9	$O+HO_2 \Longleftrightarrow O_2+OH$	1.40E+13	0	1073
10	$H+H+M \Longleftrightarrow H_2+M$	1.00E+18	-1	0
	$H_2O/0.0/@H_2/0.0/$			
11	$H+H+H_2 \Longleftrightarrow H_2+ H_2$	9.20E+16	-0.6	0
12	$H+H+H_2O \Longleftrightarrow H_2+H_2O$	6.00E+19	-1.25	0
13	$H+OH+M \Longleftrightarrow H_2O+M$	1.60E+22	-2	0
	$H_2O/5.0/$			
14	$H+O+M \Longleftrightarrow OH+M$	6.20E+16	-0.6	0
	$H_2O/5.0/$			
15	$O+O+M \Longleftrightarrow O_2+M$	1.89E+13	0	-1788
16	$H+HO_2 \Longleftrightarrow H_2+O_2$	1.25E+13	0	0
17	$HO_2+HO_2 \Longleftrightarrow H_2O_2+O_2$	2.00E+12	0	0
18	$H_2O_2+M \Longleftrightarrow OH+OH+M$	1.30E+17	0	45500
19	$H_2O_2+H \Longleftrightarrow HO_2+H_2$	1.60E+12	0	3800
20	$H_2O_2+OH \Longleftrightarrow H_2O+HO_2$	1.00E+13	0	1800
21	$N+NO \Longleftrightarrow N_2+O$	3.27E+12	0.3	0
22	$N+O_2 \Longleftrightarrow NO+O$	6.40E+09	1	6280
23	$N+OH \Longleftrightarrow NO+H$	3.08E+13	0	0
24	$HO_2+NO \Longleftrightarrow NO_2+OH$	2.11E+12	0	-479
25	$NO_2+H \Longleftrightarrow NO+OH$	3.50E+14	0	1500
26	$NO_2+O \Longleftrightarrow NO+O_2$	1.00E+13	0	600
27	$NO_2+M \Longleftrightarrow NO+O+M$	1.10E+16	0	66000

(A: frequency factor, β: pre-exponential temperature exponent, E: activation energy)

Appendix B

The detailed kinetic mechanism for methane–air premixed flame

Table B.1: 53 reactive species from GRI-Mech 3.0 kinetic mechanism [52].

NO.	Species	NO.	Species
1	H_2	28	HCCO
2	H	29	CH_2CO
3	O	30	HCCOH
4	O_2	31	N
5	OH	32	NH
6	H_2O	33	NH_2
7	HO_2	34	NH_3
8	H_2O_2	35	NNH
9	C	36	NO
10	CH	37	NO_2
11	CH_2	38	N_2O
12	CH_2(S)	39	HNO
13	CH_3	40	CN
14	CH_4	41	HCN
15	CO	42	H_2CN
16	CO_2	43	HCNN
17	HCO	44	HCNO
20	CH_3O	45	HOCN
18	CH_2O	46	HNCO
19	CH_2OH	47	NCO
21	CH_3OH	48	AR
22	C_2H	49	C_3H_7
23	C_2H_2	50	C_3H_8
24	C_2H_3	51	CH_2CHO
25	C_2H_4	52	CH_3CHO
26	C_2H_5	53	N_2
27	C_2H_6		

Table B.2: 325 elementary reactions from GRI-Mech 3.0 kinetic mechanism [52].

	Reaction	A	β	E
1	$2O+M^a \Longleftrightarrow O_2+M^a$	1.20E+17	-1	0
2	$O+H+M^b \Longleftrightarrow OH+M^b$	5.00E+17	-1	0
3	$O+H_2 \Longleftrightarrow H+OH$	3.87E+04	2.7	6260
4	$O+HO_2 \Longleftrightarrow OH+O_2$	2.00E+13	0	0
5	$O+H_2O_2 \Longleftrightarrow OH+HO_2$	9.63E+06	2	4000
6	$O+CH \Longleftrightarrow H+CO$	5.70E+13	0	0
7	$O+CH_2 \Longleftrightarrow H+HCO$	8.00E+13	0	0
8	$O+CH_2(S) \Longleftrightarrow H_2+CO$	1.50E+13	0	0
9	$O+CH_2(S) \Longleftrightarrow H+HCO$	1.50E+13	0	0
10	$O+CH_3 \Longleftrightarrow H+CH_2O$	5.06E+13	0	0
11	$O+CH_4 \Longleftrightarrow OH+CH_3$	1.02E+09	1.5	8600
12	$O+CO\ (+M^c) \Longleftrightarrow CO_2(+M^c)$	1.80E+10	0	2385
	Low pressure limit: 6.02E+14 0.00 3000			
13	$O+HCO \Longleftrightarrow OH+CO$	3.00E+13	0	0
14	$O+HCO \Longleftrightarrow H+CO_2$	3.00E+13	0	0
15	$O+CH_2O \Longleftrightarrow OH+HCO$	3.90E+13	0	3540
16	$O+CH_2OH \Longleftrightarrow OH+CH_2O$	1.00E+13	0	0
17	$O+CH_3O \Longleftrightarrow OH+CH_2O$	1.00E+13	0	0
18	$O+CH_3OH \Longleftrightarrow OH+CH_2OH$	3.88E+05	2.5	3100
19	$O+CH_3OH \Longleftrightarrow OH+CH_3O$	1.30E+05	2.5	5000
20	$O+C_2H \Longleftrightarrow CH+CO$	5.00E+13	0	0
21	$O+C_2H_2 \Longleftrightarrow H+HCCO$	1.35E+07	2	1900
22	$O+C_2H_2 \Longleftrightarrow OH+C_2H$	4.60E+19	-1.4	28950
23	$O+C_2H_2 \Longleftrightarrow CO+CH_2$	6.94E+06	2	1900
24	$O+C_2H_3 \Longleftrightarrow H+CH_2CO$	3.00E+13	0	0
25	$O+C_2H_4 \Longleftrightarrow CH_3+HCO$	1.25E+07	1.8	220
26	$O+C_2H_5 \Longleftrightarrow CH_3+CH_2O$	2.24E+13	0	0
27	$O+C_2H_6 \Longleftrightarrow OH+C_2H_5$	8.98E+07	1.9	5690
28	$O+HCCO \Longleftrightarrow H+2CO$	1.00E+14	0	0
29	$O+CH_2CO \Longleftrightarrow OH+HCCO$	1.00E+13	0	8000
30	$O+CH_2CO \Longleftrightarrow CH_2+CO_2$	1.75E+12	0	1350
31	$O_2+CO \Longleftrightarrow O+CO_2$	2.50E+12	0	47800
32	$O_2+CH_2O \Longleftrightarrow HO_2+HCO$	1.00E+14	0	40000
33	$H+O_2+M^d \Longleftrightarrow HO_2+M^d$	2.80E+18	-0.9	0
34	$H+2O_2 \Longleftrightarrow HO_2+O_2$	2.08E+19	-1.2	0
35	$H+O_2+H_2O \Longleftrightarrow HO_2+H_2O$	1.13E+19	-0.8	0
36	$H+O_2+N_2 \Longleftrightarrow HO_2+N_2$	2.60E+19	-1.2	0
37	$H+O_2+AR \Longleftrightarrow HO_2+AR$	7.00E+17	-0.8	0
38	$H+O_2 \Longleftrightarrow O+OH$	2.65E+16	-0.7	17041
39	$2H+M^e \Longleftrightarrow H_2+M^e$	1.00E+18	-1	0
40	$2H+H_2 \Longleftrightarrow 2H_2$	9.00E+16	-0.6	0

	Reaction	A	β	E
41	$2H+H_2O \Longleftrightarrow H_2+H_2O$	6.00E+19	-1.3	0
42	$2H+CO_2 \Longleftrightarrow H_2+CO_2$	5.50E+20	-2	0
43	$H+OH+M^f \Longleftrightarrow H_2O+M^f$	2.20E+22	-2	0
44	$H+HO_2 \Longleftrightarrow O+H_2O$	3.97E+12	0	671
45	$H+HO_2 \Longleftrightarrow O_2+H_2$	4.48E+13	0	1068
46	$H+HO_2 \Longleftrightarrow 2OH$	8.40E+13	0	635
47	$H+H_2O_2 \Longleftrightarrow HO_2+H_2$	1.21E+07	2	5200
48	$H+H_2O_2 \Longleftrightarrow OH+H_2O$	1.00E+13	0	3600
49	$H+CH \Longleftrightarrow C+H_2$	1.65E+14	0	0
50	$H+CH_2(+M^b) \Longleftrightarrow CH_3(+M^b)$	6.00E+14	0	0
	Low pressure limit: 1.04E+26 -2.76 1600			
	Troe parameters: α= 5.62E-01 T^{***}= 91 T^{*}= 5836 T^{**}= 8552			
51	$H+CH_2(S) \Longleftrightarrow CH+H_2$	3.00E+13	0	0
52	$H+CH_3(+M^g) \Longleftrightarrow CH_4(+M^g)$	1.39E+16	-0.5	536
	Low pressure limit: 2.62E+33 -4.76 2440			
	Troe parameters: α= 7.83E-01 T^{***}= 74 T^{*}= 2941 T^{**}= 6964			
53	$H+CH_4 \Longleftrightarrow CH_3+H_2$	6.60E+08	1.6	10840
54	$H+HCO\ (+M^b) \Longleftrightarrow CH_2O(+M^b)$	1.09E+12	0.5	-260
	Low pressure limit: 2.47E+24 -2.57 425			
	Troe parameters: α= 7.82E-01 T^{***}= 271 T^{*}= 2755 T^{**}= 6570			
	Troe parameters: α=7.824E-01 T^{***}=271 T^{*}=2755 T^{**}=6570			
55	$H+HCO \Longleftrightarrow H_2+CO$	7.34E+13	0	0
56	$H+CH_2O(+M^h) \Longleftrightarrow CH_2OH(+M^h)$	5.40E+11	0.5	3600
	Low pressure limit: 1.27E+32 -4.82 6530			
	Troe parameters: α= 7.19E-01 T^{***}= 103 T^{*}= 1291 T^{**}= 4160			
57	$H+CH_2O(+M^h) \Longleftrightarrow CH_3O(+M^h)$	5.40E+11	0.5	2600
	Low pressure limit: 2.20E+30 -4.80 5560			
	Troe parameters: α= 7.58E-01 T^{***}= 94 T^{*}= 1555 T^{**}= 4200			
58	$H+CH_2O \Longleftrightarrow HCO+H_2$	5.74E+07	1.9	2742
59	$H+CH_2OH(+M^h) \Longleftrightarrow CH_3OH(+M^h)$	1.06E+12	0.5	86
	Low pressure limit: 4.36E+31 -4.65 5080			
	Troe parameters: α= 6.00E-01 T^{***}= 100 T^{*}= 90000 T^{**}= 10000			
60	$H+CH_2OH \Longleftrightarrow H_2+CH_2O$	2.00E+13	0	0
61	$H+CH_2OH \Longleftrightarrow OH+CH_3$	1.65E+11	0.7	-284
62	$H+CH_2OH \Longleftrightarrow CH_2(S)+H_2O$	3.28E+13	-0.1	610
63	$H+CH_3O(+M^h) \Longleftrightarrow CH_3OH(+M^h)$	2.43E+12	0.5	50
	Low pressure limit: 4.66E+41 -7.44 14080			
	Troe parameters: α= 7.00E-01 T^{***}= 100 T^{*}= 90000 T^{**}= 10000			
64	$H+CH_3O \Longleftrightarrow H+CH_2OH$	4.15E+07	1.6	1924
65	$H+CH_3O \Longleftrightarrow H_2+CH_2O$	2.00E+13	0	0
66	$H+CH_3O \Longleftrightarrow OH+CH_3$	1.50E+12	0.5	-110
67	$H+CH_3O \Longleftrightarrow CH_2(S)+H_2O$	2.62E+14	-0.2	1070
68	$H+CH_3OH \Longleftrightarrow CH_2OH+H_2$	1.70E+07	2.1	4870
69	$H+CH_3OH \Longleftrightarrow CH_3O+H_2$	4.20E+06	2.1	4870

	Reaction	A	β	E
70	$H+C_2H(+M^b) \Longleftrightarrow C_2H_2(+M^b)$	1.00E+17	-1	0
	Low pressure limit: 3.75E+33 -4.80 1900			
	Troe parameters: α= 6.46E-01 T^{***}= 132 T^{*}= 1315 T^{**}= 5566			
71	$H+C_2H_2(+M^b) \Longleftrightarrow C_2H_3(+M^b)$	5.60E+12	0	2400
	Low pressure limit: 3.80E+40 -7.27 7220			
	Troe parameters: α= 7.51E-01 T^{***}= 99 T^{*}= 1302 T^{**}= 4167			
72	$H+C_2H_3(+M^b) \Longleftrightarrow C_2H_4(+M^b)$	6.08E+12	0.3	280
	Low pressure limit: 1.40E+30 -3.86 3320			
	Troe parameters: α= 7.82E-01 T^{***}= 208 T^{*}= 2663 T^{**}= 6095			
73	$H+C_2H_3 \Longleftrightarrow H_2+C_2H_2$	3.00E+13	0	0
74	$H+C_2H_4(+M^b) \Longleftrightarrow C_2H_5(+M^b)$	5.40E+11	0.5	1820
	Low pressure limit: 6.00E+41 -7.62 6970			
	Troe parameters: α= 9.75E-01 T^{***}= 210 T^{*}= 984 T^{**}= 4374			
75	$H+C_2H_4 \Longleftrightarrow C_2H_3+H_2$	1.33E+06	2.5	12240
76	$H+C_2H_5(+M^b) \Longleftrightarrow C_2H_6(+M^b)$	5.21E+17	-1	1580
	Low pressure limit: 1.99E+41 -7.08 6685			
	Troe parameters: α= 8.42E-01 T^{***}= 125 T^{*}= 2219 T^{**}= 6882			
77	$H+C_2H_5 \Longleftrightarrow H_2+C_2H_4$	2.00E+12	0	0
78	$H+C_2H_6 \Longleftrightarrow C_2H_5+H_2$	1.15E+08	1.9	7530
79	$H+HCCO \Longleftrightarrow CH_2(S)+CO$	1.00E+14	0	0
80	$H+CH_2CO \Longleftrightarrow HCCO+H_2$	5.00E+13	0	8000
81	$H+CH_2CO \Longleftrightarrow CH_3+CO$	1.13E+13	0	3428
82	$H+HCCOH \Longleftrightarrow H+CH_2CO$	1.00E+13	0	0
83	$H_2+CO\ (+M^b) \Longleftrightarrow CH_2O(+M^b)$	4.30E+07	1.5	79600
	Low pressure limit: 5.07E+27 -3.42 84350			
	Troe parameters: α= 9.32E-01 T^{***}= 197 T^{*}= 1540 T^{**}= 10300			
84	$OH+H_2 \Longleftrightarrow H+H_2O$	2.16E+08	1.5	3430
85	$2OH\ (+M^b) \Longleftrightarrow H_2O_2(+M^b)$	7.40E+13	-0.4	0
	Low pressure limit: 2.30E+18 -0.90 -1700			
	Troe parameters: α= 7.35E-01 T^{***}= 94 T^{*}= 1756 T^{**}= 5182			
86	$2OH \Longleftrightarrow O+H_2O$	3.57E+04	2.4	-2110
87	$OH+HO_2 \Longleftrightarrow O_2+H_2O$	1.45E+13	0	-500
88	$OH+H_2O_2 \Longleftrightarrow HO_2+H_2O$	2.00E+12	0	427
89	$OH+H_2O_2 \Longleftrightarrow HO_2+H_2O$	1.70E+18	0	29410
90	$OH+C \Longleftrightarrow H+CO$	5.00E+13	0	0
91	$OH+CH \Longleftrightarrow H+HCO$	3.00E+13	0	0
92	$OH+CH_2 \Longleftrightarrow H+CH_2O$	2.00E+13	0	0
93	$OH+CH_2 \Longleftrightarrow CH+H_2O$	1.13E+07	2	3000
94	$OH+CH_2(S) \Longleftrightarrow H+CH_2O$	3.00E+13	0	0
95	$OH+CH_3(+M^h) \Longleftrightarrow CH_3OH(+M^h)$	2.79E+18	-1.4	1330
	Low pressure limit: 4.00E+36 -5.92 3140			
	Troe parameters: α= 4.12E-01 T^{***}= 195 T^{*}= 5900 T^{**}= 6394			
96	$OH+CH_3 \Longleftrightarrow CH_2+H_2O$	5.60E+07	1.6	5420
97	$OH+CH_3 \Longleftrightarrow CH_2(S)+H_2O$	6.44E+17	-1.3	1417

	Reaction	A	β	E
98	$OH+CH_4 \Longleftrightarrow CH_3+H_2O$	1.00E+08	1.6	3120
99	$OH+CO \Longleftrightarrow H+CO_2$	4.76E+07	1.2	70
100	$OH+HCO \Longleftrightarrow H_2O+CO$	5.00E+13	0	0
101	$OH+CH_2O \Longleftrightarrow HCO+H_2O$	3.43E+09	1.2	-447
102	$OH+CH_2OH \Longleftrightarrow H_2O+CH_2O$	5.00E+12	0	0
103	$OH+CH_3O \Longleftrightarrow H_2O+CH_2O$	5.00E+12	0	0
104	$OH+CH_3OH \Longleftrightarrow CH_2OH+H_2O$	1.44E+06	2	-840
105	$OH+CH_3OH \Longleftrightarrow CH_3O+H_2O$	6.30E+06	2	1500
106	$OH+C_2H \Longleftrightarrow H+HCCO$	2.00E+13	0	0
107	$OH+C_2H_2 \Longleftrightarrow H+CH_2CO$	2.18E-04	4.5	-1000
108	$OH+C_2H_2 \Longleftrightarrow H+HCCOH$	5.04E+05	2.3	13500
109	$OH+C_2H_2 \Longleftrightarrow C_2H+H_2O$	3.37E+07	2	14000
110	$OH+C_2H_2 \Longleftrightarrow CH_3+CO$	4.83E-04	4	-2000
111	$OH+C_2H_3 \Longleftrightarrow H_2O+C_2H_2$	5.00E+12	0	0
112	$OH+C_2H_4 \Longleftrightarrow C_2H_3+H_2O$	3.60E+06	2	2500
113	$OH+C_2H_6 \Longleftrightarrow C_2H_5+H_2O$	3.54E+06	2.1	870
114	$OH+CH_2CO \Longleftrightarrow HCCO+H_2O$	7.50E+12	0	2000
115	$2HO_2 \Longleftrightarrow O_2+H_2O_2$	1.30E+11	0	-1630
116	$2HO_2 \Longleftrightarrow O_2+H_2O_2$	4.20E+14	0	12000
117	$HO_2+CH_2 \Longleftrightarrow OH+CH_2O$	2.00E+13	0	0
118	$HO_2+CH_3 \Longleftrightarrow O_2+CH_4$	1.00E+12	0	0
119	$HO_2+CH_3 \Longleftrightarrow OH+CH_3O$	3.78E+13	0	0
120	$HO_2+CO \Longleftrightarrow OH+CO_2$	1.50E+14	0	23600
121	$HO_2+CH_2O \Longleftrightarrow HCO+H_2O_2$	5.60E+06	2	12000
122	$C+O_2 \Longleftrightarrow O+CO$	5.80E+13	0	576
123	$C+CH_2 \Longleftrightarrow H+C_2H$	5.00E+13	0	0
124	$C+CH_3 \Longleftrightarrow H+C_2H_2$	5.00E+13	0	0
125	$CH+O_2 \Longleftrightarrow O+HCO$	6.71E+13	0	0
126	$CH+H_2 \Longleftrightarrow H+CH_2$	1.08E+14	0	3110
127	$CH+H_2O \Longleftrightarrow H+CH_2O$	5.71E+12	0	-755
128	$CH+CH_2 \Longleftrightarrow H+C_2H_2$	4.00E+13	0	0
129	$CH+CH_3 \Longleftrightarrow H+C_2H_3$	3.00E+13	0	0
130	$CH+CH_4 \Longleftrightarrow H+C_2H_4$	6.00E+13	0	0
131	$CH+CO\ (+M^b) \Longleftrightarrow HCCO@(+M^b)$	5.00E+13	0	0
	Low pressure limit: 2.69E+28 -3.74 1936			
	Troe parameters: α= 5.76E-01 T^{***}= 237 T^{*}= 1652 T^{**}= 5069			
132	$CH+CO_2 \Longleftrightarrow HCO+CO$	1.90E+14	0	15792
133	$CH+CH_2O \Longleftrightarrow H+CH_2CO$	9.46E+13	0	-515
134	$CH+HCCO \Longleftrightarrow CO+C_2H_2$	5.00E+13	0	0
135	$CH_2+O_2 \Longleftrightarrow OH+H+CO$	5.00E+12	0	1500
136	$CH_2+H_2 \Longleftrightarrow H+CH_3$	5.00E+05	2	7230
137	$2CH_2 \Longleftrightarrow H_2+C_2H_2$	1.60E+15	0	11944
138	$CH_2+CH_3 \Longleftrightarrow H+C_2H_4$	4.00E+13	0	0
139	$CH_2+CH_4 \Longleftrightarrow 2CH_3$	2.46E+06	2	8270

	Reaction	A	β	E
140	CH_2+CO (+M^b) $\Longleftrightarrow$ CH_2CO(+M^b)	8.10E+11	0.5	4510
	Low pressure limit: 2.69E+33 -5.11 7095			
	Troe parameters: α= 5.91E-01 T^{***}= 275 T^{*}= 1226 T^{**}= 5185			
141	CH_2+HCCO $\Longleftrightarrow$ C_2H_3+CO	3.00E+13	0	0
142	CH_2(S)+$N_2$$\Longleftrightarrow$ CH_2+N_2	1.50E+13	0	600
143	CH_2(S)+AR $\Longleftrightarrow$ CH_2+AR	9.00E+12	0	600
144	CH_2(S)+$O_2$$\Longleftrightarrow$ H+OH+CO	2.80E+13	0	0
145	CH_2(S)+$O_2$$\Longleftrightarrow$ CO+H_2O	1.20E+13	0	0
146	CH_2(S)+$H_2$$\Longleftrightarrow$ CH_3+H	7.00E+13	0	0
147	CH_2(S)+H_2O(+M^h) $\Longleftrightarrow$ CH_3OH(+M^h)	4.82E+17	-1.2	1145
	Low pressure limit: 1.88E+38 -6.36 5040			
	Troe parameters: α= 6.03E-01 T^{***}= 208 T^{*}= 3922 T^{**}= 10180			
148	CH_2(S)+$H_2O$$\Longleftrightarrow$ CH_2+H_2O	3.00E+13	0	0
149	CH_2(S)+$CH_3$$\Longleftrightarrow$ H+C_2H_4	1.20E+13	0	-570
150	CH_2(S)+$CH_4$$\Longleftrightarrow$ 2CH_3	1.60E+13	0	-570
151	CH_2(S)+CO $\Longleftrightarrow$ CH_2+CO	9.00E+12	0	0
152	CH_2(S)+$CO_2$$\Longleftrightarrow$ CH_2+CO_2	7.00E+12	0	0
153	CH_2(S)+$CO_2$$\Longleftrightarrow$ CO+CH_2O	1.40E+13	0	0
154	CH_2(S)+$C_2H_6$$\Longleftrightarrow$ CH_3+C_2H_5	4.00E+13	0	-550
155	CH_3+$O_2$$\Longleftrightarrow$ O+CH_3O	3.56E+13	0	30480
156	CH_3+$O_2$$\Longleftrightarrow$ OH+CH_2O	2.31E+12	0	20315
157	CH_3+$H_2O_2$$\Longleftrightarrow$ HO_2+CH_4	2.45E+04	2.5	5180
158	2CH_3(+M^b) $\Longleftrightarrow$ C_2H_6(+M^b)	6.77E+16	-1.2	654
	Low pressure limit: 3.40E+41 -7.03 2762			
	Troe parameters: α= 6.19E-01 T^{***}= 73 T^{*}= 1180 T^{**}= 9999			
159	2$CH_3$$\Longleftrightarrow$ H+C_2H_5	6.84E+12	0.1	10600
160	CH_3+HCO $\Longleftrightarrow$ CH_4+CO	2.65E+13	0	0
161	CH_3+$CH_2O$$\Longleftrightarrow$ HCO+CH_4	3.32E+03	2.8	5860
162	CH_3+$CH_3OH$$\Longleftrightarrow$ CH_2OH+CH_4	3.00E+07	1.5	9940
163	CH_3+$CH_3OH$$\Longleftrightarrow$ CH_3O+CH_4	1.00E+07	1.5	9940
164	CH_3+$C_2H_4$$\Longleftrightarrow$ C_2H_3+CH_4	2.27E+05	2	9200
165	CH_3+$C_2H_6$$\Longleftrightarrow$ C_2H_5+CH_4	6.14E+06	1.7	10450
166	HCO+$H_2O$$\Longleftrightarrow$ H+CO+HtwoO	1.50E+18	-1	17000
167	HCO+M^i $\Longleftrightarrow$ H+CO+M^i	1.87E+17	-1	17000
168	HCO+$O_2$$\Longleftrightarrow$ HO_2+CO	1.35E+13	0	400
169	CH_2OH+$O_2$$\Longleftrightarrow$ HO_2+CH_2O	1.80E+13	0	900
170	CH_3O+$O_2$$\Longleftrightarrow$ HO_2+CH_2O	4.28E-13	7.6	-3530
171	C_2H+$O_2$$\Longleftrightarrow$ HCO+CO	1.00E+13	0	-755
172	C_2H+$H_2$$\Longleftrightarrow$ H+C_2H_2	5.68E+10	0.9	1993
173	C_2H_3+$O_2$$\Longleftrightarrow$ HCO+CH_2O	4.58E+16	-1.4	1015

	Reaction	A	β	E
174	$C_2H_4(+M^b) \Longleftrightarrow H_2+C_2H_2(+M^b)$	8.00E+12	0.4	86770
	Low pressure limit: 1.58E+51 -9.30 97800			
	Troe parameters: α= 7.35E-01 T^{***}= 180 T^{*}= 1035 T^{**}= 5417			
175	$C_2H_5+O_2 \Longleftrightarrow HO_2+C_2H_4$	8.40E+11	0	3875
176	$HCCO+O_2 \Longleftrightarrow OH+2CO$	3.20E+12	0	854
177	$2HCCO \Longleftrightarrow 2CO+C_2H_2$	1.00E+13	0	0
178	$N+NO \Longleftrightarrow N_2+O$	2.70E+13	0	355
179	$N+O_2 \Longleftrightarrow NO+O$	9.00E+09	1	6500
180	$N+OH \Longleftrightarrow NO+H$	3.36E+13	0	385
181	$N_2O+O \Longleftrightarrow N_2+O_2$	1.40E+12	0	10810
182	$N_2O+O \Longleftrightarrow 2NO$	2.90E+13	0	23150
183	$N_2O+H \Longleftrightarrow N_2+OH$	3.87E+14	0	18880
184	$N_2O+OH \Longleftrightarrow N_2+HO_2$	2.00E+12	0	21060
185	$N_2O(+M^j) \Longleftrightarrow N_2+O\ (+M^j)$	7.91E+10	0	56020
	Low pressure limit: 6.37E+14 0.00 56640			
186	$HO_2+NO \Longleftrightarrow NO_2+OH$	2.11E+12	0	-480
187	$NO+O+M^b \Longleftrightarrow NO_2+M^b$	1.06E+20	-1.4	0
188	$NO_2+O \Longleftrightarrow NO+O_2$	3.90E+12	0	-240
189	$NO_2+H \Longleftrightarrow NO+OH$	1.32E+14	0	360
190	$NH+O \Longleftrightarrow NO+H$	4.00E+13	0	0
191	$NH+H \Longleftrightarrow N+H_2$	3.20E+13	0	330
192	$NH+OH \Longleftrightarrow HNO+H$	2.00E+13	0	0
193	$NH+OH \Longleftrightarrow N+H_2O$	2.00E+09	1.2	0
194	$NH+O_2 \Longleftrightarrow HNO+O$	4.61E+05	2	6500
195	$NH+O_2 \Longleftrightarrow NO+OH$	1.28E+06	1.5	100
196	$NH+N \Longleftrightarrow N_2+H$	1.50E+13	0	0
197	$NH+H_2O \Longleftrightarrow HNO+H_2$	2.00E+13	0	13850
198	$NH+NO \Longleftrightarrow N_2+OH$	2.16E+13	-0.2	0
199	$NH+NO \Longleftrightarrow N_2O+H$	3.65E+14	-0.5	0
200	$NH_2+O \Longleftrightarrow OH+NH$	3.00E+12	0	0
201	$NH_2+O \Longleftrightarrow H+HNO$	3.90E+13	0	0
202	$NH_2+H \Longleftrightarrow NH+H_2$	4.00E+13	0	3650
203	$NH_2+OH \Longleftrightarrow NH+H_2O$	9.00E+07	1.5	-460
204	$NNH \Longleftrightarrow N_2+H$	3.30E+08	0	0
205	$NNH+M^b \Longleftrightarrow N_2+H+M^b$	1.30E+14	-0.1	4980
206	$NNH+O_2 \Longleftrightarrow HO_2+N_2$	5.00E+12	0	0
207	$NNH+O \Longleftrightarrow OH+N_2$	2.50E+13	0	0
208	$NNH+O \Longleftrightarrow NH+NO$	7.00E+13	0	0
209	$NNH+H \Longleftrightarrow H_2+N_2$	5.00E+13	0	0
210	$NNH+OH \Longleftrightarrow H_2O+N_2$	2.00E+13	0	0
211	$NNH+CH_3 \Longleftrightarrow CH_4+N_2$	2.50E+13	0	0
212	$H+NO+M^b \Longleftrightarrow HNO+M^b$	4.48E+19	-1.3	740
213	$HNO+O \Longleftrightarrow NO+OH$	2.50E+13	0	0
214	$HNO+H \Longleftrightarrow H_2+NO$	9.00E+11	0.7	660

	Reaction	A	β	E
215	HNO+OH $\Longleftrightarrow$ NO+H_2O	1.30E+07	1.9	-950
216	HNO+$O_2\Longleftrightarrow$ HO_2+NO	1.00E+13	0	13000
217	CN+O $\Longleftrightarrow$ CO+N	7.70E+13	0	0
218	CN+OH $\Longleftrightarrow$ NCO+H	4.00E+13	0	0
219	CN+$H_2O\Longleftrightarrow$ HCN+OH	8.00E+12	0	7460
220	CN+$O_2\Longleftrightarrow$ NCO+O	6.14E+12	0	-440
221	CN+$H_2\Longleftrightarrow$ HCN+H	2.95E+05	2.5	2240
222	NCO+O $\Longleftrightarrow$ NO+CO	2.35E+13	0	0
223	NCO+H $\Longleftrightarrow$ NH+CO	5.40E+13	0	0
224	NCO+OH $\Longleftrightarrow$ NO+H+CO	2.50E+12	0	0
225	NCO+N $\Longleftrightarrow$ N_2+CO	2.00E+13	0	0
226	NCO+$O_2\Longleftrightarrow$ NO+CO_2	2.00E+12	0	20000
227	NCO+M^b $\Longleftrightarrow$ N+CO+M^b	3.10E+14	0	54050
228	NCO+NO $\Longleftrightarrow$ N_2O+CO	1.90E+17	-1.5	740
229	NCO+NO $\Longleftrightarrow$ N_2+CO_2	3.80E+18	-2	800
230	HCN+M^b $\Longleftrightarrow$ H+CN+M^b	1.04E+29	-3.3	126600
231	HCN+O $\Longleftrightarrow$ NCO+H	2.03E+04	2.6	4980
232	HCN+O $\Longleftrightarrow$ NH+CO	5.07E+03	2.6	4980
233	HCN+O $\Longleftrightarrow$ CN+OH	3.91E+09	1.6	26600
234	HCN+OH $\Longleftrightarrow$ HOCN+H	1.10E+06	2	13370
235	HCN+OH $\Longleftrightarrow$ HNCO+H	4.40E+03	2.3	6400
236	HCN+OH $\Longleftrightarrow$ NH_2+CO	1.60E+02	2.6	9000
237	H+HCN (+M^b) $\Longleftrightarrow$ H_2CN(+M^b)	3.30E+13	0	0
	Low pressure limit: 1.40E+26 -3.40 1900			
238	H_2CN+N $\Longleftrightarrow$ N_2+CH_2	6.00E+13	0	400
239	C+$N_2\Longleftrightarrow$ CN+N	6.30E+13	0	46020
240	CH+$N_2\Longleftrightarrow$ HCN+N	3.12E+09	0.9	20130
241	CH+N_2(+M^k) $\Longleftrightarrow$ HCNN (+M^k)	3.10E+12	0.2	0
	Low pressure limit: 1.30E+25 -3.16 740			
	Troe parameters: α= 6.67E-01 T^{***}= 235 T^{*}= 2117 T^{**}= 4536			
242	CH_2+$N_2\Longleftrightarrow$ HCN+NH	1.00E+13	0	74000
243	CH_2(S)+$N_2\Longleftrightarrow$ NH+HCN	1.00E+11	0	65000
244	C+NO $\Longleftrightarrow$ CN+O	1.90E+13	0	0
245	C+NO $\Longleftrightarrow$ CO+N	2.90E+13	0	0
246	CH+NO $\Longleftrightarrow$ HCN+O	4.10E+13	0	0
247	CH+NO $\Longleftrightarrow$ H+NCO	1.62E+13	0	0
248	CH+NO $\Longleftrightarrow$ N+HCO	2.46E+13	0	0
249	CH_2+NO $\Longleftrightarrow$ H+HNCO	3.10E+17	-1.4	1270
250	CH_2+NO $\Longleftrightarrow$ OH+HCN	2.90E+14	-0.7	760
251	CH_2+NO $\Longleftrightarrow$ H+HCNO	3.80E+13	-0.4	580
252	CH_2(S)+NO $\Longleftrightarrow$ H+HNCO	3.10E+17	-1.4	1270
253	CH_2(S)+NO $\Longleftrightarrow$ OH+HCN	2.90E+14	-0.7	760
254	CH_2(S)+NO $\Longleftrightarrow$ H+HCNO	3.80E+13	-0.4	580
255	CH_3+NO $\Longleftrightarrow$ HCN+H_2O	9.60E+13	0	28800

	Reaction	A	β	E
256	CH_3+NO $\Longleftrightarrow$ H_2CN+OH	1.00E+12	0	21750
257	HCNN+O $\Longleftrightarrow$ CO+H+N_2	2.20E+13	0	0
258	HCNN+O $\Longleftrightarrow$ HCN+NO	2.00E+12	0	0
259	HCNN+$O_2$$\Longleftrightarrow$ O+HCO+N_2	1.20E+13	0	0
260	HCNN+OH $\Longleftrightarrow$ H+HCO+N_2	1.20E+13	0	0
261	HCNN+H $\Longleftrightarrow$ CH_2+N_2	1.00E+14	0	0
262	HNCO+O $\Longleftrightarrow$ NH+CO_2	9.80E+07	1.4	8500
263	HNCO+O $\Longleftrightarrow$ HNO+CO	1.50E+08	1.6	44000
264	HNCO+O $\Longleftrightarrow$ NCO+OH	2.20E+06	2.1	11400
265	HNCO+H $\Longleftrightarrow$ NH_2+CO	2.25E+07	1.7	3800
266	HNCO+H $\Longleftrightarrow$ H_2+NCO	1.05E+05	2.5	13300
267	HNCO+OH $\Longleftrightarrow$ NCO+H_2O	3.30E+07	1.5	3600
268	HNCO+OH $\Longleftrightarrow$ NH_2+CO_2	3.30E+06	1.5	3600
269	HNCO+M^b $\Longleftrightarrow$ NH+CO+M^b	1.18E+16	0	84720
270	HCNO+H $\Longleftrightarrow$ H+HNCO	2.10E+15	-0.7	2850
271	HCNO+H $\Longleftrightarrow$ OH+HCN	2.70E+11	0.2	2120
272	HCNO+H $\Longleftrightarrow$ NH_2+CO	1.70E+14	-0.8	2890
273	HOCN+H $\Longleftrightarrow$ H+HNCO	2.00E+07	2	2000
274	HCCO+NO $\Longleftrightarrow$ HCNO+CO	9.00E+12	0	0
275	CH_3+N $\Longleftrightarrow$ H_2CN+H	6.10E+14	-0.3	290
276	CH_3+N $\Longleftrightarrow$ HCN+H_2	3.70E+12	0.2	-90
277	NH_3+H $\Longleftrightarrow$ NH_2+H_2	5.40E+05	2.4	9915
278	NH_3+OH $\Longleftrightarrow$ NH_2+H_2O	5.00E+07	1.6	955
279	NH_3+O $\Longleftrightarrow$ NH_2+OH	9.40E+06	1.9	6460
280	NH+$CO_2$$\Longleftrightarrow$ HNO+CO	1.00E+13	0	14350
281	CN+$NO_2$$\Longleftrightarrow$ NCO+NO	6.16E+15	-0.8	345
282	NCO+$NO_2$$\Longleftrightarrow$ N_2O+CO_2	3.25E+12	0	-705
283	N+$CO_2$$\Longleftrightarrow$ NO+CO	3.00E+12	0	11300
284	O+$CH_3$$\Longrightarrow$ H+H_2+CO	3.37E+13	0	0
285	O+$C_2H_4$$\Longleftrightarrow$ H+CH_2CHO	6.70E+06	1.8	220
286	O+$C_2H_5$$\Longleftrightarrow$ H+CH_3CHO	1.10E+14	0	0
287	OH+$HO_2$$\Longleftrightarrow$ O_2+H_2O	5.00E+15	0	17330
288	OH+$CH_3$$\Longrightarrow$ H_2+CH_2O	8.00E+09	0.5	-1755
289	CH+H_2(+M^b) $\Longleftrightarrow$ CH_3(+M^b)	1.97E+12	0.4	-370
	Low pressure limit: 4.82E+25 -2.80 590			
	Troe parameters: α= 5.78E-01 T^{***}= 122 T^{*}= 2535 T^{**}= 9365			
290	CH_2+$O_2$$\Longrightarrow$ 2H+CO_2	5.80E+12	0	1500
291	CH_2+$O_2$$\Longleftrightarrow$ O+CH_2O	2.40E+12	0	1500
292	CH_2+$CH_2$$\Longrightarrow$ 2H+C_2H_2	2.00E+14	0	10989
293	CH_2(S)+$H_2O$$\Longrightarrow$ H_2+CH_2O	6.82E+10	0.3	-935
294	C_2H_3+$O_2$$\Longleftrightarrow$ O+CH_2CHO	3.03E+11	0.3	11
295	C_2H_3+$O_2$$\Longleftrightarrow$ HO_2+C_2H_2	1.34E+06	1.6	-384
296	O+CH_3CHO$\Longleftrightarrow$ OH+CH_2CHO	2.92E+12	0	1808
297	O+CH_3CHO$\Longrightarrow$ OH+CH_3+CO	2.92E+12	0	1808

	Reaction	A	β	E
298	O_2+$CH_3CHO$$\Longrightarrow$ HO_2+CH_3+CO	3.01E+13	0	39150
299	H+$CH_3CHO$$\Longleftrightarrow$ CH_2CHO+H_2	2.05E+09	1.2	2405
300	H+$CH_3CHO$$\Longrightarrow$ CH_3+H_2+CO	2.05E+09	1.2	2405
301	OH+$CH_3CHO$$\Longrightarrow$ CH_3+H_2O+CO	2.34E+10	0.7	-1113
302	HO_2+$CH_3CHO$$\Longrightarrow$ CH_3+H_2O_2+CO	3.01E+12	0	11923
303	CH_3+$CH_3CHO$$\Longrightarrow$ CH_3+CH_4+CO	2.72E+06	1.8	5920
304	H+CH_2CO(+M^b) $\Longleftrightarrow$ CH_2CHO(+M^b)	4.87E+11	0.4	-1755
	Low pressure limit: 1.01E+42 -7.63 3854			
	Troe parameters: α= 4.65E-01 T^{***}= 201 T^{*}= 1773 T^{**}= 5333			
305	O+$CH_2CHO$$\Longrightarrow$ H+CH_2+CO_2	1.50E+14	0	0
306	O_2+$CH_2CHO$$\Longrightarrow$ OH+CO+CH_2O	1.81E+10	0	0
307	O_2+$CH_2CHO$$\Longrightarrow$ OH+2HCO	2.35E+10	0	0
308	H+$CH_2CHO$$\Longleftrightarrow$ CH_3+HCO	2.20E+13	0	0
309	H+$CH_2CHO$$\Longleftrightarrow$ CH_2CO+H_2	1.10E+13	0	0
310	OH+$CH_2CHO$$\Longleftrightarrow$ H_2O+CH_2CO	1.20E+13	0	0
311	OH+$CH_2CHO$$\Longleftrightarrow$ HCO+CH_2OH	3.01E+13	0	0
312	CH_3+C_2H_5(+M^b) $\Longleftrightarrow$ C_3H_8(+M^b)	9.43E+12	0	0
	Low pressure limit: 2.71E+74 -16.82 13065			
	Troe parameters: α= 1.53E-01 T^{***}= 291 T^{*}= 2742 T^{**}= 7748			
313	O+$C_3H_8$$\Longleftrightarrow$ OH+C_3H_7	1.93E+05	2.7	3716
314	H+$C_3H_8$$\Longleftrightarrow$ C_3H_7+H_2	1.32E+06	2.5	6756
315	OH+$C_3H_8$$\Longleftrightarrow$ C_3H_7+H_2O	3.16E+07	1.8	934
316	C_3H_7+$H_2O_2$$\Longleftrightarrow$ HO_2+C_3H_8	3.78E+02	2.7	1500
317	CH_3+$C_3H_8$$\Longleftrightarrow$ C_3H_7+CH_4	9.03E-01	3.7	7154
318	CH_3+C_2H_4(+M^b) $\Longleftrightarrow$ C_3H_7(+M^b)	2.55E+06	1.6	5700
	Low pressure limit: 3.00E+63 -14.60 18170			
	Troe parameters: α= 1.89E-01 T^{***}= 277 T^{*}= 8748 T^{**}= 7891			
319	O+$C_3H_7$$\Longleftrightarrow$ C_2H_5+CH_2O	9.64E+13	0	0
320	H+C_3H_7(+M^b) $\Longleftrightarrow$ C_3H_8(+M^b)	3.61E+13	0	0
	Low pressure limit: 4.42E+61 -13.55 11357			
	Troe parameters: α= 3.15E-01 T^{***}= 369 T^{*}= 3285 T^{**}= 6667			
321	H+$C_3H_7$$\Longleftrightarrow$ CH_3+C_2H_5	4.06E+06	2.2	890
322	OH+$C_3H_7$$\Longleftrightarrow$ C_2H_5+CH_2OH	2.41E+13	0	0
323	HO_2+$C_3H_7$$\Longleftrightarrow$ O_2+C_3H_8	2.55E+10	0.3	-943
324	HO_2+$C_3H_7$$\Longrightarrow$ OH+C_2H_5+CH_2O	2.41E+13	0	0
325	CH_3+$C_3H_7$$\Longleftrightarrow$ 2C_2H_5	1.93E+13	-0.3	0

(A: frequency factor, β: pre-exponential temperature exponent, E: activation energy)

Fall off reaction in the Troe form: $F_{\text{cent}} = (1-\alpha)\exp(-T/T^{***})+\alpha\exp(-T/T^{*})+\exp(-T^{**}/T)$

M^{a} : H_2/2.40/ H_2O/15.40/ CH_4/2.00/ CO/1.75/ CO_2/3.60/ C_2H_6/3.00/ AR/0.83/

M^{b} : H_2/2.00/ H_2O/6.00/ CH_4/2.00/ CO/1.50/ CO_2/2.00/ C_2H_6/3.00/ AR/0.70/

M^{c} : H_2/2.00/ O_2/6.00/ H_2O/6.00/ CH_4/2.00/ CO/1.50/ CO_2/3.50/ C_2H_6/3.00/ AR/0.50/

M^{d} : O_2/0.00/ H_2O/0.00/ CO/0.75/ CO_2/1.50/ C_2H_6/1.50/ N_2/0.00/ AR/0.00/

M^{e} : H_2/0.00/ H_2O/0.00/ CH_4/2.00/ CO_2/0.00/ C_2H_6/3.00/ AR/0.63/

M^{f} : H_2/0.73/ H_2O/3.65/ CH_4/2.00/ C_2H_6/3.00/ AR/0.38/

M^{g} : H_2/2.00/ H_2O/6.00/ CH_4/3.00/ CO/1.50/ CO_2/2.00/ C_2H_6/3.00/ AR/0.70/

M^{h} : H_2/2.00/ H_2O/6.00/ CH_4/2.00/ CO/1.50/ CO_2/2.00/ C_2H_6/3.00/

M^{i} : H_2/2.00/ H_2O/0.00/ CH_4/2.00/ CO/1.50/ CO_2/2.00/ C_2H_6/3.00/

M^{j} : H_2/2.00/ H_2O/6.00/ CH_4/2.00/ CO/1.50/ CO_2/2.00/ C_2H_6/3.00/ AR/0.625/

M^{k} : H_2/2.00/ H_2O/6.00/ CH_4/2.00/ CO/1.50/ CO_2/2.00/ C_2H_6/3.00/ AR/1.0/

Acknowledgments

Firstly, I would like to express a deep sense of gratitude to my supervisor, Prof. Tanahashi, for his continuous support and exemplary guidance throughout the course of my research. I am also grateful to Assoc. Prof. Shimura, Assist. Prof. Fukushima and Assist. Prof. Naka for their assistance on this thesis. Their valuable feedbacks helped me to improve this thesis in many ways.

The financial support of Monbukagakusho during my studies in Japan is gratefully acknowledged.

I must thank Johchi and Hiraoka, for their friendship and support in the lab.

Thanks to my laboratory mates, Ito, Aoki, Miyata, Osawa, Matsui, Saito, Kishita, Kobayashi and Yoshida.

I am grateful to the past members of Reactive Gas Dynamics Laboratory. In no particular order, Katayama, Kadowaki, Matsukawa, Matsumoto, Nuka, Kuchiki, Tomita, Park, Katada, Ogawa, Murayama. On behalf of Turkish people, I am eternally thankful for their generous assistance to earthquake stricken Van city in 2011.

Special thanks to my friends back home, Ahmet, Emrah, Togay, Muammer, Saglam, Muhdi, Nozim, Murat and Emre, for their prayers and support.

I am grateful to my very good friend, Erkan Gunpinar, for making my life more enjoyable in Japan. Also I would never forget Selim, Talgat, Erman, Azer, Emre, Yeldos, Nazim, Mustafa and Djibi, for making my life much easier in Japan and for many other things. I am thankful to Rie for her patience and understanding.

I am grateful to my parents and my brothers. I feel a deep sense of gratitude to them, deeper than I know how to express, for their support and prayers.